

PRELIMINARY CHARACTERIZATION OF THE RESPONSE OF AN
ORGANIC THIN FILM TRANSISTOR TO IONIZING RADIATION

by

M. Allan Hupman

Submitted in partial fulfillment of the requirements
for the degree of Master of Science

at

Dalhousie University
Halifax, Nova Scotia
August 2017

© Copyright by M. Allan Hupman, 2017

Table of Contents

List of Tables	v
List of Figures	ix
Abstract	x
List of Abbreviations and Symbols Used	xi
Acknowledgements	xiv
Chapter 1 Introduction	1
1.1 Radiation interactions with matter	1
1.2 Dosimeters	5
1.3 MOSFET Structure and Operation in Saturation Mode	8
1.3.1 MOSFET Channel Formation	8
1.3.2 Saturation Mode	11
1.3.3 Derivation of MOSFET Equations	11
1.4 OTFT Operation (P-channel)	14
1.5 Extraction of Important Parameters	16
1.6 MOSFET response to ionizing irradiation	17
1.6.1 Charge Yield	19
1.6.2 Oxide Traps	19
1.6.3 Interface Traps	20
1.6.4 Threshold Voltage Shift	20
1.7 Measured MOSFET Response to Ionizing Irradiation	21
1.8 MOSFET Radiation Response Characteristics	22
1.8.1 Temperature dependence	22
1.8.2 Energy dependence	23
1.8.3 Directional Dependence	24
1.8.4 Dose and Dose Rate Dependence	25
1.8.5 Time Dependence	25
1.9 Organic Semiconductors Response to ionizing irradiation	25
1.10 Energy Dependence of Organics	26

1.11	Potential Applications	27
Chapter 2	Methods	29
2.1	Fabrication Techniques and Procedures	29
2.1.1	Spin Coating Process	29
2.1.2	Physical Vapor Deposition	29
2.1.3	Parylene-C Deposition	30
2.2	OTFT Fabrication	32
2.3	OTFT Irradiation Setup	34
2.4	Directional Dependence	38
2.5	Extracting important Parameters	39
2.6	Monte Carlo Simulations	39
Chapter 3	Results	42
3.1	Designing new OTFTs	42
3.2	Fabrication Challenges	43
3.3	Substrate Preparation	44
3.4	Response to Irradiation	47
3.5	Comparing an irradiated device to a control device for parylene-C	53
3.6	Changing to a PMMA dielectric	54
3.7	Irradiated PMMA OTFT	56
3.8	Improving OTFT Performance with a PMMA dielectric	58
3.9	Effects of Encapsulation and Copper Tape Contacts	60
3.10	Irradiation Response of OTFTs with PMMA Dielectric	62
3.10.1	OTFT Lifetime	65
3.10.2	Directional Dependence	66
3.10.3	Dose Rate Dependence	67
3.11	Monte Carlo Simulations	68
3.11.1	Simplistic Design	68
3.11.2	Directional Dependence	74

Chapter 4	Discussion	76
4.1	Improving OTFT function	76
4.2	Mobility Degradation with Dose	77
4.3	Threshold Voltage Shift with Dose	77
4.4	Lifetime of OTFTs	79
4.5	Comparisons of Different Quality Photon Beams	79
4.6	Monte Carlo Energy Dependence	80
4.7	Objectives of Work	81
Chapter 5	Conclusion	83
Chapter 6	Future Work	84
6.1	More Reproducible OTFTs	84
6.2	Removal of OTFTs from Glass	85
6.3	Energy and Directional Dependence	85
6.4	Other Organic Electronics	86
6.5	Other OTFT Investigations	86
6.6	Monte Carlo Simulations	86
Bibliography		88

List of Tables

Table I	Important OTFT parameters such as threshold voltage (V_{TH}), mobility (μ), on current (I_{ON}), and off current (I_{OFF}) are given for the old batch, a new batch with 100 nm Parylene-C dielectric and a new batch with 300 nm Parylene-C dielectric.	47
Table II	The starting (before irradiation) OTFT parameters: threshold voltage (V_{TH}), on current (I_{ON}), and off current (I_{OFF}) are given for each photon beam energy.	80

List of Figures

Figure 1.1	Plot of the tumor control probability (TCP) and normal tissue complication probability (NTCP) as a function of Dose.	2
Figure 1.2	Schematic diagram of a p-channel MOSFET. The three electrodes are the source (S), drain (D), and gate (G).	9
Figure 1.3	With a negative bias applied to the gate, electrons in the n-type substrate are pushed down into the substrate.	10
Figure 1.4	Provided the gate bias is sufficient to create a channel, applying a negative drain bias allows the holes to flow from the source to the drain.	12
Figure 1.5	Schematic representation of a MOSFET used to derive the relationship between the source-drain current (I_{DS}) and the gate-source voltage (V_{GS}).	15
Figure 1.6	Schematic diagram of a top contact bottom gate organic field effect transistor (OTFT).	16
Figure 1.7	Charge carriers are pulled into the channel from the source due to the gate bias ($-V_{GS}$).	17
Figure 1.8	An example of the square root of the source-drain current plotted against the source-gate voltage used to extract the mobility and threshold voltage of the device.	18
Figure 1.9	On the left is the photon cross section as a function of energy for water, silicon, and silicon dioxide.	24
Figure 1.10	The total photon cross sections as a function of energy are shown for several organics and silicon.	27
Figure 2.1	Schematic representation of spin coating.	30
Figure 2.2	Physical vapor deposition is used to deposit a thin layer (50 nm in this study) of material (pentacene, gold or aluminum in this study) in a pattern on the substrate.	31
Figure 2.3	Schematic representation of parylene-C deposition.	32
Figure 2.4	On the left is a cross sectional view and on the right a top-down view of the first OTFT fabricated on a glass substrate.	33

Figure 2.5	On the left is a cross-sectional view and on the right is a top down view of the OTFTs fabricated on a flexible PET substrate.	35
Figure 2.6	Orthovoltage irradiation setup.	36
Figure 2.7	MV irradiation setup.	37
Figure 2.8	Directional dependence measurements.	38
Figure 2.9	On the left is the simplistic design of the OTFT.	40
Figure 3.1	On the left is a cross-sectional view and the right a top view of the old device.	43
Figure 3.2	Transfer curves of the first functional devices (blue) and after improving the cleaning techniques (red).	46
Figure 3.3	Transfer curves of OTFTs made with 100 nm parylene-C dielectric (blue) and 300 nm parylene-C dielectric (red).	47
Figure 3.4	Transfer curves of the first irradiated OTFT made with a 300 nm parylene-C dielectric layer.	49
Figure 3.5	Change in threshold voltage as a function of dose as extracted from the transfer curves shown in figure 3.4.	50
Figure 3.6	Change in the normalized mobility as a function of accumulated dose for an OTFT made with a 300 nm parylene-C dielectric layer and irradiated with 180 kVp photon beam.	51
Figure 3.7	Part a) shows the transfer curves of an OTFT irradiated up to 160 Gy from figure 3.4.	52
Figure 3.8	Transfer curves of the OTFT shown in figure 3.4 are shown in part a) with black lines indicating points of constant current where the gate bias is extracted for each curve.	53
Figure 3.9	The threshold voltage shift as a function of the number of times the device was measured is shown for an irradiated OTFT and a control that was not irradiated.	54
Figure 3.10	A family of 50 transfer curves of the first OTFT made with a PMMA dielectric layer.	55
Figure 3.11	The threshold voltage for 50 measurements of the PMMA OTFT which shows more stability than the parylene-C OTFT.	56
Figure 3.12	Transfer curves of the first OTFT with a PMMA dielectric irradiated.	57

Figure 3.13	The threshold voltage shift of the first OTFT irradiated with a PMMA dielectric.	58
Figure 3.14	An OTFT made with a PMMA dielectric measured in the irradiation setup, but was not irradiated.	60
Figure 3.15	Transfer curves taken before (no copper tape or encapsulation layer), after copper tape connected to the electrical contacts, and then after the entire device was encapsulated with approximately 1 μm of parylene-C.	61
Figure 3.16	The plot on the left shows an OTFT that had worse performance when encapsulated.	62
Figure 3.17	The change in threshold voltage as a function of accumulated dose for each energy used.	63
Figure 3.18	The sensitivity (change in threshold voltage with dose) is plotted as a function of accumulated dose for each of the four photon beams used in this study.	64
Figure 3.19	The normalized mobility of an OTFT with accumulated dose for each of the photon beams used in this study.	65
Figure 3.20	The change in threshold voltage as a function of time for an OTFT irradiated up to 1000 Gy with a 6 MV photon beam.	66
Figure 3.21	An OTFT was placed at the isocenter of an 18 MV photon beam and irradiated at incidence angles of 0° , 90° , and 180°	67
Figure 3.22	An OTFT irradiated with an 18 MV photon beam in 15 Gy increments.	68
Figure 3.23	On the left is a schematic of a simplistic OTFT with the parylene-C on the inside and on the right parylene-C is on the outside.	69
Figure 3.24	Perturbation factor as a function of energy for the varying thickness of parylene-C as the inside layers (figure 3.24) of the OTFT.	70
Figure 3.25	Perturbation factor as a function of energy for the varying thickness of parylene-C as the outside layers (figure 3.25) of the OTFT.	71
Figure 3.26	Schematic of simulated OTFT where the thickness of the PMMA layers were variable, but both layers had the same thickness.	72
Figure 3.27	Perturbation factor for the OTFT in figure 3.26 normalized to 100 keV.	73

Figure 3.28	Perturbation factor for the OTFT in figure 3.27 normalized to 100 keV.	74
Figure 3.29	The perturbation factors simulated for the realistic OTFT shown in figure 2.4 for beam energies of Co-60, 6 MV, 10 MV, and 18 MV and beam incident angles of 0°, 90°, and 180°.	75

Abstract

Organic thin film transistors (OTFTs) were investigated as novel radiation detectors. OTFTs were fabricated on glass and PET substrates, with a pentacene semiconductor, and PMMA or Parylene-C dielectric. Kilovoltage (100, 180 kVp) and megavoltage (6, 18 MV) photon beams were used to irradiate OTFTs to 400 Gy. One OTFT was irradiated to 1000 Gy to observe its longevity. Irradiated devices showed a positive shift in the threshold voltage and a degradation in mobility. Initial sensitivity of devices was greater for kilovoltage-irradiated devices than megavoltage-irradiated devices, but converged after ~ 200 Gy to a value of ~ 1 mV/Gy and continued to decrease slowly at higher doses. After 1000 Gy, one device remained functional. Directional and dose rate dependence measurements were inconclusive and require further investigation. Monte Carlo simulations found less than 5% intrinsic energy dependence for photon spectra from Co-60 to 15 MV.

List of Abbreviations and Symbols Used

Abbreviations

BCA	Boundary crossing algorithm
DNA	Deoxyribonucleic acid
HOMO	Highest occupied molecular orbital
ITO	Indium tin oxide
LET	Linear energy transfer
LUMO	Lowest unoccupied molecular orbital
MOSFET	Metal oxide semiconductor field effect transistor
NPLC	Number of power line cycles
NTCP	Normal tissue complication probability
OTFT	Organic thin film transistor
P3HT	Poly(3-hexylthiophène)
PDMS	Polydimethylsiloxane
PET	Polyethylene terephthalate
PMMA	Poly(methyl methacrylate)
PTTA	Poly-(triarylamine)
SMU	Source measurement unit
SSD	Source-surface distance
TCP	Tumor control probability

TIPS-pentacene	6,13-bis(triisopropylsilyl)ethynyl-pentacene
TLDs	Thermoluminescent dosimeters
Symbols	
κ/ρ	Pair Production mass attenuation coefficient
μ	Mobility
σ_R/ρ	Rayleigh mass attenuation coefficient
σ/ρ	Compton mass attenuation coefficient
τ/ρ	Photoelectric mass attenuation coefficient
C	Capacitance
CF	Calibration factor
C_{ox}	Oxide capacitance per unit area
D	Dose
E	Energy
E_b	Binding energy
f	Fraction yield of holes
I_{DS}	Drain-source current
T	Kinetic energy
L	Length
mc^2	Rest energy of an electron
t_{ox}	Thickness of Oxide
V_{DS}	Drain-source Voltage

V_{GS}	Gate-source Voltage
V_{TH}	Threshold Voltage
W	Width
Z	Atomic number

Acknowledgements

There are many people who have contributed over the past couple of years both directly and indirectly to this work. First, is my supervisor Dr. Alasdair Syme. He was always available with great advice and guidance whenever needed. Thank you for the great opportunity and keeping me on track throughout the project. Next I would like to thank Dr. Ian Hill for letting me use his lab and helping me troubleshoot along the way. Also JP Sun, Charlotte Clegg, and Carmen Lee for teaching me fabrication techniques and maintenance of the lab equipment.

I would like to thank my committee members Dr. James Robar, Dr. Ian Hill, and Dr. Alasdair Syme for all their suggestions and timely feedback.

I would like to thank Maddy Baldissera for all her support, encouragement and for having patience with me. Lastly, I would like to thank my family for all of their encouragement and confidence in me. Thank you all!

Chapter 1

Introduction

1.1 Radiation interactions with matter

Ionizing irradiation has societal benefits such as medical imaging, nuclear power, food safety, airport security, radiotherapy, and others. However, human exposure to ionizing irradiation can be harmful due to its ability to disrupt critical molecular bonds – particularly in cellular DNA [1]. Consequently, being able to detect and accurately quantify fields of ionizing radiation are critical prerequisites for its safe use.

Approximately half of all patients diagnosed with cancer should receive some form of radiotherapy over the course of their treatment [2]. Radiotherapy represents a balancing act in which the dose of radiation delivered to a target is large enough to produce a high probability of controlling disease progression, while not being so high as to incur a significant risk of severe complications in surrounding healthy tissues. This type of dose response relationship is typically modelled by a sigmoidal curve that rises steeply from low to high probability (see figure 1.1). Therefore, accurate dosimetry is needed to deliver successful radiotherapy.

When photons with sufficient energy are incident on a material, they can interact and produce ionizations and excitations in the material. The four most common interaction types are: Rayleigh scatter, photoelectric effect, Compton scatter and pair production. The pertinent information of these interactions will be discussed, but a more detailed explanation can be found elsewhere [3]. Rayleigh scattering is a process in which a photon deflects through a small angle due to an interaction with a particle in the medium. The oscillating electric field of the photon acts on the charges within the particle, causing them to oscillate with the same frequency. This causes the particle to become a radiating dipole and the resulting radiation we see as scattered light. Rayleigh scattering is an elastic process, meaning that no energy is lost by the photon when it scatters. The mass attenuation coefficient (linear attenuation coefficient divided by the mass density of the material) for Rayleigh scattering, σ_R/ρ , depends on both the energy of the photon and

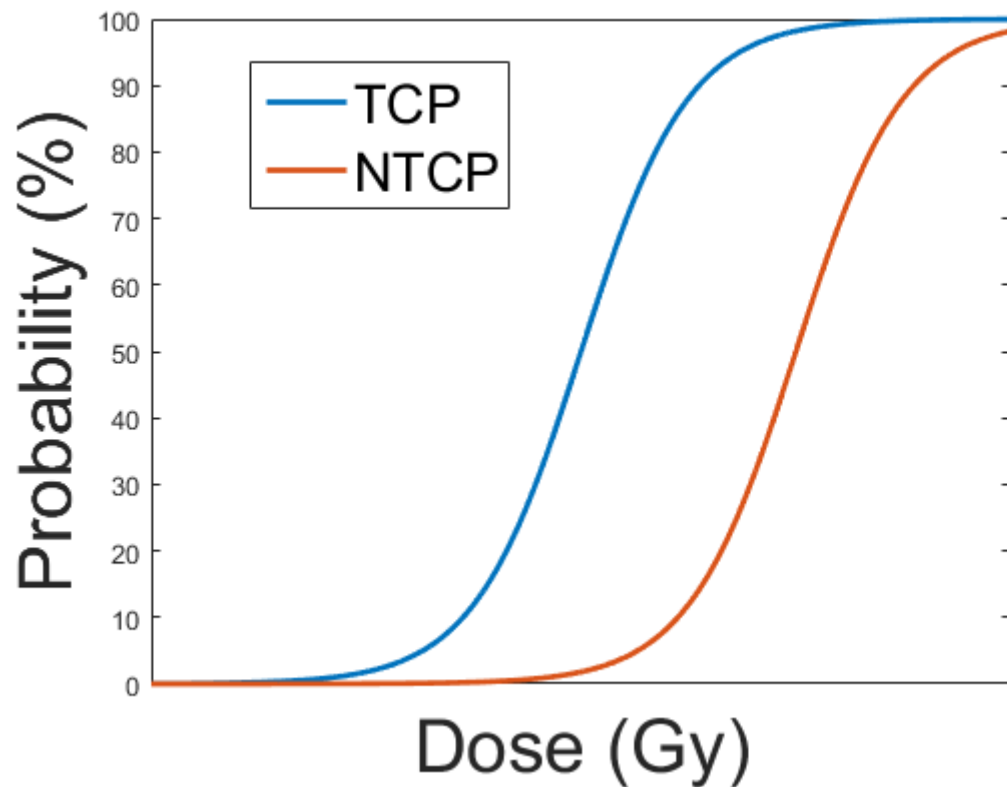


Figure 1.1: Plot of the tumor control probability (TCP) and normal tissue complication probability (NTCP) as a function of Dose. Radiotherapy is a balancing act between giving enough dose to give a high probability of tumor control, while not too high to incur a high probability of complications in the surrounding healthy tissue.

the atomic number of the material through which the photon is traveling:

$$\frac{\sigma_R}{\rho} \propto \frac{Z}{E^2} \quad (1.1)$$

where E is the energy of the incident photon and Z is the atomic number of the medium. Pair production occurs when the photon passes close to the nucleus of the atoms and if the energy of photon is high enough (>1.022 MeV) it is converted to an electron and positron pair and their associated kinetic energies. The mass attenuation coefficient for pair production, κ/ρ , depends on the atomic number of the material through which the photon is traveling:

$$\frac{\kappa}{\rho} \propto Z \quad (1.2)$$

The photon spectra used in this work range from 100 kV to 18 MV and although Rayleigh scattering and pair production can occur in these beams they are responsible for a low percentage of interactions.

In this work the two main interactions of interest are the photoelectric effect and the Compton effect. The photoelectric effect occurs when a photon interacts with an atom containing orbital electrons of binding energy less than the photon. The energy of the photon is absorbed by the atom, then the atom releases an orbital electron (called a photoelectron) with kinetic energy of the incident photon energy minus the energy of the binding energy of the electron. In equation form this is given by:

$$T = E - E_b \quad (1.3)$$

Where T is the kinetic energy of the electron, E is the incident photon energy, and E_b is the binding energy of the electron. The space left by the electron is filled with another orbital electron from a higher energy shell, which is accompanied by the emission of a characteristic X-ray or the emission an outer shell electron known as an Auger electron. The mass attenuation coefficient for the photoelectric effect, τ/ρ , is strongly dependent on both the energy of the photon and the atomic number of the material through which the photon is traveling:

$$\frac{\tau}{\rho} \propto \frac{Z^n}{E^m} \quad (1.4)$$

where Z is the atomic number of the medium and E is the incident photon energy. The value of n ranges from ~ 3 at 0.1 MeV and rises to ~ 3.6 at 3 MeV. The value of m ranges

from ~ 3 at 0.1 MeV and gradually decreases to ~ 1 at 5 MeV [3]. Below about 0.1 MeV where the photoelectric effect is most dominant m and n are ~ 3 .

The Compton effect occurs when the photon has an energy much greater than the binding energy of electron. The photon gives up some of its energy to the electron and scatters. The equations that describe Compton interactions are:

$$E' = \frac{E}{1 + (\frac{E}{m_0 c^2})(1 - \cos\phi)} \quad (1.5)$$

$$T = E - E' \quad (1.6)$$

$$\cot\theta = \left(1 + \frac{E}{m_0 c^2}\right) \tan\left(\frac{\phi}{2}\right) \quad (1.7)$$

where E is the incident photon energy, E' is the scattered photon energy, $m_0 c^2$ is the rest mass of the electron, T is the kinetic energy of the scattered electron, θ is the scattering angle of the electron, and ϕ the scattering angle of the photon. If the energy of the incident photon is known that leaves four unknowns (E' , θ , ϕ , T) and three equations that cannot be solved, but follow a probability distribution based on the energy of the incident photon. The probability of a photon interacting via the Compton effect is dependent on the electron density of the medium:

$$\frac{\sigma}{\rho} \propto \rho_e \quad (1.8)$$

where σ/ρ is the Compton mass attenuation coefficient and ρ_e is the density of electrons in the medium.

Equations 1.4 and 1.8 show the probability of interaction via the photoelectric effect and Compton effect. Compton effect does not depend on the atomic number, whereas for the photoelectric effect there is a strong dependence. When making dosimetric measurements in radiation fields that produce a significant number of photoelectric interactions in the detector (e.g. diagnostic x-ray beams), the composition of the detector should be similar to tissue so that the interactions in the active volume of the detector mimic that of tissue.

Incident electrons or secondary electrons can interact with the medium via elastic collisions in which no energy is lost; or inelastic collisions in which the electron loses some kinetic energy. Elastic collisions result in a deflection of the electron, but since no energy is deposited in the tissue, it is less important in dosimetry. If an electron

undergoes an inelastic collision with an orbital electron it gives up some of its energy. This results either in an excitation (orbital electron moves to higher energy shell) or ionization (orbital electron escapes the atom). In the event of ionization, if the electron is scattered with sufficient energy, it can go on to produce its own track of ionizations and excitations. The term delta ray is used to describe these secondary electrons. The last type of interaction is an inelastic collision with the nucleus of an atom. The interaction known as Bremsstrahlung, is when an electron decelerates when deflected by another charged particle and the loss of kinetic energy is converted into a photon. Other types of radiations (e.g. protons, carbon ions, etc.) can interact with matter, but those are beyond the scope of this work.

1.2 Dosimeters

When measuring parameters of a radiation field (e.g. dose, dose rate, ionization density, etc.), it is the ionization process itself that often forms the basis of the measured signal in a radiation detector. When calibrated appropriately, the measured signal can be translated to the amount of energy that would be absorbed per unit mass (i.e. absorbed dose) if a small mass of tissue were positioned at the same location as the detector. An ideal dosimeter would possess the following characteristics:

- **Linearity:** Response of the dosimeter should be proportional to the dose absorbed to the detector.
- **Real time readout:** Response of the dosimeter and thus the absorbed dose should be measurable during irradiation.
- **Stability:** Response of the dosimeter to absorbed dose should be consistent over time.
- **Reproducibility:** Response of the dosimeter should be consistent when irradiated with the same conditions.
- **Energy independence:** Response of the dosimeter should be directly proportional to the dose, independent of the type of radiation or its energy. Furthermore, the dose to the dosimeter should be proportional to the dose to the medium at the

point of measurement in the absence of the detector independent of the incident energy.

- Directional independence: Response of the dosimeter should be proportional to the absorbed dose independent of the angle of the incident radiation.
- Temperature and humidity: Response of the dosimeter should be independent of the temperature and humidity.
- Dose rate: Response of the dosimeter should be proportional to the absorbed dose, independent of the dose rate. This includes both instantaneous dose rate (pulsed or continuous) and average dose rate.

None of the currently used dosimeters can be considered ideal. Some examples of currently used dosimeters are ion chambers, thermoluminescent dosimeters (TLDs), radiochromic film, diamond detectors, diodes, and metal oxide semiconductor field effect transistor (MOSFETs).

An ionization chamber consists of a gas filled chamber with two electrodes [4]. A voltage potential between the two electrodes creates an electric field in the chamber. Incident ionizing irradiation can create ion-pairs in the gas chamber. The electric field causes the positive ions to move towards the negative electrode and the negative ions toward the positive electrode. This creates an ionization current which can be measured by an electrometer. The current measured is proportional to the number of ion pairs created, which in turn is proportional to the radiation dose. Since the active volume is a gas it requires larger volumes than a solid state dosimeter to produce a measurable signal. Furthermore, an ionization chamber gives one reading which is the average dose to the active volume. This is problematic for small field dosimetry where the dose changes with a change in position smaller than the size of the detector creating a partial volume effect. Another limitation of ion chambers is their energy dependence which can be problematic at diagnostic energies [5].

TLDs consist of crystalline dielectric material, which contains trace impurities. The trace impurities create trapping centers whose energy levels lie inside the forbidden gap of the pure crystal. When exposed to ionizing irradiation, a TLD stores a fraction of the absorbed energy [6]. Then when a TLD is heated, it releases visible light proportional to the amount of absorbed dose. The emitted photons are not absorbed by the crystal since

their energy is insufficient to promote electrons from the valence band to the conduction band of the crystal. TLDs are considered tissue equivalent in the energy range 20 keV to Co-60 (mean energy 1.25 MeV) [7]. Limitations of TLDs are their lack of real time readout, they require specialized hardware for the readout (reader, annealing oven, nitrogen gas supply), and need precise procedures for calibrating, reading, and annealing.

Radiochromic film consists of a layer of organic monomers that are sensitive to radiation on a polyester base with a transparent coating [8]. When exposed to ionizing radiation, a polymerization reaction causes the film to change colour and the darkness of the film increases with absorbed dose. The film is then scanned with visible light and the transmission used to determine the dose at each point on the film. Due to the sensitivity of the film, great care needs to be taken during manufacturing, transport, storage, and processing to ensure an accurate reading. Another limitation is the readout time. Film needs to be left for ~ 12 -24 hours before it can be read. Furthermore, the uncertainty of film can be made $\sim 1\%$, but it is not practical to reach that level of uncertainty in the clinic due to the difficulty of implementation [9].

When a bias is applied to a diamond detector a depleted neutral region is created [10]. Ionizing radiation creates electron-hole pairs that are attracted to the opposite polarity, which creates current proportional to the dose rate. However, some electrons can become trapped in the diamond creating an electric field opposing the applied field and reducing the current at a given dose rate. By pre-irradiating the detectors the traps will fill to allow the dose rate to be proportional to the current [10]. Potential sources of error of a diamond detector are dark current, temperature dependence, dose rate dependence, and angular dependence. A limitation of the detector is that in comparison to other solid state detectors it is more expensive [10].

A diode dosimeter consists of a lightly doped silicon substrate (either n-type or p-type) and a heavily doped surface region of the opposite type (p-type or n-type) creating p-n junction. The p-n junction creates an electric field making it possible to collect charge without an external bias on the diode. When exposed to ionizing irradiation, an electric current is generated which is measured by an electrometer [11]. The induced current in the diode is proportional to the dose rate. The increased density relative to an ionization chamber allows the active volume to be made much smaller. Limitations of diode dosimeters are the energy dependence, dose per pulse dependence, temperature

dependence, and accumulated dose dependence [12, 13, 14, 15]. As the dose per pulse increases so does the rate of recombination, which lowers the response of the diode to a given dose. The accumulated dose dependence results from damage to the diode which reduces the sensitivity with accumulated dose. Energy dependence results from the materials and composition of the diode and surrounding material (protective housing, buildup material and electrode attachment). The difference in response of a photon diode in comparison to water comes from a higher sensitivity to low energy photons which can result from scatter in the phantom. To compensate for the energy dependence a photon diode is shielded with a high Z material such as tungsten to attenuate the low energy photons [11]. Electron diode detectors are approximately energy independent because the electron stopping power of silicon to water is approximately constant over a wide energy range. Electron diode detectors use much less buildup material and it is a low Z material such as PMMA.

A MOSFET is a voltage controlled current source. When the MOSFET is exposed to ionizing radiation, electron-hole pairs are created throughout the device [16]. Holes become trapped in the Silicon-dioxide of the MOSFET, changing the current that can flow through the MOSFET at a given voltage. By calibrating the rate of change of a particular metric (e.g. threshold voltage) to the absorbed dose, the MOSFET can be used as a dosimeter. The main limitation of a MOSFET is the energy dependence, particularly at low energies. The sensitivity of a MOSFET depends on the device design, but MOSFETs are not used below ~ 1 cGy because the signal fades with time, leading to a large error in measurement at small doses [16]. The remainder of the discussion will be about MOSFETs due to the similarity of the novel radiation detectors used in this study (Organic thin film transistors (OTFT)).

1.3 MOSFET Structure and Operation in Saturation Mode

1.3.1 MOSFET Channel Formation

The structure of a p-channel MOSFET is shown in figure 1.2 (adapted from Sedra and Smith [17]). The transistor is fabricated on an n-type substrate (silicon) with two heavily doped p-type regions at the source and drain. Metal is deposited on the source and drain regions forming electrodes. An insulating layer of silicon dioxide is grown on

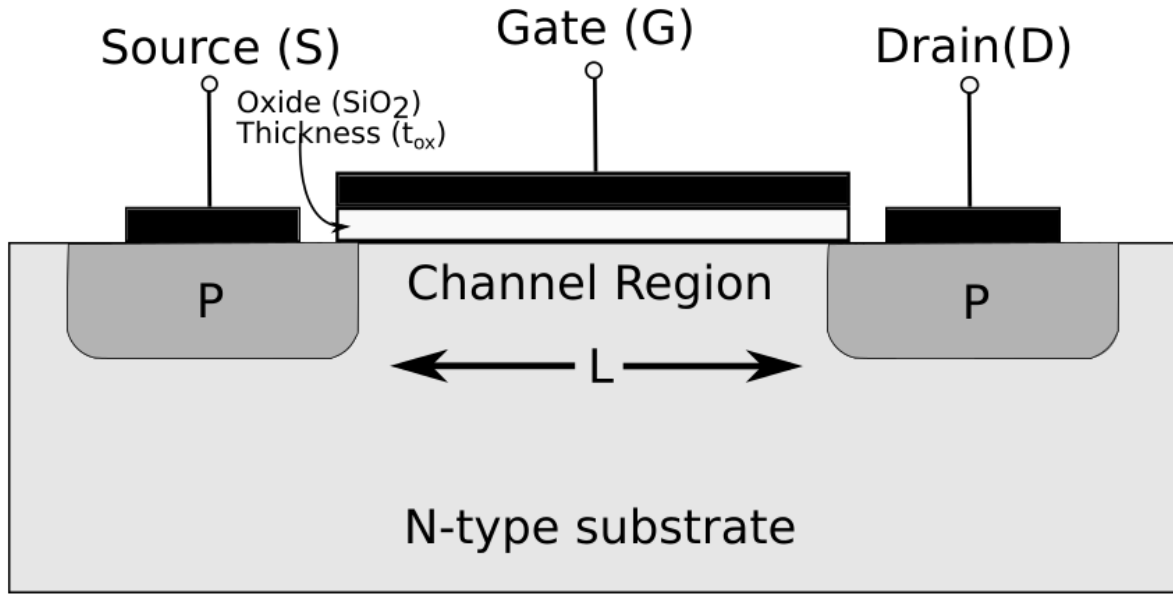


Figure 1.2: Schematic diagram of a p-channel MOSFET. The three electrodes are the source (S), drain (D), and gate (G). The gate electrode controls the conductivity of the channel and the current that can flow between the source and drain. The gate is separated from the channel by an insulating layer of silicon dioxide (SiO_2).

the surface of the substrate covering the area between the source and drain electrodes. Metal is deposited on top of the dioxide forming the gate electrode. The bias on the gate electrode controls whether current can flow between the source and drain regions known as the channel. The channel region has a length L between the electrodes and width W along the electrodes.

With all the contacts grounded, p-n junctions exist at the interface between the n-type substrate and the heavily doped regions at the source and drain. These p-n junctions act as back-to-back diodes in series meaning that no current can flow between the source and drain even if a bias is applied between them (V_{DS}). However, by applying a negative gate bias (V_{GS}) electrons in the channel are pushed down into the substrate leaving a carrier-depletion region. At the same time holes from the source and drain regions are pulled into the channel. If the gate bias is strong enough it can pull in enough holes to connect the source and drain regions, forming a conductive channel (figure 1.3). The channel is created by inverting an n-type substrate into a p-type region known as an inversion layer.

The value of the gate bias (V_{GS}) needed to pull in enough holes to create a conducting

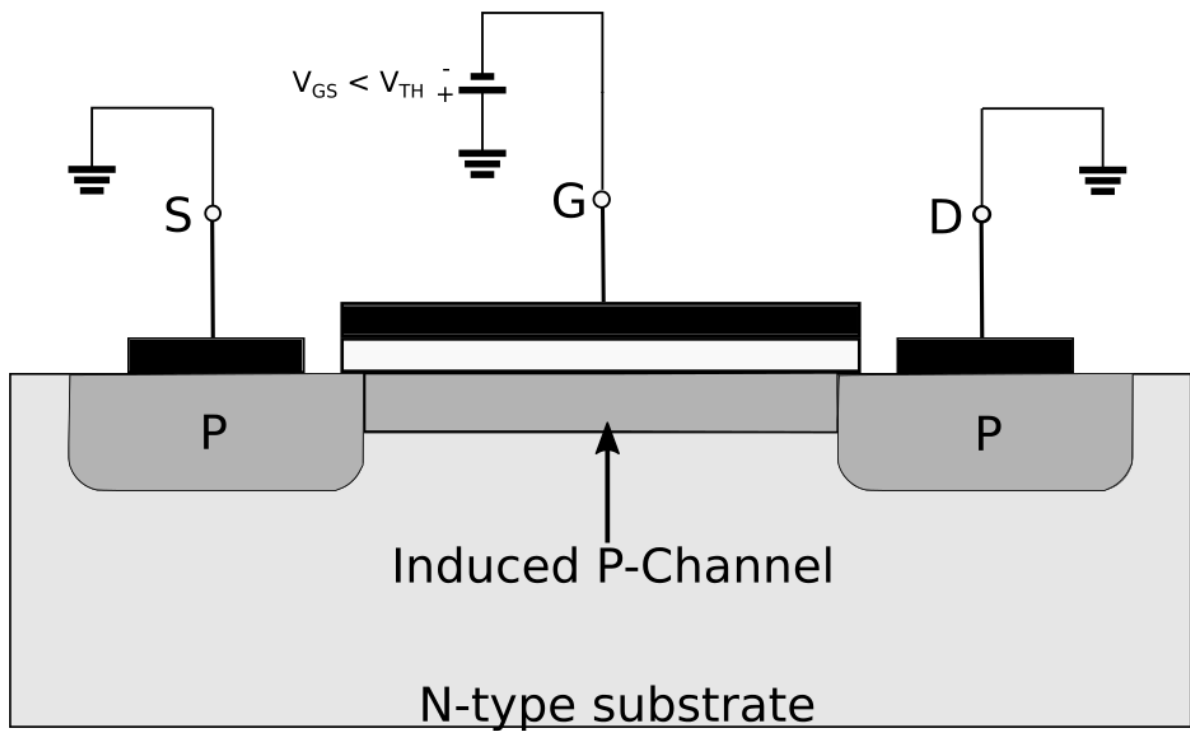


Figure 1.3: With a negative bias applied to the gate, electrons in the n-type substrate are pushed down into the substrate. Holes from the source and drain regions are pulled into the channel at the interface with the silicon dioxide. The channel is created from the n-type substrate inverting to p-type with holes being the majority charge carriers. This diagram was adapted from Sedra and Smith figure 4.2 [16].

channel is called the threshold voltage (V_{TH}). Increasing V_{GS} above the threshold voltage will pull more holes into the channel, which enhances the channel and give rise to the name enhancement-mode operation. The gate and channel region act as two plates of charge forming a parallel plate capacitor with the silicon dioxide being the dielectric. The resulting electric field controls the amount of charge in the channel and the amount of current that can flow through the device.

1.3.2 Saturation Mode

Assuming the gate bias is sufficient for a conductive channel, applying a bias between the source and drain (negative V_{DS}) will allow holes to flow from source to drain. As V_{DS} increases, the electric field along the channel increases which allows the charge carriers to move faster and creates a higher current. However, increasing the bias also causes the channel to taper because the potential at the source end of the channel is V_{GS} , but is only $V_{GS} - V_{DS}$ at the drain end. A greater negative potential at the source end creates a deeper buildup of holes near the source and shallower one near the drain (figure 1.4). Therefore, increasing the V_{DS} increases the resistance of the channel and does not increase the current linearly. When V_{DS} is high enough to reduce the voltage between the gate and the channel at the drain end to V_{TH} , the channel depth decreases to almost zero and the channel is said to be pinched off. Increasing V_{DS} beyond this point will not increase the current and the drain current is said to saturate at this value. The voltage V_{DS} where this occurs is denoted $V_{DS,sat}$ and is equal to $V_{GS} - V_{TH}$.

1.3.3 Derivation of MOSFET Equations

To analyze and better understand our results, it is important to develop equations that describe the relationship between the source to drain current (I_{DS}) and V_{GS} . Consider an infinitesimal strip of the gate at a distance x from the source (figure 1.5). The capacitance of the strip is:

$$C = C_{ox}Wdx \quad (1.9)$$

where C_{ox} is the capacitance per unit area. The charge stored on this infinitesimal strip is found by multiplying the capacitance by the effective voltage between the gate and the channel at the point x . The voltage responsible for inducing the channel at point x

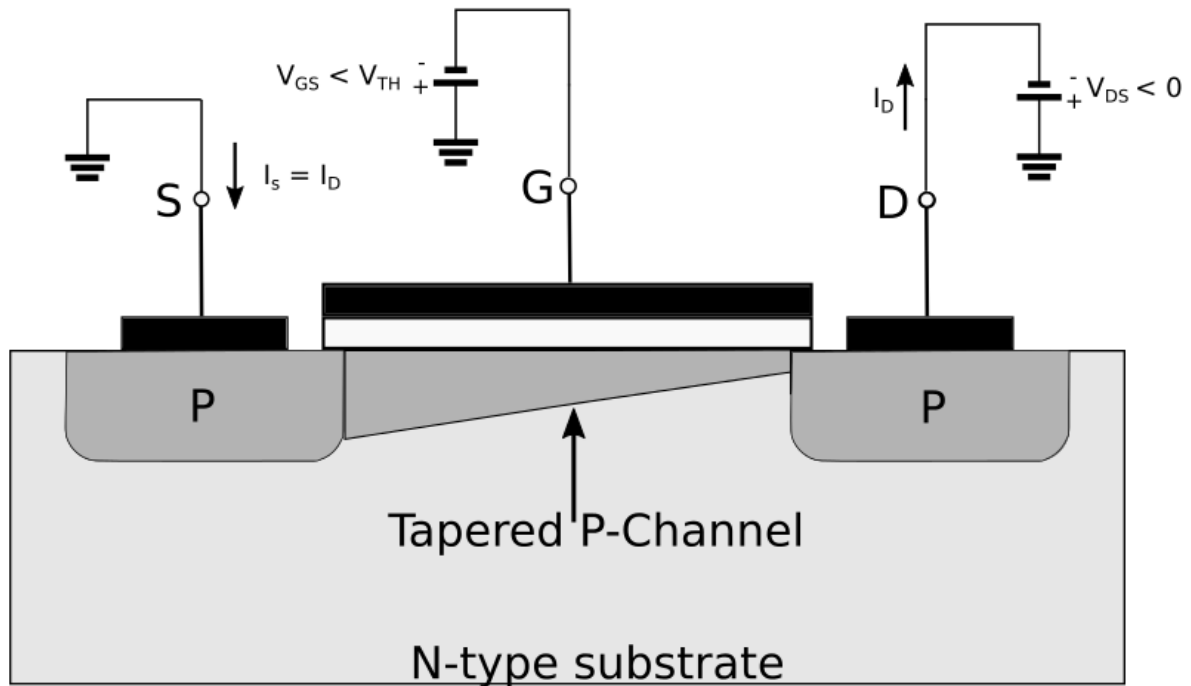


Figure 1.4: Provided the gate bias is sufficient to create a channel, applying a negative drain bias allows the holes to flow from the source to the drain. The drain bias creates a variable electric field along the channel and therefore the channel depth varies and is tapered. When the drain bias is larger than the difference between the gate source voltage and the threshold voltage the channel is said to be pinched off and the MOSFET is operating in saturation mode. Increasing the drain bias above this point will not increase the current.

is $V(x)$, given by:

$$V(x) = [V_{GS} - v(x) - V_{TH}] \quad (1.10)$$

where $v(x)$ is the voltage due to V_{DS} at point x . The hole charge in the infinitesimal portion of the channel is:

$$dq = C_{ox}(Wdx)(V_{GS} - v(x) - V_{TH}) \quad (1.11)$$

The electric field along the channel in the x-direction caused by V_{DS} is:

$$E(x) = \frac{dv(x)}{dx} \quad (1.12)$$

(positive electric field meaning the holes move in the x-direction with E-field). The electric field causes the holes to migrate toward the drain with a velocity of:

$$V = \frac{dx}{dt} = -\mu E(x) = -\mu \frac{dv(x)}{dx} \quad (1.13)$$

Where μ is the mobility of the holes in the channel and depends on the materials and fabrication process. The resulting current can be expressed as:

$$I = \frac{dq}{dt} = \left(\frac{dq}{dx} \right) \left(\frac{dx}{dt} \right) \quad (1.14)$$

Substituting equation 1.11 and 1.13 gives:

$$I = \mu C_{ox} W (V_{GS} - v(x) - V_{TH}) \frac{dv(x)}{dx} \quad (1.15)$$

The source-drain current must be the same at all points along the channel. Since we are interested in the current flowing through the device we will relabel I to I_{DS} . Furthermore, if we rearrange the equation slightly and integrate along the channel from $x = 0$ to $x = L$ or $v(0) = 0$ to $v(L) = V_{DS}$ we get:

$$\int_0^L I_{DS} dx = \int_0^{V_{DS}} \mu C_{ox} W (V_{GS} - v(x) - V_{TH}) dv(x) \quad (1.16)$$

$$I_{DS} = (\mu C_{ox}) \left(\frac{W}{L} \right) ((V_{GS} - V_{TH}) V_{DS} - \frac{1}{2} (V_{DS}^2)) \quad (1.17)$$

As stated before the saturation region begins when $V_{DS} = V_{GS} - V_{TH}$ and substituting this in gives:

$$I_{DS} = \frac{1}{2} (\mu C_{ox}) \left(\frac{W}{L} \right) (V_{GS} - V_{TH})^2 \quad (1.18)$$

In saturation mode, I_{DS} is constant with V_{DS} so this equation will hold as long as saturation is achieved ($V_{DS} > V_{GS} - V_{TH}$). To increase the drain current the electrodes should be long and the spacing between them should be narrow (increase W/L). Furthermore, multiple source and drain contacts in an interdigitated design can be used to further increase the signal.

1.4 OTFT Operation (P-channel)

An organic thin film transistor (OTFT) has a layered design consisting of a thin film of organic semiconductor, an insulator, a substrate, and three electrodes called the source, drain, and gate like a MOSFET. A bottom gate top contact OTFT is depicted in figure 1.6. Similarly to the MOSFET an OTFT operates as a voltage-controlled current source. Applying a bias between the gate and source results in the accumulation of charge carriers near the semiconductor/insulator interface allowing current to flow through the active layer from source to drain if a suitable bias is applied (V_{DS}). An important difference between MOSFETs and OTFTs is the formation of the channel. For MOSFETs the channel results from an inversion process forming a layer of charge carriers, whereas a channel in an OTFT is formed due to the accumulation of charge in the semiconductor.

In a p-type semiconductor a negative V_{GS} produces an electric field across the dielectric and results in the accumulation of holes in the semiconductor (figure 1.7). For charge to flow between the semiconductor and source/drain electrodes the fermi level of the electrodes needs to be closely aligned with either the highest occupied molecular orbital (HOMO) for holes to flow or the lowest unoccupied molecular orbital (LUMO) for electrons. For example pentacene has a HOMO of about 4.5 eV and a LUMO of about 2.5 eV (relative to the vacuum potential)[18]. If the source and drain contacts are made of gold which has a fermi energy of about 5 eV the exchange of holes is much more efficient. Therefore, a p-channel OTFT blocks electron flow due to the large energy difference between the fermi level and the LUMO, even in the presence of an applied positive electric field ($+V_{GS}$). However, applying a sufficiently negative V_{GS} will pull holes into the semiconductor from the source forming a channel. Applying a V_{DS} will result in the holes flowing from the source to drain. Like a MOSFET the V_{DS} results in a potential increase from source to drain meaning the channel behaves like a variable resistor. Like a MOSFET when the magnitude of V_{DS} is great enough the channel is pinched off and the

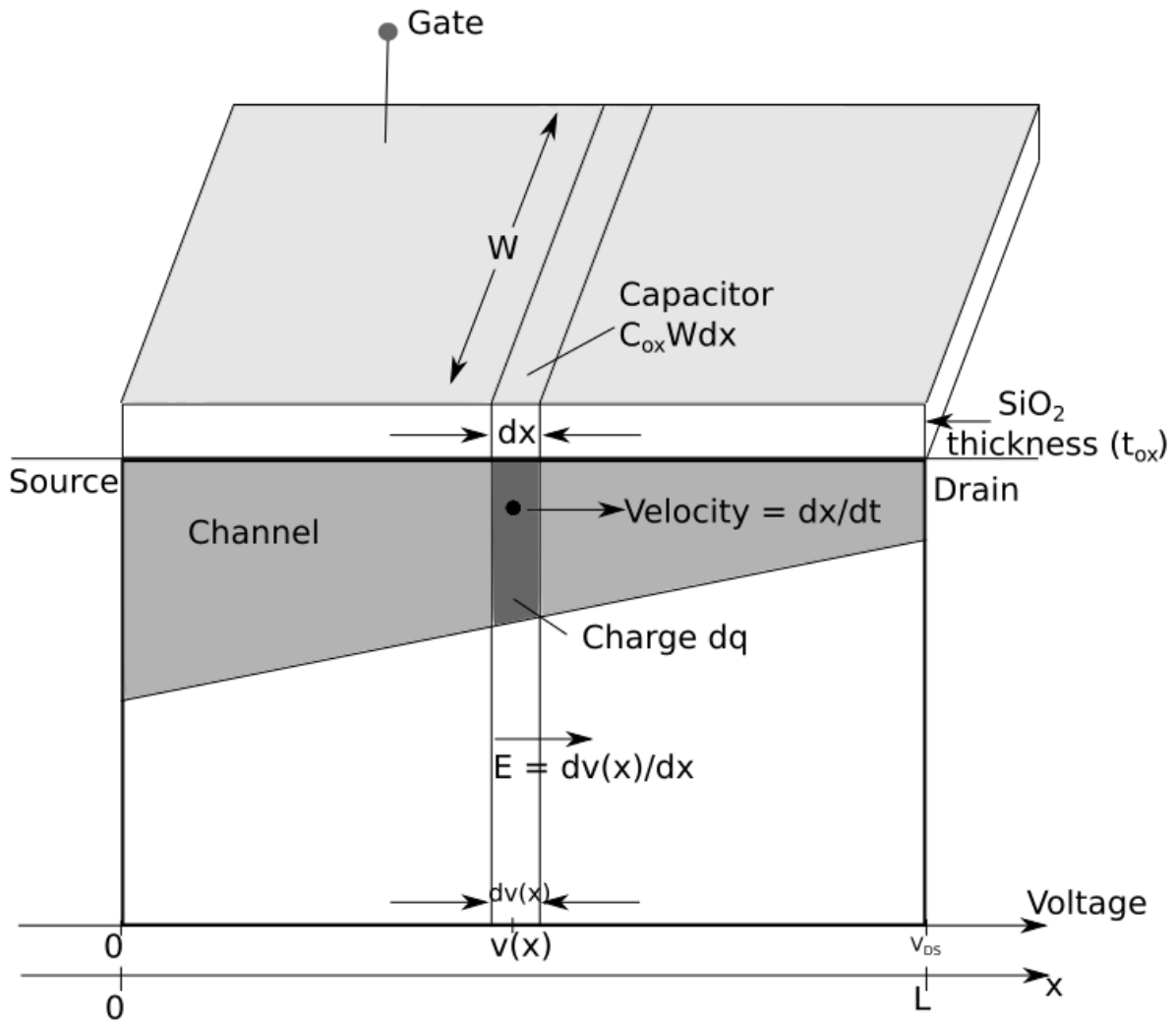


Figure 1.5: Schematic representation of a MOSFET used to derive the relationship between the source-drain current (I_{DS}) and the gate-source voltage (V_{GS}). This is a diagram of a p-channel MOSFET where the bias on the gate is negative which creates a buildup of holes forming the channel. A bias is applied between the drain and source to allow the holes in the channel to move and current to flow between the source and drain.

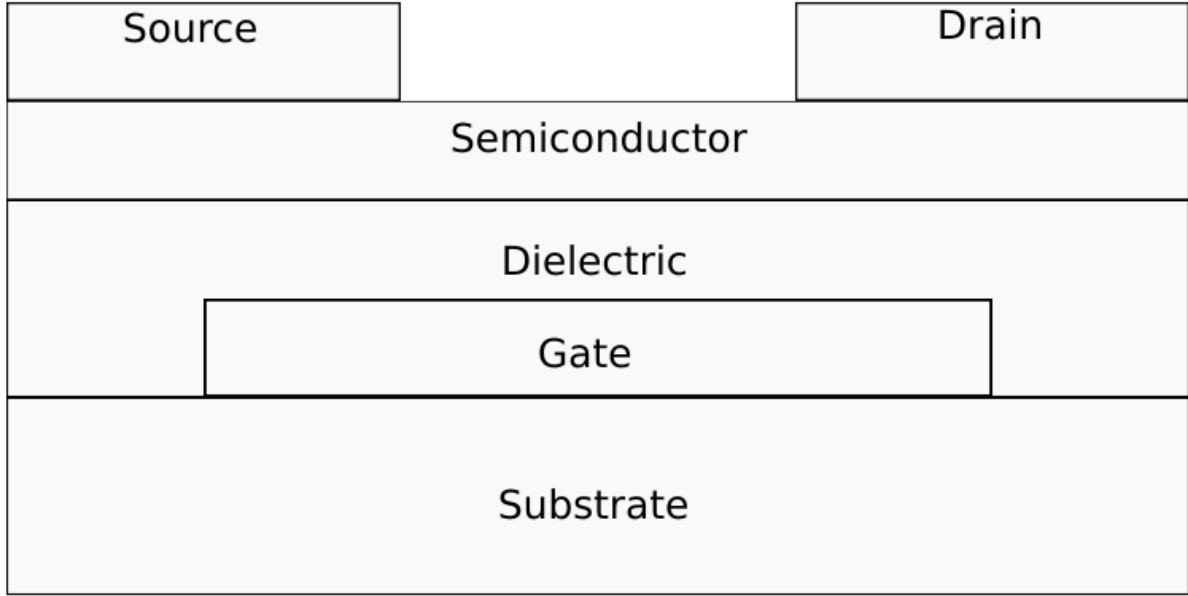


Figure 1.6: Schematic diagram of a top contact bottom gate organic field effect transistor (OTFT).

current saturates (increasing V_{DS} will not increase I_{DS} anymore). Although the transport physics in OTFTs are different than MOSFETs, the current-voltage characteristics still apply and the equations derived still hold.

1.5 Extraction of Important Parameters

When measuring the device in saturation mode the mobility and threshold voltage of the device can be extracted. Plotting the square root of the drain current as a function of the gate bias gives a linear relationship between the two (figure 1.8). Extrapolating the linear region through the x-axis and calculating the x-intercept gives the threshold voltage. Rearranging equation 1.18 the mobility can be determined, the equation is:

$$\mu = 2 \left(\frac{dI_{DS}}{dV_{GS}} \right)^{1/2} \left(\frac{L}{W} \right) \left(\frac{1}{C_{ox}} \right) \quad (1.19)$$

where $(dI_{DS})/dV_{GS}$ is the slope of the curve and the other parameters are known constants determined by the fabrication of the device.

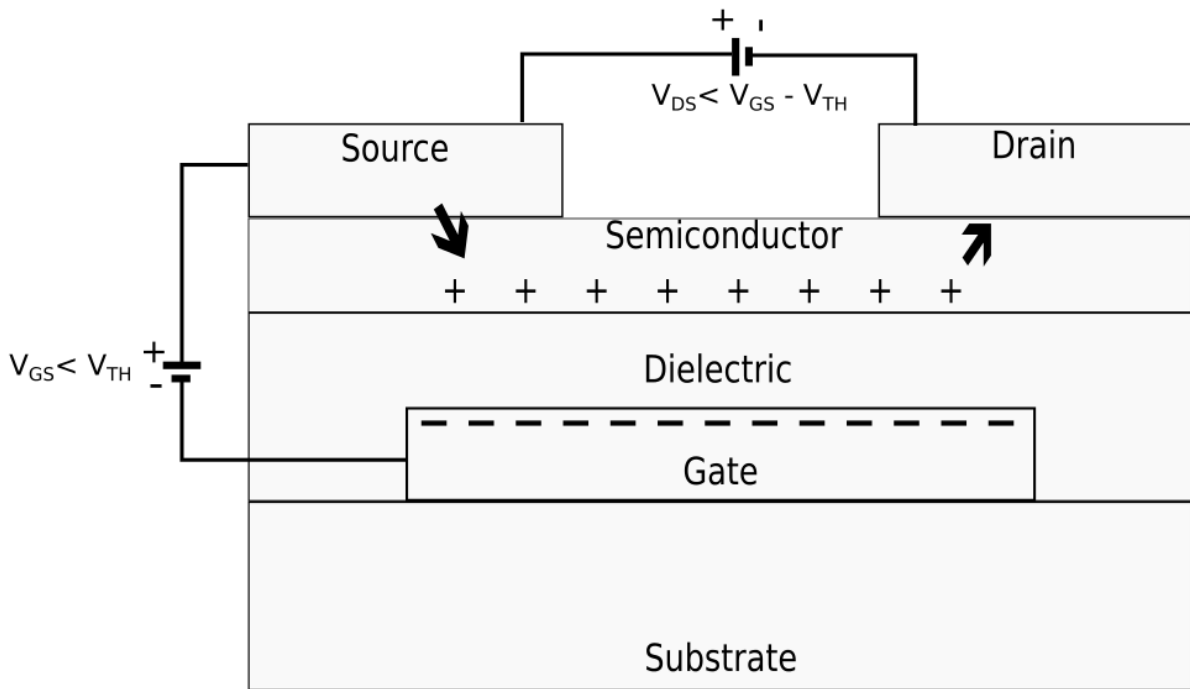


Figure 1.7: Charge carriers are pulled into the channel from the source due to the gate bias ($-V_{GS}$). By applying a negative drain bias (V_{DS}) current will flow from the source to drain.

1.6 MOSFET response to ionizing irradiation

Radiation such as photons, electrons, or protons with sufficient energy (17 ± 1 eV in SiO_2) can ionize atoms creating electron-hole pairs [19]. The resulting electron can create additional electron-hole pairs. Most total dose effects in MOSFETs are due to electron-hole pairs created in the oxide. If a positive bias is applied to the gate electrode during irradiation the resulting electrons created in the oxide will rapidly drift towards the gate and exit the device [19, 20]. However, before electrons can leave the device they can recombine with a hole. The fraction of electron-hole pairs that escape recombination is the charge yield. The remaining holes in the oxide drift toward the Si/SiO_2 interface. As the holes drift they can become trapped in the oxide forming a positive oxide trap charge or they can become trapped near the interface, forming interface traps. These two types of traps are responsible for the shift in threshold voltage of the MOSFET which is used to determine the dose deposited.

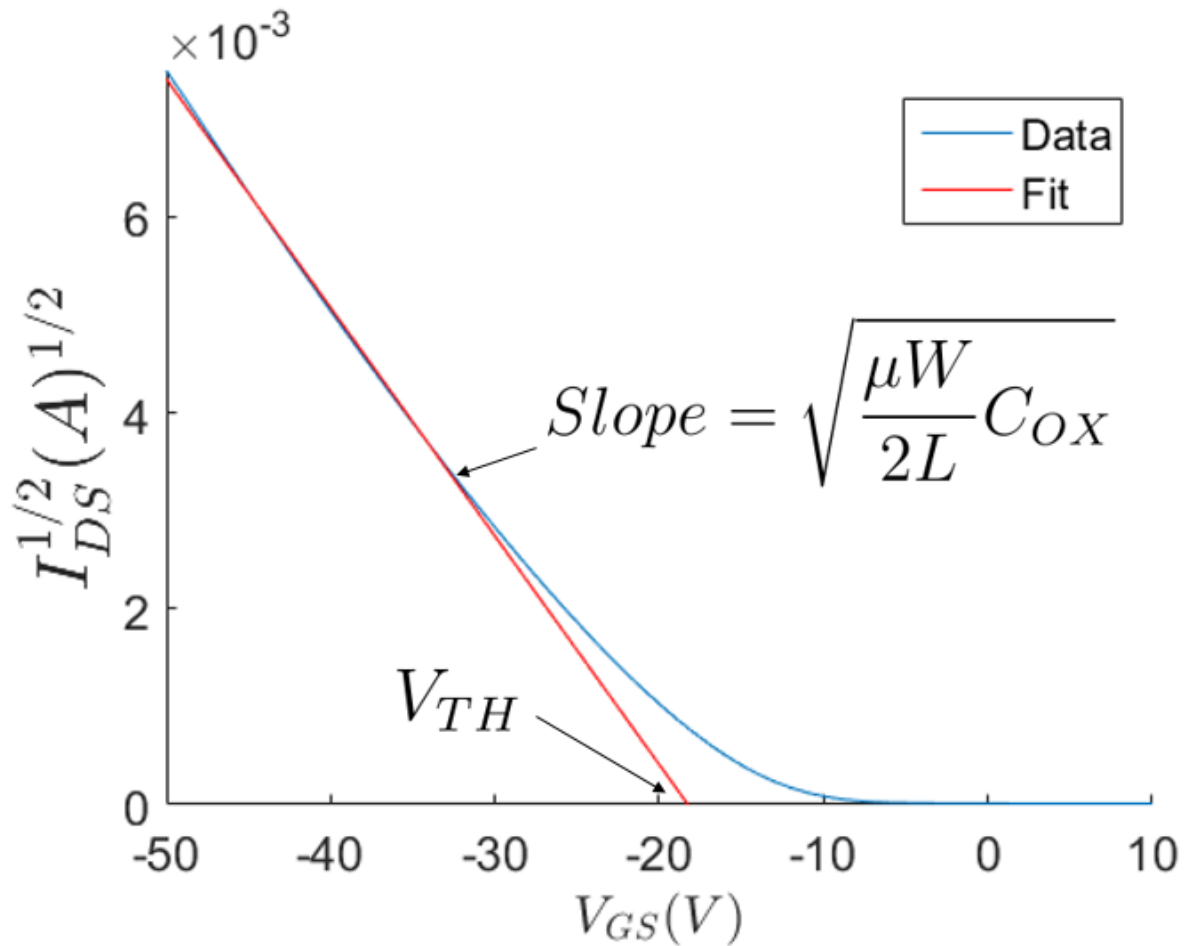


Figure 1.8: An example of the square root of the source-drain current plotted against the source-gate voltage used to extract the mobility and threshold voltage of the device. The linear region of the data is fit and the mobility is calculated using the slope and known constants from the MOSFET design. The threshold voltage is the x-intercept determined from the fit by extrapolating the line through the x-axis.

1.6.1 Charge Yield

The amount of recombination highly depends on the magnitude of the electric field and the line density of charged pairs created by the incident radiation [21]. A stronger electric field will pull the electron and hole apart with more force and decrease the probability of recombination. The line pair density depends on the linear energy transfer (LET), and therefore depends on the energy and type of incident particle. High LET irradiation leaves a dense track of electron hole pairs meaning the created electrons or holes can recombine with a neighbouring pair, increasing the rate of recombination [21, 22, 23].

1.6.2 Oxide Traps

The transportation of holes through the oxide is much slower than electrons [19, 20]. In the presence of a positive gate bias, holes transport toward the Si/SiO_2 interface. As a hole moves through the SiO_2 it causes a distortion of the local potential field which increases the trap depth at the localized site. These holes are transported by what is known as polaron hopping. A polaron is the combination of the hole and the strain field it is creating. A strain field is the movement of the atoms neighboring the hole due to its charge. A polaron increases the effective mass of the holes, which decreases their mobility. This means that as the holes move through the lattice they are trapping themselves (known as a self-trapped polaron).

Close to the Si/SiO_2 interface there is a large number of oxygen vacancies that can act as trapping centers [24]. The number of holes that will become trapped near the interface depends on the applied electric field and the fabrication of the device [25]. Only holes will become trapped in oxide traps meaning that the threshold voltage will shift negatively. Immediately after the holes become trapped they can become neutralized, which means that the MOSFET will operate as it did before the hole became trapped [26]. Oxide-trapped holes can become neutralized either by tunneling of electrons from the silicon or by thermal emission of electrons from the oxide valence band into oxide traps [22, 27]. It should be noted that not all electrons neutralize the hole directly, but some move into an electron trap associated with the trapped hole which effectively neutralizes it. In this case if the applied bias is reversed the electrons can tunnel back into the silicon substrate and a fraction of the original amount of oxide-trapped charge is restored. The degree to which this occurs depends on the annealing conditions, which

include the temperature and the applied bias from the time of irradiation to the time of measurement [27]. The amount of oxide trapped charge does not explicitly depend on the dose rate. If the total time of irradiation and anneal is the same, then the amount of oxide trapped will be equivalent [26]. However, if one measures the device directly after irradiation then a MOSFET irradiated with a higher dose rate will not have had as much time to anneal as a device irradiated to the same dose with a slower dose rate. Therefore the high dose rate device will have less oxide trapped charge neutralized and a greater shift in threshold voltage.

1.6.3 Interface Traps

Radiation leads to the formation of interface traps at the Si/SiO_2 interface as well. These interface traps exist within the silicon band gap at the interface. For p-channel MOSFETs the interface traps are mainly in the lower region of the band gap. The traps are mostly donors meaning that the fermi level at the interface is below the trap energy level and so the trap donates an electron to the silicon. This leaves the trap positively charged and shifts the threshold voltage negatively.

Interface traps build up much slower than oxide-trap charge. The interface traps occur immediately after irradiation, but in one study did not saturate until $\sim 10^5$ s [28]. Like oxide traps, interface traps are electric field-dependent and if a negative bias is applied during irradiation and anneal then an insignificant number of trap states will occur. Furthermore, like oxide traps, there is no dose rate dependence as long as the total irradiation plus anneal time is kept consistent [26]. Unlike oxide traps, an insignificant number of trapped holes will anneal at room temperature. Some annealing of interface traps occurs if the device is above $100^\circ C$ [29, 30]. Interface traps cause the threshold voltage to shift negatively and decrease the mobility of the MOSFET.

1.6.4 Threshold Voltage Shift

The threshold voltage shift of a MOSFET after being irradiated is due to the oxide traps (OT) and the interface traps (IT) given by:

$$\Delta V_{TH} = \Delta V_{OT} + \Delta V_{IT} \quad (1.20)$$

Each can be determined from:

$$\Delta V_{OT,IT} = \left(\frac{-1}{C_{ox}t_{ox}} \right) \int_0^{t_{ox}} \rho_{OT,IT} x dx \quad (1.21)$$

Where ρ is the charge distribution, t_{ox} is the oxide thickness and C_{ox} is the oxide capacitance. For p-channel MOSFETs both oxide traps and interface traps are positive meaning the threshold voltage shift is negative. The threshold voltage shift depends on the time after irradiation. Directly after a high dose rate irradiation, oxide trap charges will dominate. As time passes the oxide trapped charge will begin to neutralize and interface charges will emerge. The threshold voltage shift measured will depend on the temperature and the bias the MOSFET is held at during this time. For low dose rate irradiations the threshold voltage shift will almost entirely be due to interface trapped charge.

1.7 Measured MOSFET Response to Ionizing Irradiation

For MOSFETs operating in passive mode (No gate bias during irradiation) the threshold voltage shift has been found experimentally to be [31]:

$$\Delta V_{TH} \sim 2.2D^{0.9}t_{ox}^2 \quad (1.22)$$

Where D is the dose in cGy, ΔV_{TH} the threshold voltage shift in mV, and the thickness of the oxide in μm . In active mode (Positive gate bias during irradiation) the threshold voltage shift has been found to be:

$$\Delta V_{TH} \sim 40Dt_{ox}^2 f \quad (1.23)$$

Where f is the fraction of holes yield and depends on the applied electric field. The intrinsic sensitivity of a MOSFET is given by dividing the change in threshold voltage by the absorbed dose. The sensitivity can be increased by either increasing the thickness of the oxide or by increasing the hole yield. However, there are a limited number of hole traps available and increasing the sensitivity will fill them faster and decrease the useful lifetime of the MOSFET.

A dosimeter is used to measure the absorbed dose due to ionizing radiation. The threshold voltage shift is converted into an absorbed dose to tissue for a radiation source of quality Q , using:

$$D(Q) = CF(Q)\Delta V_{TH}\Pi k_i \quad (1.24)$$

Where D is the absorbed dose to tissue, CF is the calibration factor, and k_i are the correction factors that take into account dependencies of the detector reading when different from calibration conditions (such as dose rate, energy, temperature, field size, source to surface distance (SSD), angular, and time). MOSFET detectors are calibrated for a given beam quality in water against an ionization chamber that is traceable to the National Standards Laboratory. Using the chamber reading the dose to water can be calculated using TG-51 [32]. The MOSFET is then placed under the same conditions and the threshold voltage shift measured. With the calibration factor known the MOSFET can be placed in a radiation field where the dose is unknown and the threshold voltage shift can be used to determine the dose (provided the differences from calibration conditions does not change the response of the device).

1.8 MOSFET Radiation Response Characteristics

MOSFET response to ionizing radiation involves various dependencies such as energy, dose rate, directional, and temperature. Some of these dependencies will depend highly on device fabrication and so may change from one manufacturer to another.

1.8.1 Temperature dependence

A temperature increase reduces the number of trapped holes affecting the shift in threshold voltage and limiting the accuracy of measurement [33, 34]. Cheung *et al* showed an 8% variation in threshold voltage over a 20 °C variation for a prototype MOSFET from CMRP [35]. Kinhikar *et al* [33, 36] measured a 1.5% under response at 37 °C in comparison to 20 °C for a OneDose sensor. Briere *et al* and Beyer *et al* found an under response of about 3.3% when comparing Sichel's implantable detector at 23 °C to 37 °C [34, 37]. These measurements highlight the importance of establishing the temperature correction factor before clinical use. However, this effect can be minimized when using a dual-MOSFET detector. This works by having two identical MOSFETs directly next to one another operating at different gate biases. After irradiation the difference in the threshold voltage shifts are proportional to the absorbed dose. With both detectors being in the same environment this reduces the temperature dependence to less than 0.015 mV/°C from 0 to 80 °C [38, 39]. With dual bias dual MOSFETs the temperature dependence is decreased by over a factor of 100 and no correction factor is needed [39].

1.8.2 Energy dependence

One of the main disadvantages of MOSFETs is the increased sensitivity at lower beam energies. The energy dependence emerges due to the use of silicon and silicon dioxide in the MOSFET. In figure 1.9a the photon cross section is shown as a function of energy. In figure 1.9b the ratio of the photon cross section for silicon and silicon dioxide to water is shown. At low energies the ratio of the cross-section to water is much higher and changes rapidly with energy. This means that a higher proportion of photons interact. Furthermore, the photons are more likely to interact via the photoelectric effect which deposits a greater fraction of the incident energy locally in comparison to the Compton effect. This causes a larger response in the MOSFET. This becomes problematic when the energy of the beam changes relative to the energy in which the MOSFET was calibrated. Megavoltage photon beams contain photons in this low energy region and so the MOSFET must be calibrated in each radiation modality and field in which it is to be used [16]. When MOSFETs are used in photon beams of low energies (i.e. in the diagnostic imaging energy range: 20 – 150 keV) this is especially problematic because the photon beam quality will change from calibration conditions when interacting with a phantom or patient and cause a large error in measurement. At high photon energies (150 keV – 10 MeV) the ratio of the photon cross sections are much more constant and so a small perturbation in the beam quality when interacting with a patient or phantom should not significantly change the response of the device.

The MOSFET response as a function of energy depends on the structure and encapsulation of the device. The response of the device was found to be constant within $\pm 3\%$ over a range of photon (4 to 25 MV) and electron (5 to 21 MeV) therapy beams [40] [41, 42]. Beyer *et al* found an energy dependence of less than $\pm 1\%$ over the range of Co-60 to 18 MV photon beams [34]. However, Panettieri *et al* found a 12% reduction in response in 18 MV photon beams in comparison to Co-60 [43]. These apparent disagreements speak to the high dependence on device and encapsulation properties. Edwards *et al* found the air kerma sensitivity to be 4.4 times higher at 33 keV than at 6 MV for photons [44]. Wang *et al* found the maximum air kerma sensitivity at 40 keV was over 6 times that of a 6 MV beam [45, 46]. MOSFETs should be calibrated in the beam quality in which they will be used to minimize the error of the measurements. Ramaseshan *et al* found no field size dependence in MOSFETs (5x5 cm^2 to 30x30 cm^2) [41]. For 6 MV

photon beams the MOSFET response increases with depth, but was within 2% of ion chamber measurements [41]. For 18 MV photon beam the response was constant with depth.

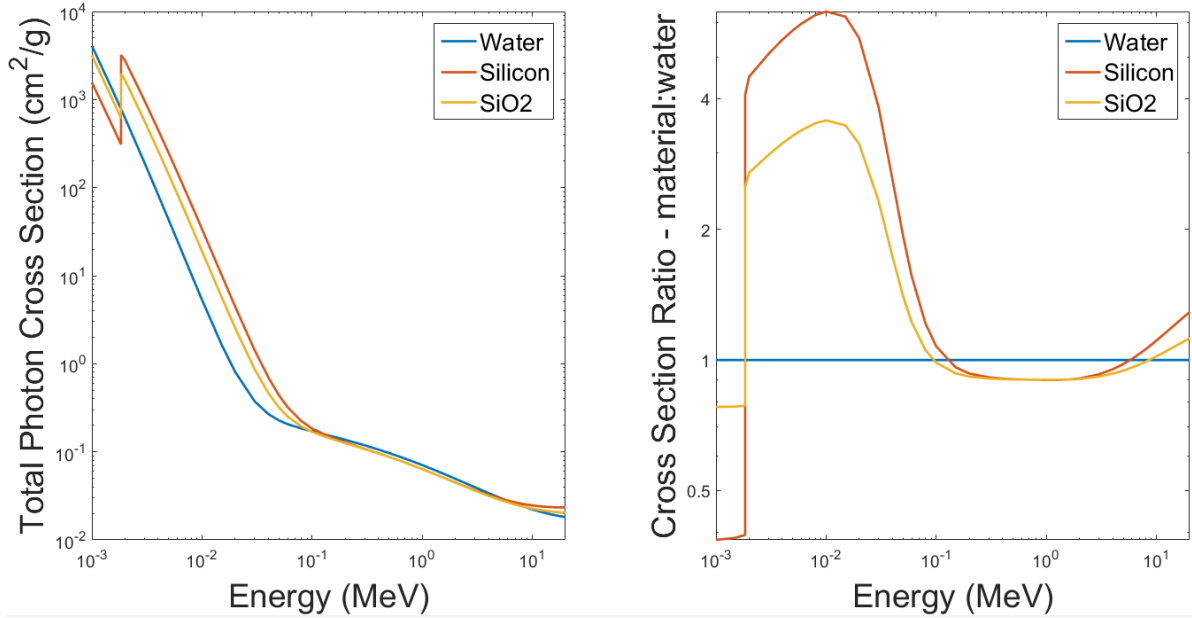


Figure 1.9: On the left is the photon cross section as a function of energy for water, silicon, and silicon dioxide. On the right is the ratio of the photon cross section of those materials to water. At low energies (below 150 keV) the ratio of the cross-sections change rapidly with energy, which leads to an energy dependence. In the megavoltage range the ratio is relatively constant over a range of energies, which leads to little energy dependence for photon beams at those energies.

1.8.3 Directional Dependence

The directional dependence of a MOSFET highly depends on the device design and the geometry of the materials surrounding the detector. In general devices that are irradiated with buildup conditions have less directional dependence than surface or in air measurements [38, 40, 41, 47, 48, 49]. TN dual-MOSFET have been shown to have less than 2.5% response in full buildup conditions for a 6 MV photon beam [47]. MicroMOSFETs have been shown to have an angular response within 3% for photon beams from 75 kV up to 18 MV [41, 50, 51]. Sicel devices have shown an angular dependence of less than 5% without full buildup and within 1.3% in full buildup conditions.

1.8.4 Dose and Dose Rate Dependence

As the exposure to radiation increases, more charge is trapped in the silicon dioxide of the MOSFET. The trapped charge will repel newly created holes leading to fewer trapped holes at the same given dose. The result is a decrease in sensitivity with accumulated dose [34, 52, 53]. Beyer *et al* found a reduction of 40% in the sensitivity over the 80 Gy lifetime of the device [34]. For this reason MOSFETs have a pre-calibration curve given by the manufacturer to correct for the decrease in sensitivity with accumulated dose (no user input required). Using the pre-calibration curve One Dose MOSFETs (Sicel Technologies, Morrisville, USA) were linear in both 6 MV and Ir-192 photon beams [36, 42]. Furthermore, dosimeter readings were independent of dose rates in the range of 80 to 480 cGy/min [42]. MicroMOSFET (Best Medical, Ottawa, Canada) showed a linear response up to 500 cGy in a 6 MV photon beam and no dose rate response [40]. As long as the total irradiation plus anneal time is consistent there is no dependence on the dose per pulse [26].

1.8.5 Time Dependence

A time dependence can emerge due to trapped holes being neutralized, which will decrease the signal and is known as fading. Dual-MOSFET dual-bias detectors had a 3% fading within the first 5 hours and then remained stable up to 60 hours [41]. Less than 2% fading was found for Sicel OneDose sensors in the first ten minutes after irradiation [54]. For irradiations that may take a few hours special MOSFETs should be used that have been designed to have much lower fading. Due to fading, the MOSFETs should be read out at the same time post irradiation each time to minimize the error.

1.9 Organic Semiconductors Response to ionizing irradiation

Mills *et al* measured the response of organic semiconductor in the form of a diode in a 6 MV photon beam [55]. They found a linear increase in photocurrent with dose, showing potential to be used as a radiation detector. For operating voltages of -50 to -150 V the sensitivity was found to be 13 to 20 nC mGy⁻¹ cm⁻³. Similarly, Intaniwet *et al* made a diode with a blend of poly(triarylamine)(PTAA) and 6,13-bis(triisopropylsilylethynyl)(TIPS)-pentacene as the semiconductor [56]. They found

the sensitivity of the devices to 17.5 keV x-rays increased with increasing mobility. Furthermore, they found a linear increase in photocurrent with dose rate.

Raval *et al* irradiated an OTFT with a P3HT semiconductor on a silicon dioxide insulating layer up to 410 Gy using a Co-60 source [57]. They found a decrease in the on current by a factor of 2, an increase in off current by a factor of 150, and a decrease in the mobility. Furthermore, they observed a negative shift in the threshold voltage attributed to positive charge accumulation in the silicon dioxide. Kim *et al* measured the response of a rubrene semiconductor OTFT to electron beam irradiation [58]. For a control device they irradiated a silicon/silicon dioxide substrate before deposition of a rubrene semiconductor. For this device the on and off currents remained about the same, but the mobility fell by about 50% after 10^5 Gy in comparison to pre-irradiation conditions. A second device was irradiated after the deposition of rubrene. This device saw a mobility decrease of more than 50% after 10^3 Gy and no charge transportation after 10^5 Gy. From this they concluded that the response of the OTFT to irradiation was dominated by the response of the organic semiconductor. These results provide promise for organic semiconductor based electronics to be used for the detection of radiation fields.

1.10 Energy Dependence of Organics

In figure 1.10a the photon cross sections of several organics and silicon are shown as a function of energy. The organic materials given in the figure are parylene-C (C_8H_7Cl), parylene-F ($C_8H_4F_4$), PET ($C_{10}H_8O_4$), PMMA ($C_5H_8O_2$), and polyvinyl-F (C_2HF_3). In figure 1.10b the ratio of the photon cross sections for the organics and silicon to water are shown. Below 150 keV the organic materials are more similar to water than silicon and change less rapidly. Furthermore, using a combination of organic materials that under respond and over respond could allow the overall response of the OTFT to be optimized to mimic that of water. This could potentially allow OTFTs to be used across the entire energy range used diagnostically and therapeutically with a single calibration.

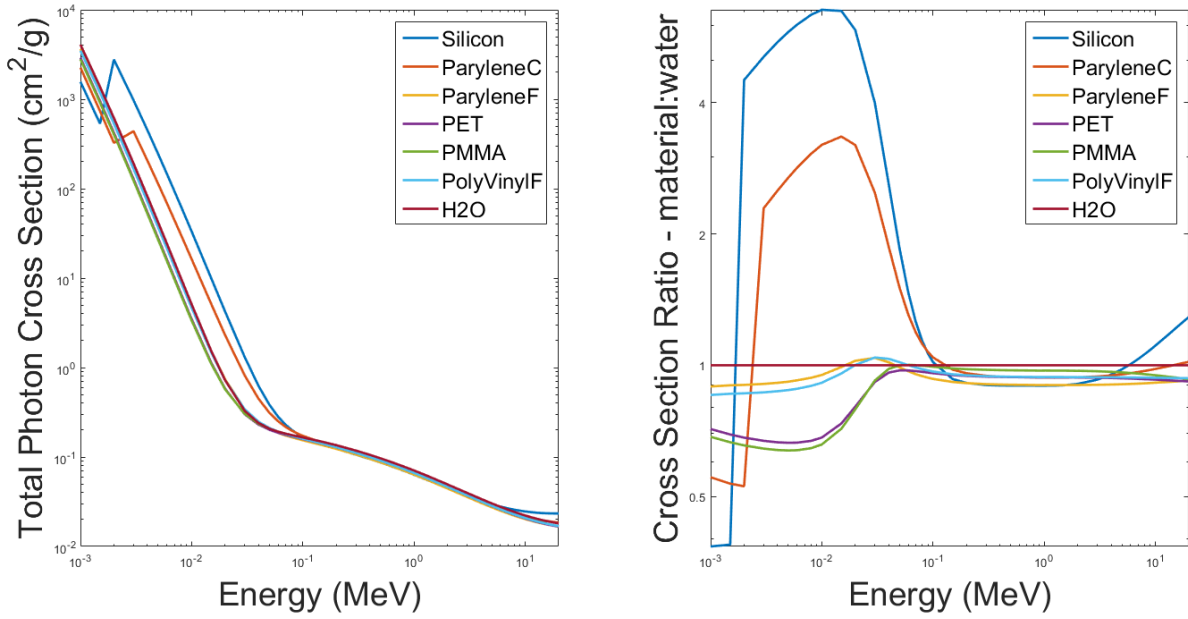


Figure 1.10: The total photon cross sections as a function of energy are shown for several organics and silicon. In comparison to silicon, the organics are more similar to water at energies below 150 keV. This highlights the potential of OTFTs as an energy independent dosimeter. PMMA, parylene-C, and parylene-F are potential dielectrics, while PET is a potential substrate for OTFTs.

1.11 Potential Applications

In this study, OTFTs of novel composition were designed, fabricated and tested in photon beams of various qualities. The objectives of the work were:

- to gain familiarity with the fabrication processes
- to acquire some preliminary data measuring the response of the devices to fields of ionizing radiation
- to characterize the dependence of the devices on energy, direction and dose rate

There are many potential applications of organic electronic devices as radiation detectors. A single element device could prove useful for point measurements in situations that are challenging for conventional dosimeter (e.g. small fields) due to energy dependence or partial volume issues. A 2-dimensional array of devices could be used for evaluating planar dose distributions or fluence patterns. Similarly, a 3-dimensional array could be used for volumetric dose measurements. The small size and flexible substrates

could allow novel in vivo dosimetry applications. Furthermore, the ability to tune the chemical composition of the device could allow for thermal neutron measurements with enriched B-10 or increased low energy photon sensitization with high-Z elements. Given that there already exist commercial products for some of these applications (planar dose measurements in particular), OTFTs will need to demonstrate an advantage over existing technologies if they are to be used clinically in a routine manner. Reduced energy dependence and theoretical reductions in fabrication costs could provide sufficient motivation for their commercialization. The current work aims to provide early evidence that this technology is deserving of further exploration. The work differs from OTFT work done previously due to our use of a flexible substrates, use of various energy photon beams, and use of an organic dielectric differing from silicon-dioxide.

Chapter 2

Methods

In this section the methodologies used for this research will be described. First the fabrication techniques used when making the OTFTs will be described (spin coating, physical vapor deposition, and parylene-C deposition). Next, the steps used for fabricating OTFTs on both a glass substrate and a flexible PET substrate will be described. Then the techniques used for measuring the OTFTs (transfer curves) and extracting the important parameters will be discussed. Finally, the design and parameters used for Monte Carlo simulations will be discussed.

2.1 Fabrication Techniques and Procedures

2.1.1 Spin Coating Process

Spin coating allows a thin film of material to be deposited evenly across a substrate [59]. This is done typically by dissolving the desired material into a solvent. The substrate is held in place on a pedestal with a vacuum (figure 2.1). The solution is placed onto the substrate and the substrate is rotated at high speeds which hurls the majority of the solution off the substrate. An even covering of the substrate is produced by the combination of the centripetal force and the surface tension of the solution. Air flow aids in the drying of the solvent leaving a film of the desired material behind. It may be necessary to place the substrate onto a hot plate to allow the rest of the solvent to evaporate.

2.1.2 Physical Vapor Deposition

Physical vapor deposition is used to deposit a material in a precise pattern [60]. The material to be deposited is placed into a basket (usually tungsten) that has a higher evaporation temperature than the material to be deposited (figure 2.2). Current through the basket is controlled via a power supply. As the current increases the basket and material

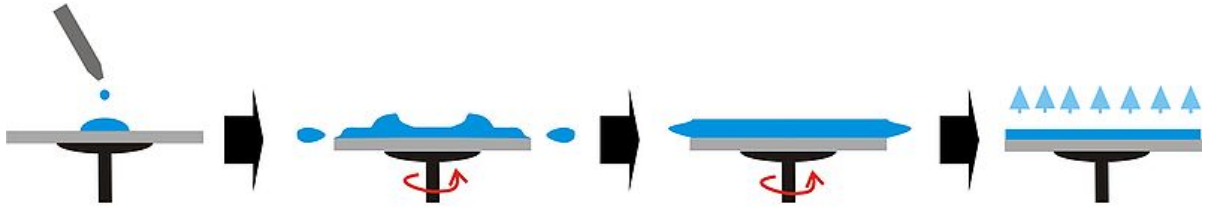


Figure 2.1: Schematic representation of spin coating. The solution is dispensed onto the substrate which is held onto a pedestal via a vacuum. The pedestal rotates quickly forcing some of the solution off the edges of the substrate. The remaining solution evaporates leaving a film of the solute behind.

being held heat up. When the temperature is high enough, the material evaporates and flows away from the basket in straight lines until it contacts a cool surface and condenses. A mask is placed directly in front of the substrate to block the areas where the deposited material is undesired. This process takes place in a vacuum of less than 6×10^{-6} Torr to ensure a low level of contamination. Shutters are placed in front of the substrate to prevent deposition until the desired rate of deposition is reached. Approximately 50 \AA of the material is wasted to ensure any contaminants on the surface of the material are fully evaporated off. When the desired thickness is reached the shutters are closed.

2.1.3 Parylene-C Deposition

Parylene deposition is used to evenly coat a substrate in parylene. Parylene is often used to coat circuit boards because it is a good moisture barrier, has good dielectric properties, and creates a pinhole free film [61]. To start, the substrates are placed into the deposition chamber (SCS Labcoter 2 (Specialty Coating Systems, Indianapolis, USA)). Parylene-C in the form of a dimer is placed into the vaporizer and heated to 176°C to evaporate it (figure 2.3) [62]. The dimer gas then enters the pyrolysis furnace which is heated to 176°C converting the gas into the reactive monomer phase. The monomer gas flows into the

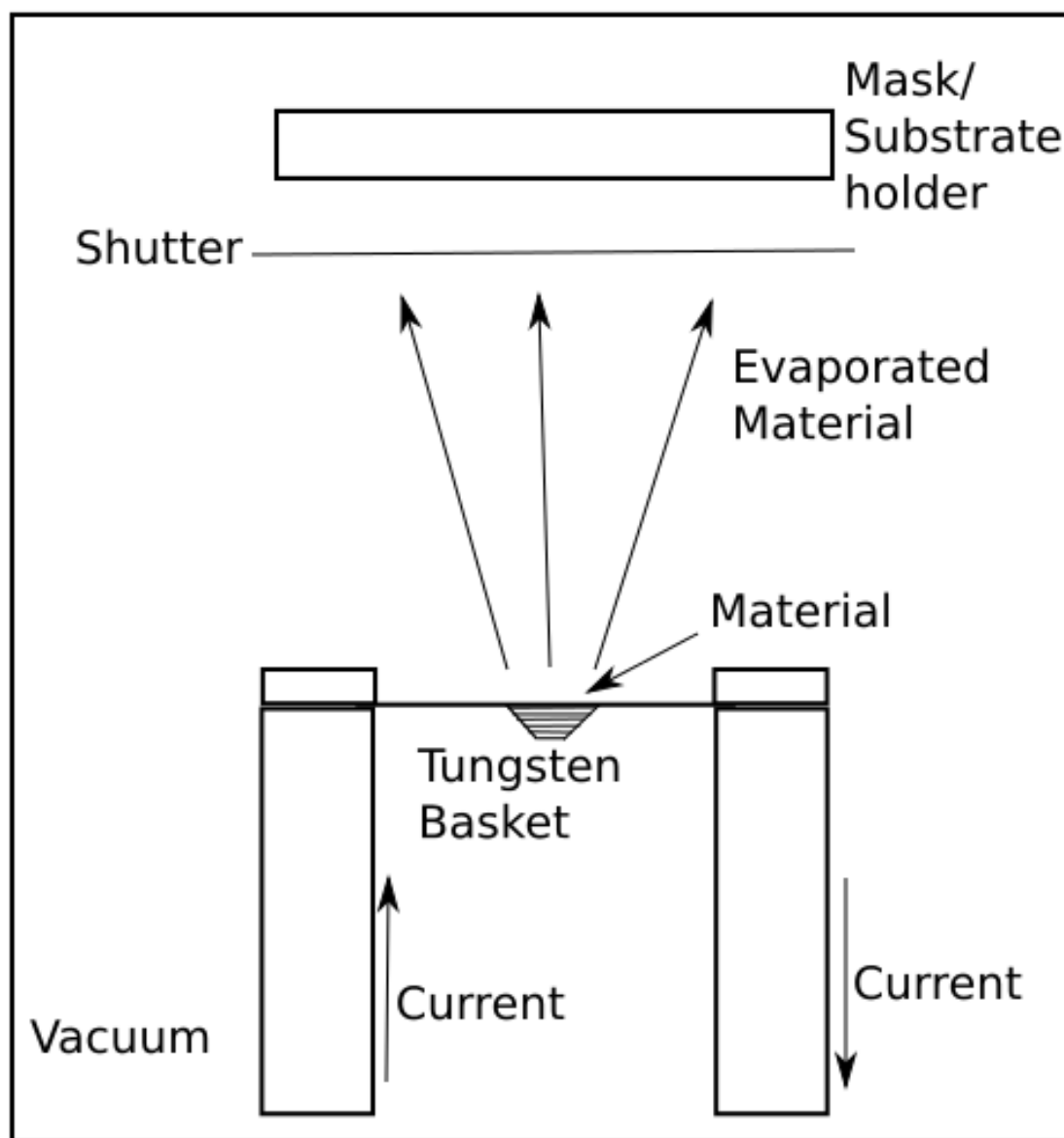


Figure 2.2: Physical vapor deposition is used to deposit a thin layer (50 nm in this study) of material (pentacene, gold or aluminum in this study) in a pattern on the substrate. An external power supply runs a current through the tungsten basket containing the material to be deposited. The current heats up the tungsten basket and material above the evaporation temperature of the material. The material then moves in straight lines until in contact with a cool surface and condenses. By placing a mask directly in front of the substrates the deposited material can be patterned precisely.

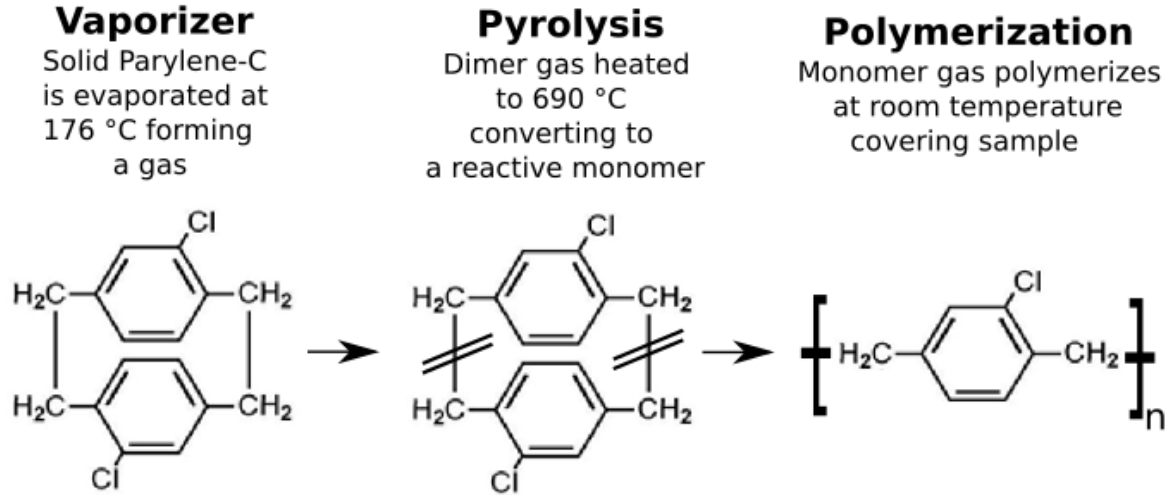


Figure 2.3: Schematic representation of parylene-C deposition. Parylene-C is loaded as a solid dimer in the vaporizer and the substrates are loaded into the deposition chamber. In the vaporizer the solid dimer is heated to 176 °C forming a gas. The gas flows into the pyrolysis chamber where it is heated to 690 °C converting the dimer gas into a reactive monomer gas. The monomer gas flows into the deposition chamber where it polymerizes over all surfaces and creates a uniform film over the substrates. Figure adapted from Reza *et al* [60].

deposition chamber such that the pressure remains at 35 mT and polymerizes at room temperature forming an even film on the device. Between the deposition chamber and vacuum pump is a cold trap to condense any remaining vapors before they enter the vacuum pump and cause damage.

2.2 OTFT Fabrication

Fabrication of OTFTs followed established methods from the literature [63]. The first OTFTs fabricated were on a glass substrate with indium tin oxide (ITO) electrodes (figure 2.4). Initially, the glass is coated in ITO. The ITO device contacts are then patterned by covering contact areas with electroplating tape and placing the slide in 12 M HCl for 10-12 minutes until the non-covered ITO is fully etched away. The slides were then cleaned by sonicating for 20 minutes each in deionized water with Sparkleen, deionized water, acetone, and ethanol. A parylene-C dielectric layer was formed by placing about 300 mg of Parylene-C (~300 nm thick film) into the parylene deposition machine and left to run to completion. To be able to make electrical contact to the

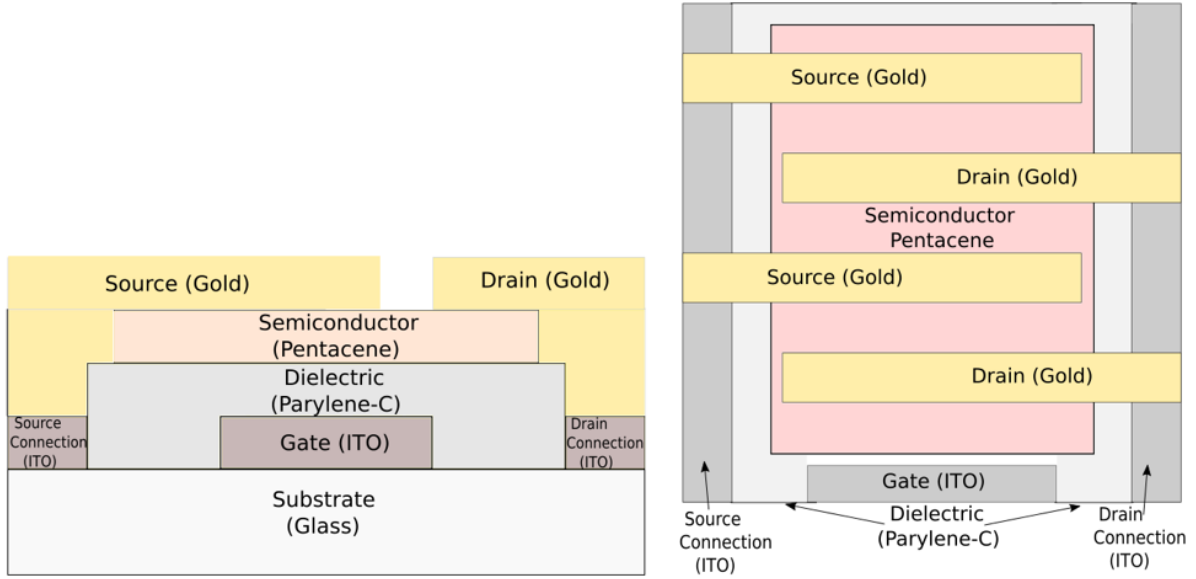


Figure 2.4: On the left is a cross sectional view and on the right a top-down view of the first OTFT fabricated on a glass substrate. The actual device contains 6 gold source leads and 5 gold drain leads, but they are left out to avoid clutter in the diagram. Each of the source contacts and each of the drain contacts are connected together with a strip of ITO.

ITO (i.e. the gate electrode) the parylene-C is cut using a razor blade. Next, pentacene (TCI America, Portland, USA) is deposited using physical vapor deposition at a rate of $\sim 1 \text{ \AA/s}$ with the substrate held at 50°C during evaporation to a thickness of 50 nm. Next the source and drain contacts were patterned using physical vapor deposition to a thickness of $\sim 50 \text{ nm}$ at a rate of $\sim 1 \text{ \AA/s}$. Copper wires were attached with conductive glue to the electrodes to permit easy connection of cabling. A pentacene semiconductor and gold source and drain contacts were used because they have been shown to produce functional OTFTs with high mobility [18, 64]. As explained in the introduction section 1.4, the HOMO of pentacene and fermi level of gold allows for easy charge transportation between the two [18]. Using gold will introduce an energy dependence when irradiated due to having a high atomic number, but we are not interested in fully optimizing an OTFT for energy dependence at this time. After the response of a well understood system is measured, the materials and structure of the OTFT can be optimized for energy dependence. For example graphene could be used in place of the metal electrodes to reduce the effective atomic number of the device [65]. All handling of devices occurred in a clean room when possible.

A new design was implemented to fabricate OTFTs on a flexible PET substrate (figure 2.5). Briefly, a 125 μm polyethylene terephthalate (PET) film (Tekra, New Berlin, USA) was mounted on a glass slide using Polydimethylsiloxane (PDMS). This made spin coating onto PET possible and made alignment during subsequent vapor deposition steps easier. PDMS was made by mixing Sylgard 184A and B (Dow Corning Corporation, Midland, USA) in a 10:1 ratio (polymer to curing agent) and left to sit until all the bubbles have evaporated out of solution (about 30 minutes). The solution is spin coated onto the glass at 2000 rpm for 1 minute, and cured for 30 minutes at 150 $^{\circ}\text{C}$ to facilitate smooth adhesion to the PET. A 50 nm aluminum gate was deposited with thermal evaporation at a rate of $\sim 1 \text{ \AA/s}$. A dielectric layer of either parylene-C or PMMA was then deposited. For PMMA, a 6.0 % by weight solution of PMMA (Sigma-Aldrich, St. Louis, USA) in toluene was spin coated for 60 s at 1000 rpm. The films were heated at 70 $^{\circ}\text{C}$ for 2 h to evaporate residual toluene leaving a dielectric layer of PMMA. For a parylene-C dielectric layer, 300 mg of parylene-C was placed into the deposition system and left until all of the material was deposited. Thermal evaporation was used to deposit a 50 nm pentacene layer at a rate of $\sim 1 \text{ \AA/s}$ with the substrate held at 50 $^{\circ}\text{C}$ during evaporation. Source and drain electrodes were made by thermally evaporating gold at a rate of $\sim 1 \text{ \AA/s}$ to a thickness of 50 nm. The OTFT was encapsulated with $\sim 1 \mu\text{m}$ of parylene-C. The source-drain electrodes were deposited in an interdigitated configuration with at W/L of 125. To permit easy connection of cabling, copper tape was attached to the gold electrodes.

2.3 OTFT Irradiation Setup

OTFTs were irradiated with both an Xstrahl 300 orthovoltage x-ray unit (Xstrahl Ltd., Surrey, UK) (100 and 180 kVp) and a Varian Clinac 21EX (Varian Medical Systems, Inc., Palo Alto, USA) medical linear accelerator (6 and 18 MV photons). For the orthovoltage irradiations, a 5 cm diameter, 30 cm length cone was used to deliver dose to the OTFT (figure 1.6). OTFTs were placed on top of a 15 cm stack of Solid Water (Sun Nuclear Corp., Melbourne, USA). For the megavoltage irradiations, the OTFTs were placed at isocenter with a 5x5 cm^2 field size. The OTFTs were positioned on top of a 10 cm stack of Solid Water and below an additional 5 cm of Solid Water (figure 1.7). To prevent the build up material from damaging the OTFTs, 3 mm shims of PMMA were used to

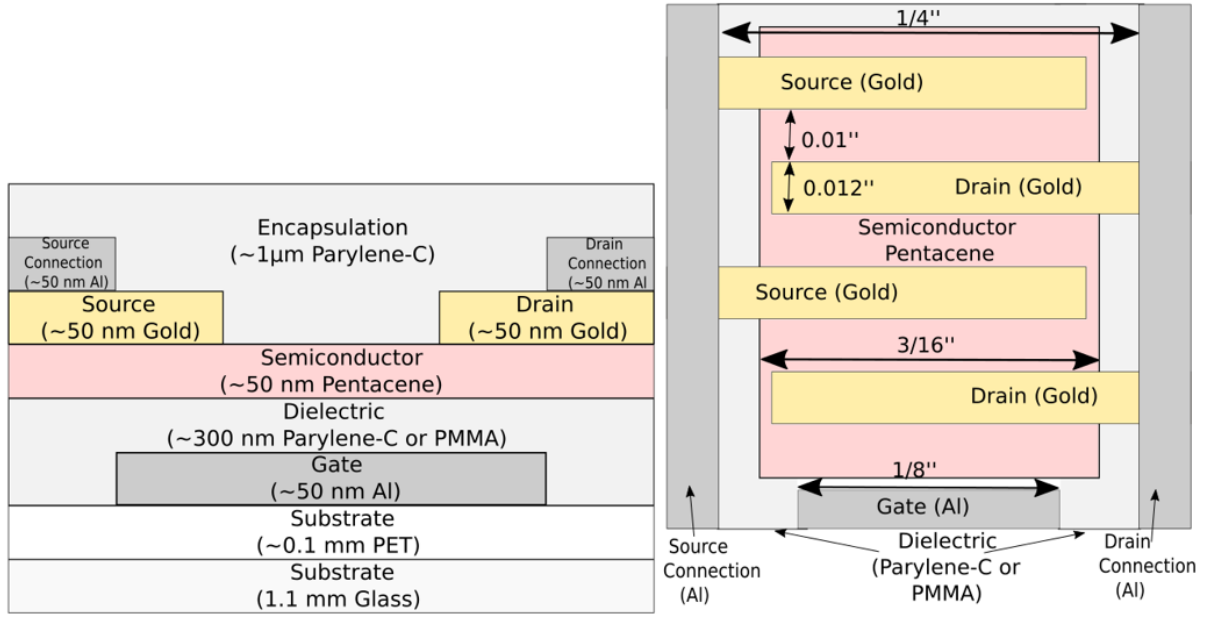


Figure 2.5: On the left is a cross-sectional view and on the right is a top down view of the OTFTs fabricated on a flexible PET substrate. There are 6 gold source contacts and 5 gold drain contacts, but are not included in the figure. With this configuration the source and drain contacts were connected together using an aluminum strip on top of the contacts.

maintain a small air gap (~ 2 mm) between the top of the OTFT and the bottom of the Solid Water. All machine outputs were measured with a calibrated ionization chamber. For each setup an ionization chamber was used to measure the dose. Next, the number of monitor units was adjusted to ensure the dose delivered was accurate.

During irradiations a dual channel source measurement unit (SMU) (Keithley 2614B, Tektronix, Inc., Beaverton, USA) was used to apply a +10 V bias across the OTFT dielectric (source and drain contacts were shorted to ground potential). The SMU was also used to measure transfer curves prior to the initial exposure ($n = 5$) and then following each exposure. Curves were measured at 10 Gy and 20 Gy intervals for the kilovoltage and megavoltage photon beams, respectively. After initial experiments, all transfer curves were measured with V_{DS} held constant at -50 V and the V_{GS} swept from +10 V to -50 V and back to -10 V in 1 V steps. Important parameters such as threshold voltage (V_{TH}), mobility (μ), and the on/off current ratio (I_{ON}/I_{OFF}) were extracted from the transfer curves.

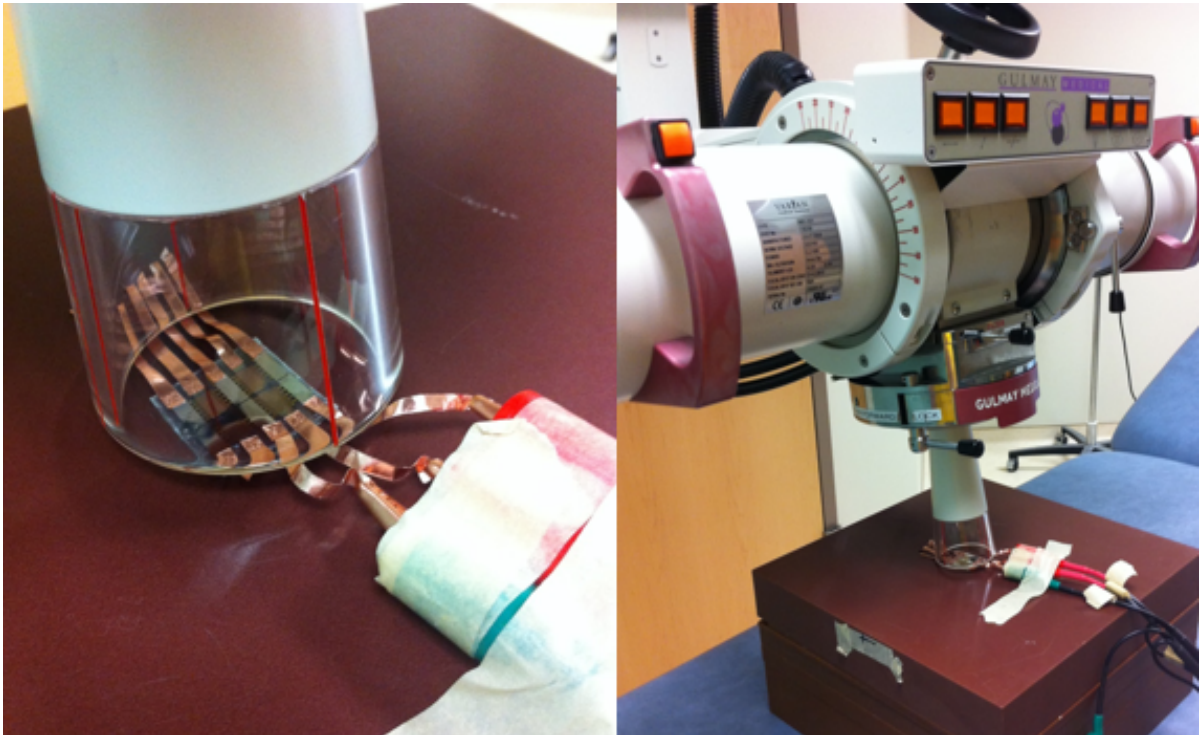


Figure 2.6: Orthovoltage irradiation setup. The substrate consists of 4 OTFTs and the one being measured is aligned to the center of the cone. The OTFT is placed on top of 15 cm of solid water located 30 cm from the source.



Figure 2.7: MV irradiation setup. The OTFT is placed on top of 10 cm of solid water with 5 cm of solid water on top. To ensure the solid water on top of the OTFT does not damage the device it is propped up with 3 mm shims of PMMA (white in picture) to ensure a small air gap (~ 2 mm) between the OTFT and solid water. The OTFT is placed 100 cm from the source with a 5×5 cm² field size.



Figure 2.8: Directional dependence measurements. The OTFT was located at isocenter with a field size of $5 \times 5 \text{ cm}^2$. The device was irradiated at 0° (figure 2.7), 90° (left image), and 180° (right image). Ion chamber measurements were performed to ensure equal dose to the OTFT at each angle. During directional dependence irradiations the white PMMA shims were modified so that they did not protrude beyond the solid water (shown in figure) and were made such that the device was at a depth of 10 cm when irradiated at 90° .

2.4 Directional Dependence

Directional dependence of the OTFT was measured using an 18 MV photon beam. The OTFT was positioned at isocenter and the response was measured at beam incidence angles of 0° , 90° , and 180° . Buildup of 10 cm of solid water was used at angles of 0° and 90° . At 180° there was 5 cm of solid water plus the couch. At each geometry ion chamber measurements were performed and monitor units were adjusted appropriately to ensure consistency with respect to delivered dose.

2.5 Extracting important Parameters

In section 1.5 of the introduction the method and equation for extracting the mobility and threshold voltage from the drain-source current (I_{DS}) as a function of the gate-source voltage (V_{GS}) is described. The on-current and off-current are found by taking the maximum and minimum I_{DS} measured, respectively. This means that the on-current is found at the most negative V_{GS} measured and depends on the range that V_{GS} is swept. For this reason the acquisition parameters were kept the same from one device to another where possible. To extract the threshold voltage, mobility, on-current, and off current requires a sweep of the OTFT over a range of biases. To use an OTFT to measure dose clinically it would be advantageous if one measurement could be used to calibrate the device. For this either the change in V_{GS} was measured at a constant I_{DS} or the change in I_{DS} was measured at a constant V_{GS} . For both of these analyses, the changing parameter was extracted by interpolating between data points on the transfer curves. This allowed us to extract the important parameters above, while also showing the proof of concept of the quicker measurement.

2.6 Monte Carlo Simulations

Monte Carlo simulations using DOSXYZnrc were used to investigate the intrinsic energy dependence of proposed device designs (i.e. materials, thicknesses and geometries) [66]. To assess the energy dependence of the OTFT the perturbation factor was calculating using:

$$P = \frac{D_W}{D_{det}} \quad (2.1)$$

Where D_W is the dose to water in the position of the OTFT had the OTFT been replaced with water and D_{det} is the dose measured in the OTFT. The doses used to calculate the perturbation factor were the doses to the dielectric material of the OTFT because the dielectric is the active material responsible for the dose response of a MOSFET and an assumption was made that similar mechanisms may be responsible for signal generation in OTFTs.

The first Monte Carlo simulations were a simplistic 1x1x9 voxel simulation shown in figure 2.9. The length and width of each voxel was 1 cm and the material and thickness of each voxel was varied. This layered design was used to increase the speed of

Top Coat 1	Water
Top Coat 2	Water
Top Coat 3	Water
Semiconductor	Water
Dielectric (Dose Scoring Voxel)	Water (Dose scoring Voxel)
Gate	Water
Substrate 1 (Same as Top Coat 3)	Water
Substrate 2 (Same as Top Coat 2)	Water
Substrate 3 (Same as Top Coat 1)	Water

Figure 2.9: On the left is the simplistic design of the OTFT. Each voxel has a length and width of 1 cm and varying thickness depending on the simulation. On the right is the OTFT replaced completely with water with the exact same dimensions. The dose is scored to the voxel of the dielectric material.

simulations to understand what materials and what thicknesses may be a good starting point for optimizing an OTFT device. For this we use three substrate layers on the bottom and three top coating layers on the top that mirrored each other to reduce directional dependence. The layers in the middle simulate the gate, dielectric, and semiconductor. For these simulations the OTFTs were suspended in air and irradiated with monoenergetic photon beams from 20-100 keV.

The second Monte Carlo simulation was used to model our irradiated OTFTs shown in figure 2.5. These simulations used photon beam spectra incorporated into DOSXYZnrc of energies Co-60, 6 MV, 10 MV, and 15 MV. The OTFT was placed in a 10x10x15 cm block of water at a depth of 5 cm and located 100 cm from the source. At each energy the OTFT was irradiated at photon beam incident angles of 0°, 90°, and 180°. Each simulation used 4×10^9 incident photons.

A brief description of the parameters of interest for the simulations and the values used are listed below, but a more complete description can be found elsewhere [66]:

- Electron cutoff energy (ECUT) – Once an electron has less energy than ECUT it deposits the rest of its energy locally (in the voxel in which it is currently located). For the simulations a cutoff energy of 512 keV was used, meaning that any electron with a kinetic energy less than 1 keV was cutoff (rest mass of electron is 511 keV).
- Photon cutoff energy (PCUT) – A photon with energy less than the PCUT will

deposit the rest of its energy locally. Set to 1 keV for the simulations.

- Electron Boundary Algorithm – This controls the algorithm used to transport electrons across boundaries. For the simulations, the EXACT algorithm was used which transports electrons in single elastic scattering mode when the electrons are within a distance from the boundary given by the skin depth for boundary crossing algorithm (BCA).
- Skin depth for BCA – When using the EXACT algorithm the skin depth for BCA is the perpendicular distance in units of elastic mean free paths, to the region boundary when the electron transport will be in single elastic scattering mode. The default value of 3 was used which has been found to give peak efficiency [66].
- Electron step algorithm – The algorithm is used to calculate the lateral and longitudinal corrections to account for elastic scattering for a condensed history electron step. PRESTA-II was used for the simulations.
- Bound Compton Scattering – Used to determine if Doppler broadening and binding effects are simulated in Compton scattering events. This was turned on because bound Compton scattering is important at low energies and if Rayleigh scattering is being simulated.
- Rayleigh scattering – Determines whether Rayleigh scattering is simulated or not. This was turned on because low energy photons are simulated in this work.
- Atomic relaxations – Determines whether the relaxation of atoms to their ground state are simulated following a Compton or photoelectric event. Atomic relaxations are important at low energies and were turned on for the simulations.

Chapter 3

Results

In this section, the results of device fabrication and response to irradiation will be presented. First the design change of the OTFTs from a glass substrate to a flexible PET substrate will be described, along with the reasons for the changes. Next the difficulties in fabrication and measurement will be presented, with the change in methods and the resulting electrical properties of the OTFTs. The response of the OTFTs will be presented for each of the photon beam qualities used. The longevity, directional dependence, and dose rate dependence of the OTFTs will be presented. Finally, the simulated perturbation factors of OTFTs simulated with Monte Carlo will be presented.

3.1 Designing new OTFTs

Originally OTFTs were made on a glass substrate, with ITO electrodes, parylene-C dielectric, and a pentacene semiconductor (figure 2.4). From that design we wanted to move to a more tissue-equivalent, flexible substrate. Doing so, however, led to several challenges. First, a PET substrate was chosen, but unlike the glass substrates the PET was not coated in a conductive material. An aluminum gate was chosen because it has a low atomic number relative to most conductive materials and should have less energy dependence. A second problem with the new design was contacting the electrodes. Depositing parylene-C as a dielectric layer evenly coats the entire device including the contacts. For the glass/ITO devices a razor blade was used to scrape the parylene-C off of the areas needed for contact. Using a razor blade with the new design would result in removing the aluminum contact as well. Instead, contact to the aluminum gate was made before the deposition of parylene-C. Rather than using copper wires with conductive glue as before, we used a conductive copper tape because it stayed in place more effectively.

An improvement over the first design (glass substrate, figure 2.5) was made by depositing the source and drain electrodes last to make easier connection. With the interdigitated design, each of the contacts needed to be connected together. This was

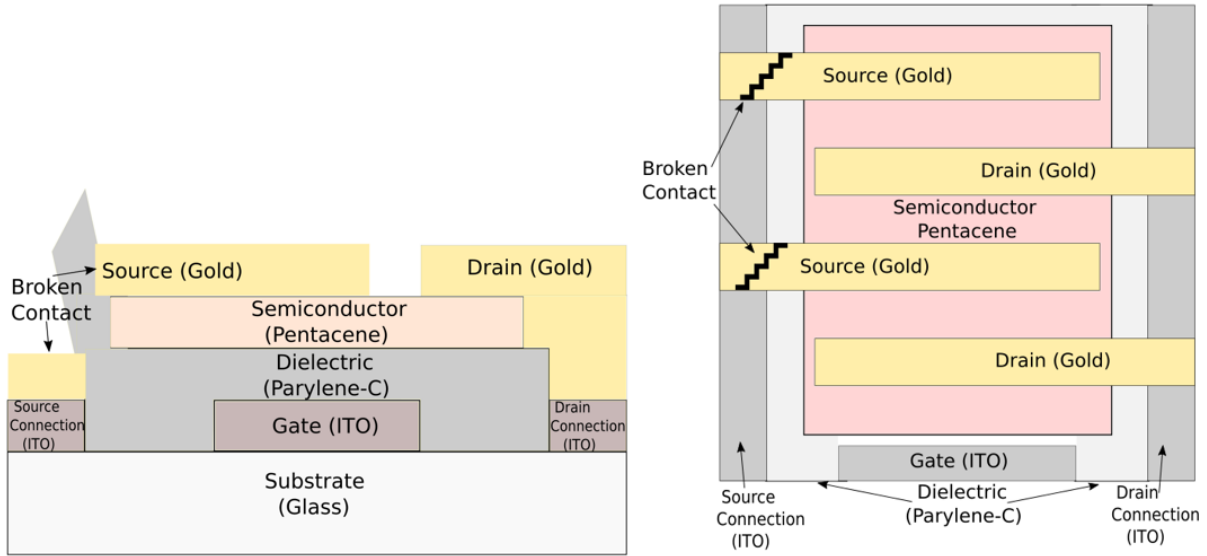


Figure 3.1: On the left is a cross-sectional view and the right a top view of the old device. This illustrates that if the parylene-C is not cut smoothly and peels at the edge, it will break the contacts from the gold source or drain contacts to the aluminum strips that connects them together.

problematic with the old design because cutting the parylene-C often made a ledge over which the individual digits could not make contact with the connecting strip (figure 3.1). This meant that many devices were not functional, but with the new design this problem was avoided. Gold was deposited to form the interdigitated design and then a connective strip of aluminum overtop to connect them together.

3.2 Fabrication Challenges

When glass slides are placed into the masks for thermal deposition there is very little room for movement, which makes alignment easy. PET being flexible, it is harder to align because it can bend to fit in the mask if cut too big or can move around if cut too small. Furthermore, the response of the OTFT to bending is unknown and so care should be taken initially to reduce the bending as much as possible. To overcome these problems, we decided to mount the PET onto glass slides which would fit the masks well and would give a rigid support for the PET. To mount the PET onto glass there were two requirements. First, the adhesion should be temporary so that the PET can be removed from the glass after fabrication. Second, the adhesion layer must be smooth so that the deposition of subsequent layers are also smooth. PDMS was chosen as the

temporary adhesion. PDMS is spin coated onto the glass forming a smooth PDMS layer and then the PET can be lightly pressed on. Sticking PET onto glass had the additional benefit of making spin coating onto PET possible which was useful when the dielectric would later be changed from parylene-C to PMMA.

3.3 Substrate Preparation

Most of the OTFTs made in the first batch did not function as transistors, but with improvements in the cleaning methods a much higher yield was achieved. Many of the OTFTs were reaching “compliance” on the gate (current greater than 0.01 A). This indicates that the current between the gate and drain was high, even when the device was biased to be turned off, which means that the resistance between the gate and drain is too small. This led us to believe that the dielectric material, which should isolate the gate electrode, was not functioning as intended. This could be due to a short through the dielectric material. The cause of a short could be from dust or from large extrusions or scratches on the PET substrate. To overcome this, two solutions were tried. For both, all handling of PET occurred in the clean room. The first solution was to use a lens brush to brush dust off the PET before the usual sonication steps used for cleaning (fifteen minutes sonicating in sparkleen and deionized water and fifteen minutes in deionized water). Second, a thin PMMA film was spin coated onto the PET to make a smoother layer in case the surface of the PET was too rough. After some investigation, it was decided that using the lens brush and sonicating the PET substrates was enough to produce functional OTFTs and so the additional step of spin coating PMMA was no longer used. Figure 3.2 shows transfer curves of some of the first OTFTs before and after the new cleaning method. New cleaning methods yielded a much higher percentage of functional OTFTs in a given batch.

Next, the thickness of the parylene-C layer was investigated. Thicknesses of approximately 100 and 300 nm were deposited based on previous calibration curves. Figure 3.3 shows the transfer curves of a batch of OTFTs made with the two thicknesses. For a given V_{GS} the electric field drops off linearly with distance (equation 1.12). This means that the charge buildup drops off linearly with distance and causes a lower current to be created at a given voltage for a thicker dielectric. Furthermore, it shifts the threshold voltage because a larger bias is needed to create the accumulation of charge initially [64].

In table *I* is a summary of the important parameters for the two sets of devices. Also in the table are the important parameters of the devices shown previously that were fabricated with the new cleaning methods (approximately 300 nm parylene-C). The devices shown previously are going to be referred to as the old batch and were included to highlight incremental improvements in device performance. Between the old batch and this experiment the transfer curves were measured with a different V_{DS} and over a different range of V_{GS} . However, some comparisons can still be made. The off current was $(2.8 \pm 2.0) \times 10^{-8}$ A (n=6), $(1.1 \pm 0.8) \times 10^{-8}$ A (n=8), and $(4.0 \pm 3.3) \times 10^{-9}$ A (n=7) for the old batch (300 nm parylene-C), 100 nm parylene-C, and 300 nm parylene-C, respectively. The error given is the standard deviation of the batch of devices. The mobility was calculated based on the thickness calculated from previous calibration of the parylene-C layer and using a relative permittivity of 3.1. The measured mobilities were 0.09 ± 0.03 , 0.43 ± 0.04 , and 0.29 ± 0.02 cm²/V.s for the old batch (300 nm parylene-C), 100 nm parylene-C, and 300 nm parylene-C, respectively. The increased mobility and lower off currents from the old batch to the new batch may have been due to more careful fabrication and less exposure to air between fabrication steps. In terms of reproducibility (variance of mobility, threshold voltage, etc.) and quality of devices the 100 nm parylene-C and 300 nm parylene-C were similar. Following this comparison study, subsequent devices used 300 nm of parylene-C because MOSFET dosimeters have been shown to have increased sensitivity to ionizing irradiation with increased thickness of the dielectric.

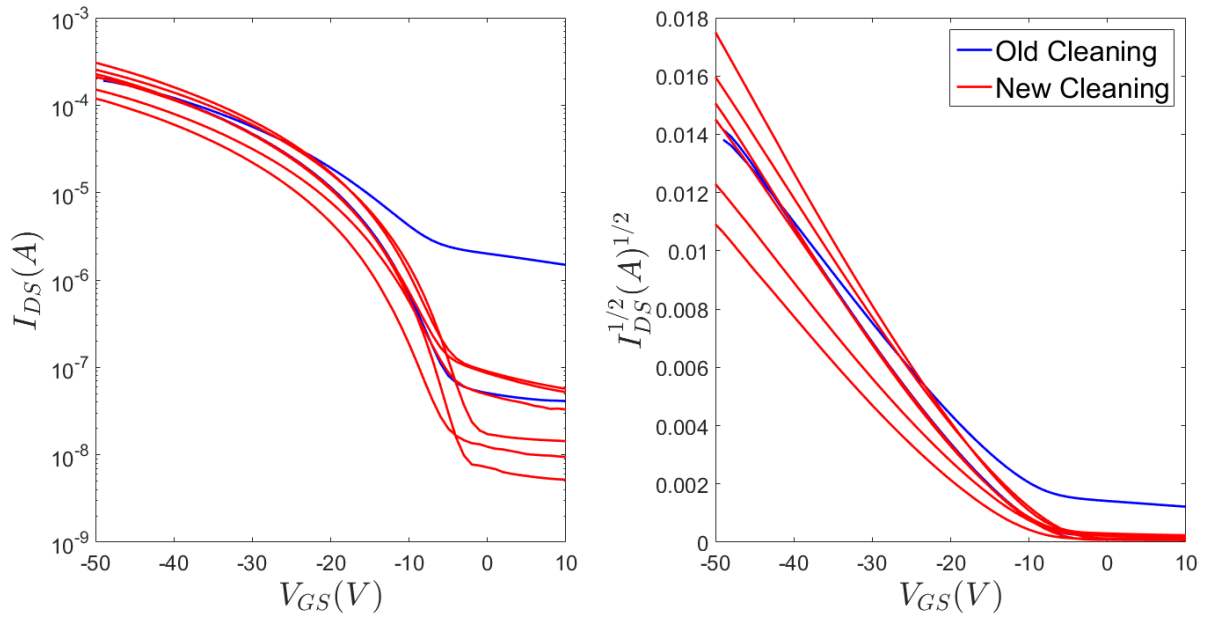


Figure 3.2: Transfer curves of the first functional devices (blue) and after improving the cleaning techniques (red). Cleaning was improved by using a camera brush to brush off the dust on the PET in addition to sonicating the PET. Before the improved cleaning technique, many of the devices were reaching gate compliance and did not function as transistors (not shown). After cleaning was improved a much higher percentage of devices were functional.

Table I: Important OTFT parameters such as threshold voltage (V_{TH}), mobility (μ), on current (I_{ON}), and off current (I_{OFF}) are given for the old batch, a new batch with 100 nm Parylene-C dielectric and a new batch with 300 nm Parylene-C dielectric. The mobility and off current improve with the new batches. The error stated is the standard deviation from the batch.

	V_{TH}	$\mu(\text{cm}^2/\text{V.s})$	$I_{ON}(A)$	$I_{OFF}(A)$
After Cleaning (Old batch)	-13 ± 1	0.09 ± 0.03	$(2.5 \pm 0.7) \times 10^{-4}$	$(2.8 \pm 2.0) \times 10^{-8}$
100 nm Parylene-C	-6.4 ± 0.7	0.43 ± 0.04	$(5.8 \pm 0.7) \times 10^{-4}$	$(1.1 \pm 0.8) \times 10^{-8}$
300 nm Parylene-C	-13.2 ± 1.0	0.29 ± 0.02	$(8.5 \pm 2.0) \times 10^{-5}$	$(4.0 \pm 3.3) \times 10^{-9}$

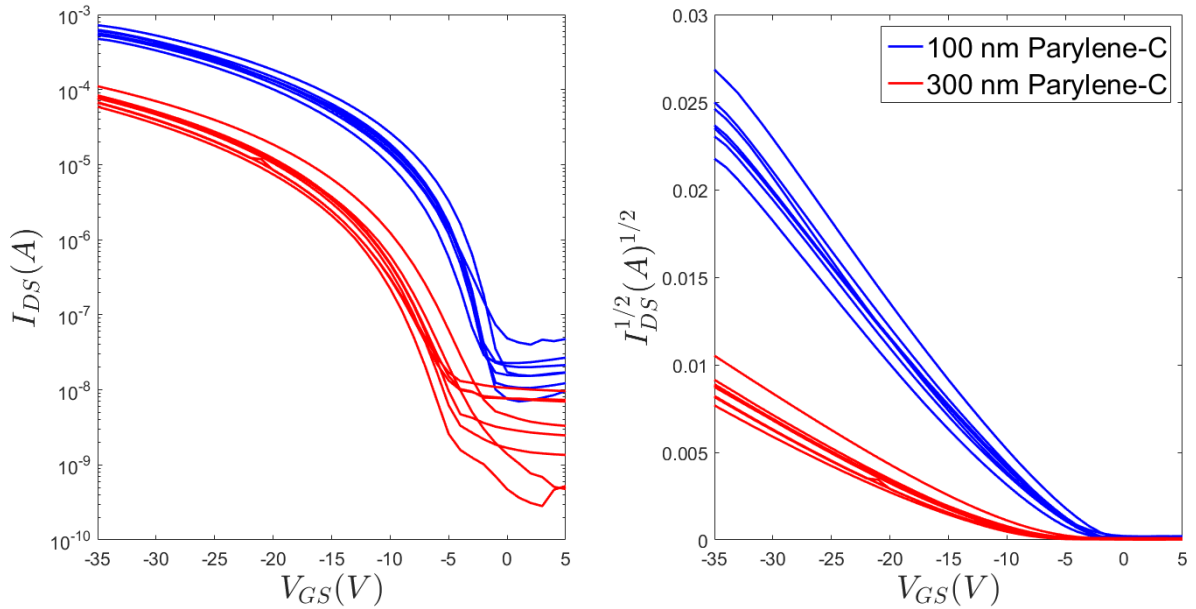


Figure 3.3: Transfer curves of OTFTs made with 100 nm parylene-C dielectric (blue) and 300 nm parylene-C dielectric (red). A thicker dielectric has a reduced current at a given bias, which is expected because a greater bias is required to produce the same electric field with a thinner dielectric. Going forward the 300 nm dielectric was used because MOSFETs have been shown to have increased sensitivity to irradiation with dielectric thickness.

3.4 Response to Irradiation

An OTFT with a 300 nm parylene-C dielectric layer was irradiated with a 180 kV photon beam as described in section 2.3. Transfer curves were measured after each increment

of dose (increments varied between 1 and 10 Gy) and shown in figure 3.4. As a general observation, the on current decreased with dose to the OTFT. In figure 3.5 the threshold voltage shift as a function of accumulated dose is shown. The threshold voltage shift is more sensitive to dose initially, and then lessens with accumulated dose. A total shift of about +2.8 V over a 160 Gy was measured. Mobility of the OTFTs were extracted from the transfer curves as described in section 1.5. Figure 3.6 shows the normalized mobility as a function of accumulated dose where the mobility is normalized to the mobility before irradiation. Over 160 Gy, there is over a 20% reduction in mobility. Mobility and threshold voltage were extracted from the transfer curves. A clinical system would likely require a simpler readout circuit; probably one in which a fixed voltage is used to drive a measured current or one in which the voltage required to drive a given current is measured. Figure 3.7 shows how the current changes at a given gate bias as a function of dose. This data is extracted from the transfer curves, but could be extracted as a single point measurement in a future prototype after further characterization of the devices. This would have the advantage of greatly simplifying and reducing the cost of the readout circuitry since voltages across electrodes would not need to be swept (e.g. with a costly source meter unit as was used in this work). At 0 V the current is very noisy, but at -49 V the current decreases with dose and is approximately linear over that span. A common way to use MOSFETs as radiation detectors is to measure what bias is required to drive a given current. Again we have extracted this data from the transfer curves taken previously. To drive a current of 0.25 mA the gate voltage changes from approximately -52.5 V to -56 V over the 160 Gy (figure 3.8). The voltage shift per unit dose is larger than the threshold voltage change per dose and is more linear. At a constant current of 2 and 50 μ A there was a smaller shift in voltage and less linearity than at a constant current of 2.5 mA.

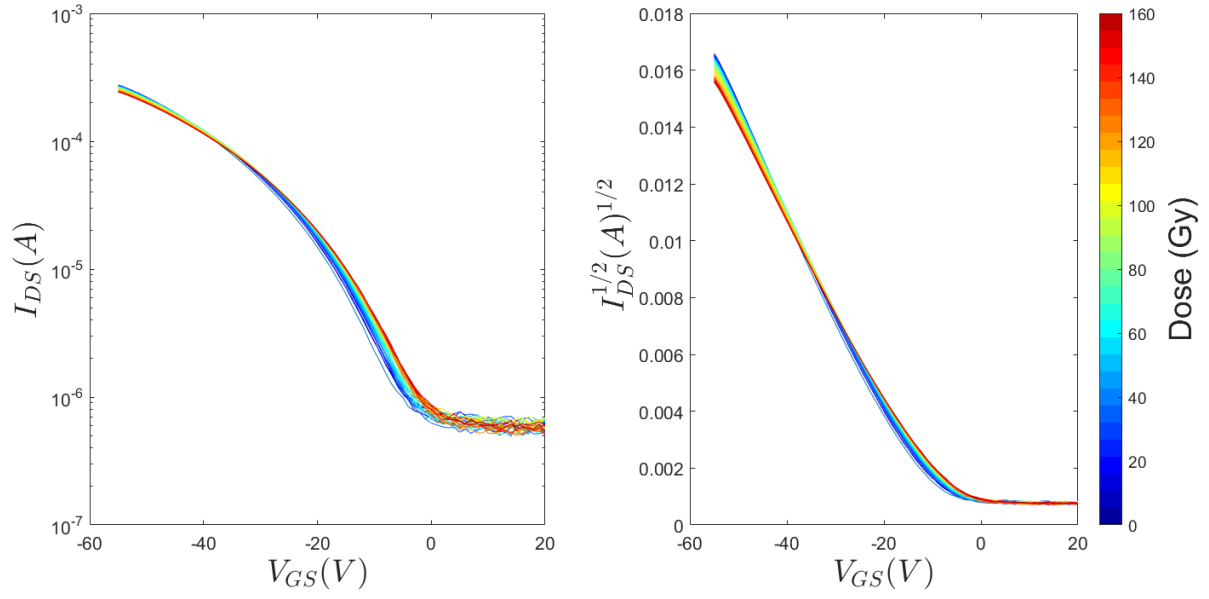


Figure 3.4: Transfer curves of the first irradiated OTFT made with a 300 nm parylene-C dielectric layer. The OTFT was irradiated with 180 kVp photon beam up to 160 Gy. The on current decreased with increasing dose. The off current was quite noisy, but just above the threshold voltage (about -10 V) current increased with accumulated dose.

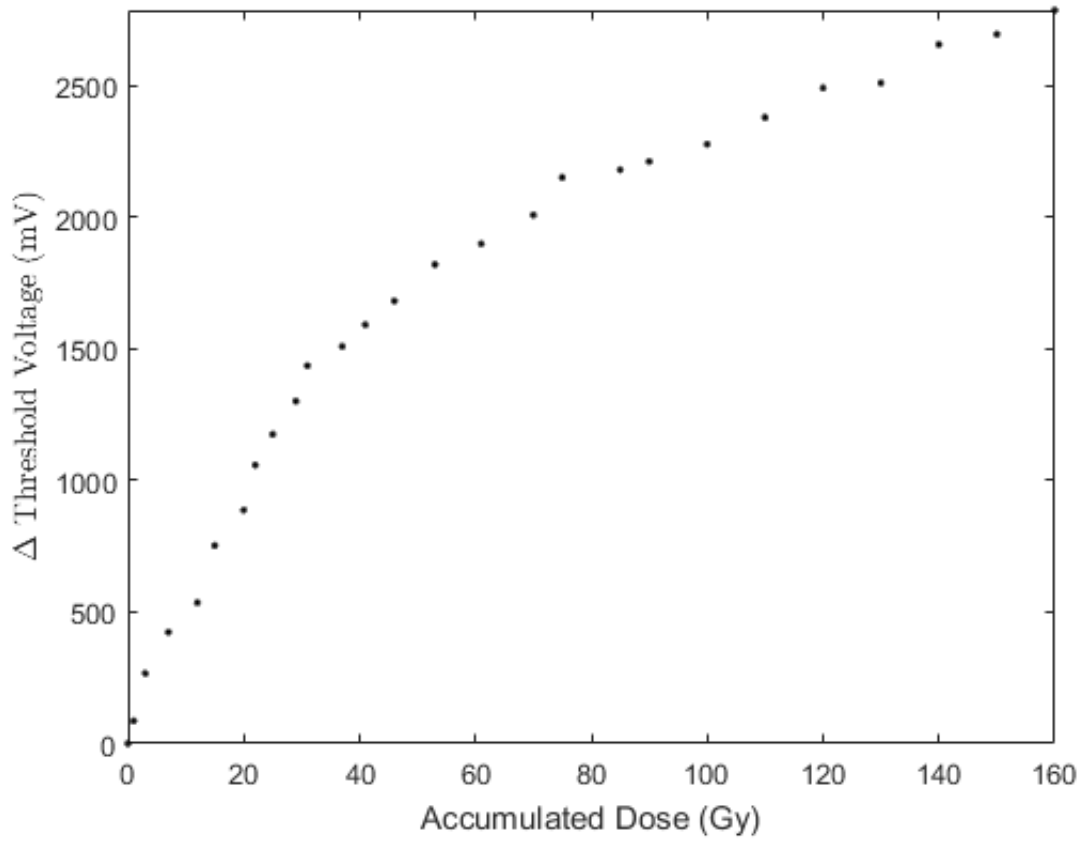


Figure 3.5: Change in threshold voltage as a function of dose as extracted from the transfer curves shown in figure 3.4. The OTFT had a 300 nm parylene-C dielectric layer and was irradiated up to 160 Gy with a 180 kVp photon beam. The threshold voltage shifted positively as a function of accumulated dose. A greater shift occurred for a given amount of dose at low accumulated doses (less than 40 Gy), than for higher accumulated doses (greater than 40 Gy).

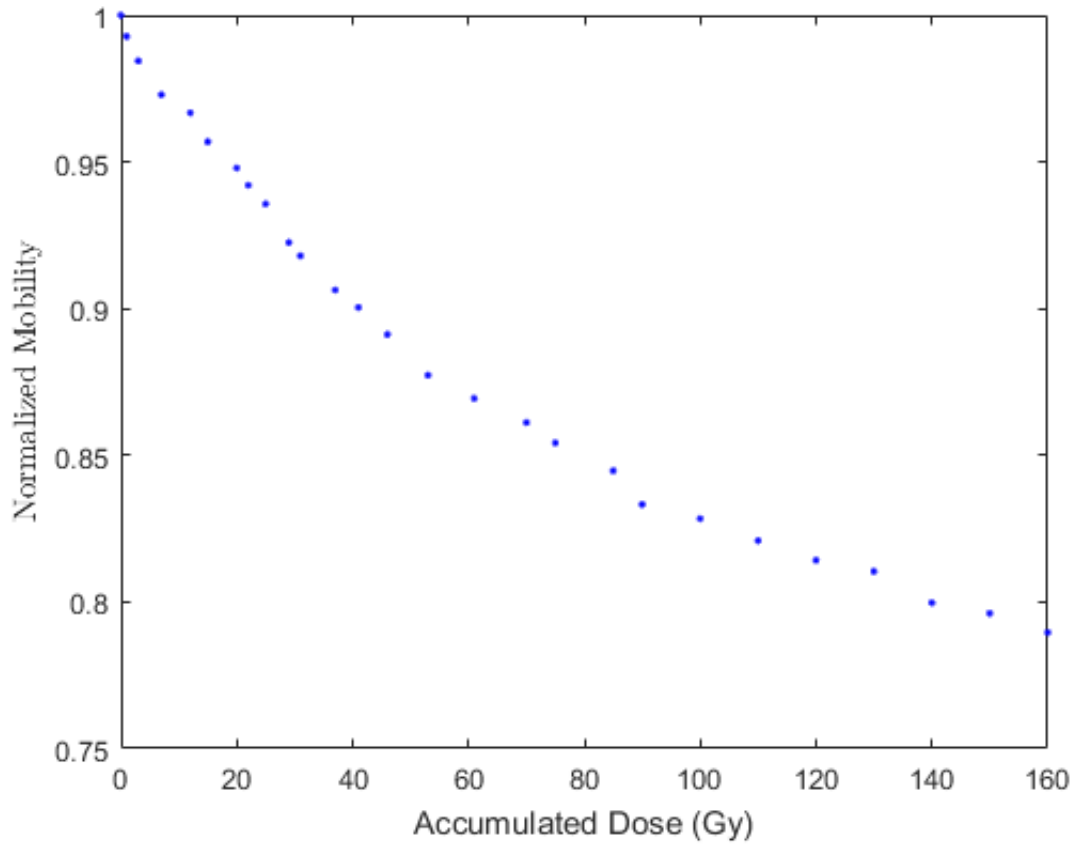


Figure 3.6: Change in the normalized mobility as a function of accumulated dose for an OTFT made with a 300 nm parylene-C dielectric layer and irradiated with 180 kVp photon beam. The mobility was extracted from the transfer curves in figure 3.4 and normalized to the mobility before irradiation. The mobility decreased as a function of accumulated dose, with an approximate 10% reduction after 40 Gy and more than a 20% reduction after 160 Gy.

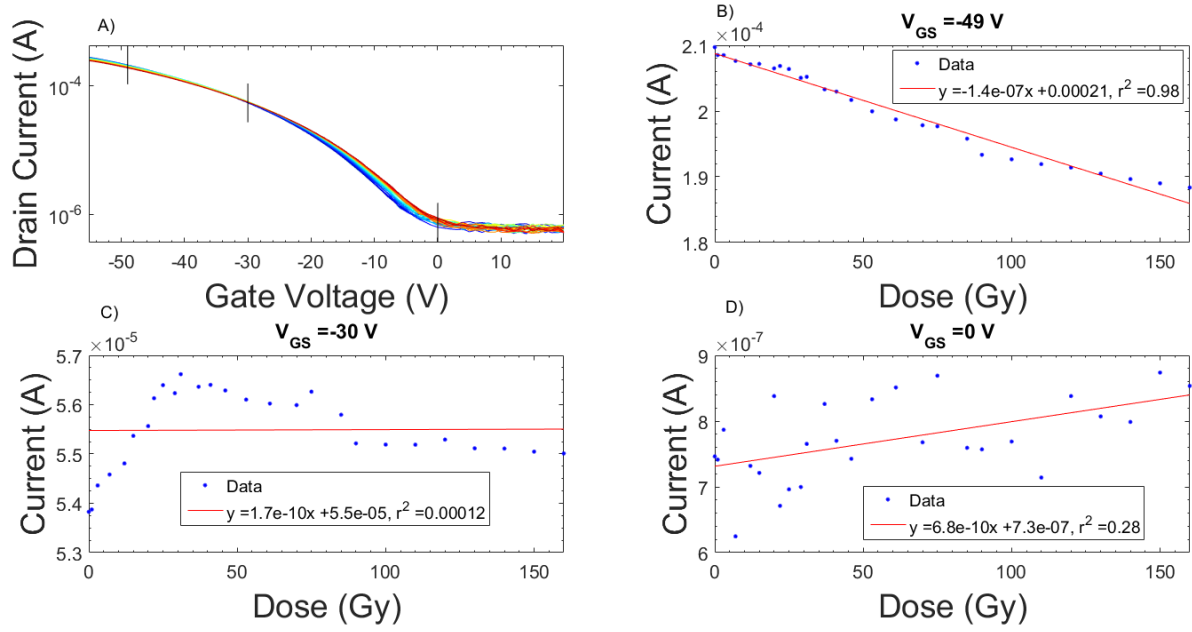


Figure 3.7: Part a) shows the transfer curves of an OTFT irradiated up to 160 Gy from figure 3.4. The black lines indicate places of constant gate bias where the drain current was extracted and plotted in the other three frames. At -49 V (part b), the current decreases as a function of dose. Part c) plots the current at a constant bias of -30 V. Initially the current increases before leveling off. Part d) shows the current at a bias of 0 V where the current is very noisy.

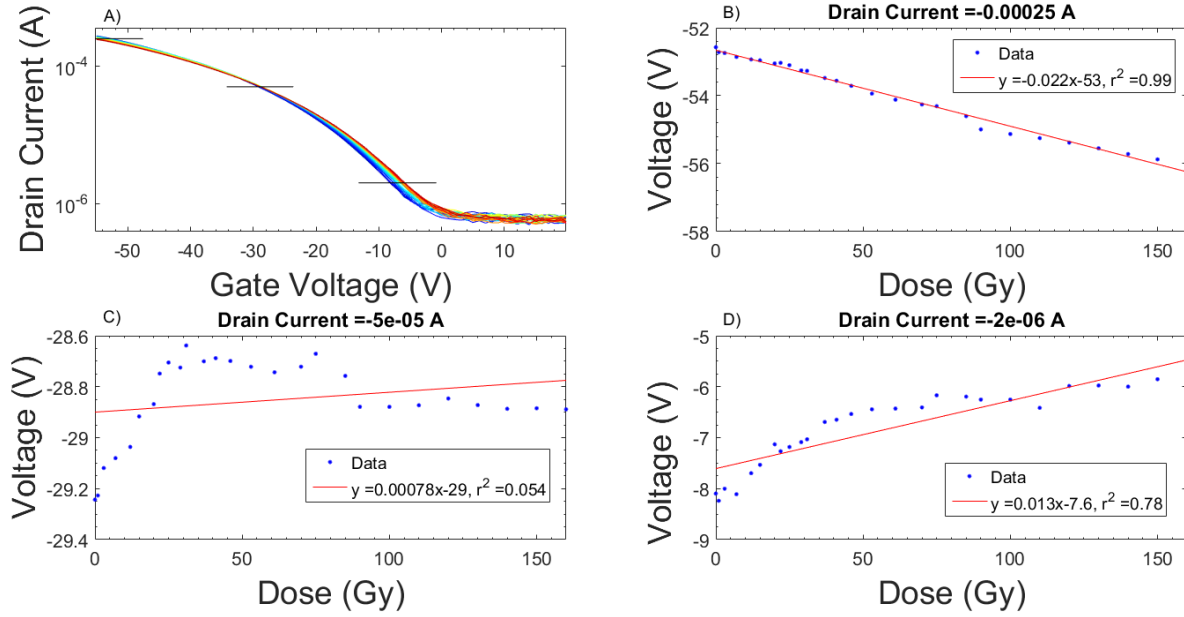


Figure 3.8: Transfer curves of the OTFT shown in figure 3.4 are shown in part a) with black lines indicating points of constant current where the gate bias is extracted for each curve. Part b) shows how the gate bias changes as a function of dose for a constant drain current of 0.25 mA. The bias decreases as a function of dose and is approximately linear across the dose range. The two bottom panels (c and d) show the change in bias at 50 and 2 μ A. In each case the bias changes by less and is much less linear than at 2.5 mA. This suggests if one measurement is to be calibrated to the dose, then a current in the on region of the curve should be selected.

3.5 Comparing an irradiated device to a control device for parylene-C

Next a control device was measured to determine if the response of the device was due to irradiation or possibly something else. The control device had the same setup as the irradiated device. A +10 V bias was applied to the control device for a length of time similar to an increment of dose given to the irradiated device. Then a transfer curve was measured and the threshold voltage extracted. The threshold shift as a function of the number of times measured (cycle number) is shown in figure 3.9 for the irradiated and non-irradiated devices. Over the measurements taken the threshold voltage shifts 70 and 100 mV/cycle for the control and irradiated devices, respectively. Even though the irradiated device shifts more than the control, the amount the control device shifts is very concerning. Ismail and Hill previously measured the transfer curve of an OTFT with a parylene-C dielectric 100 times and found that the threshold voltage was not

stable [67]. As a result of our measurements which supported the previous study, we elected to change the dielectric to see if we could improve threshold voltage stability and reduce the dependence of threshold voltage shifts on things unrelated to the ionizing irradiation.

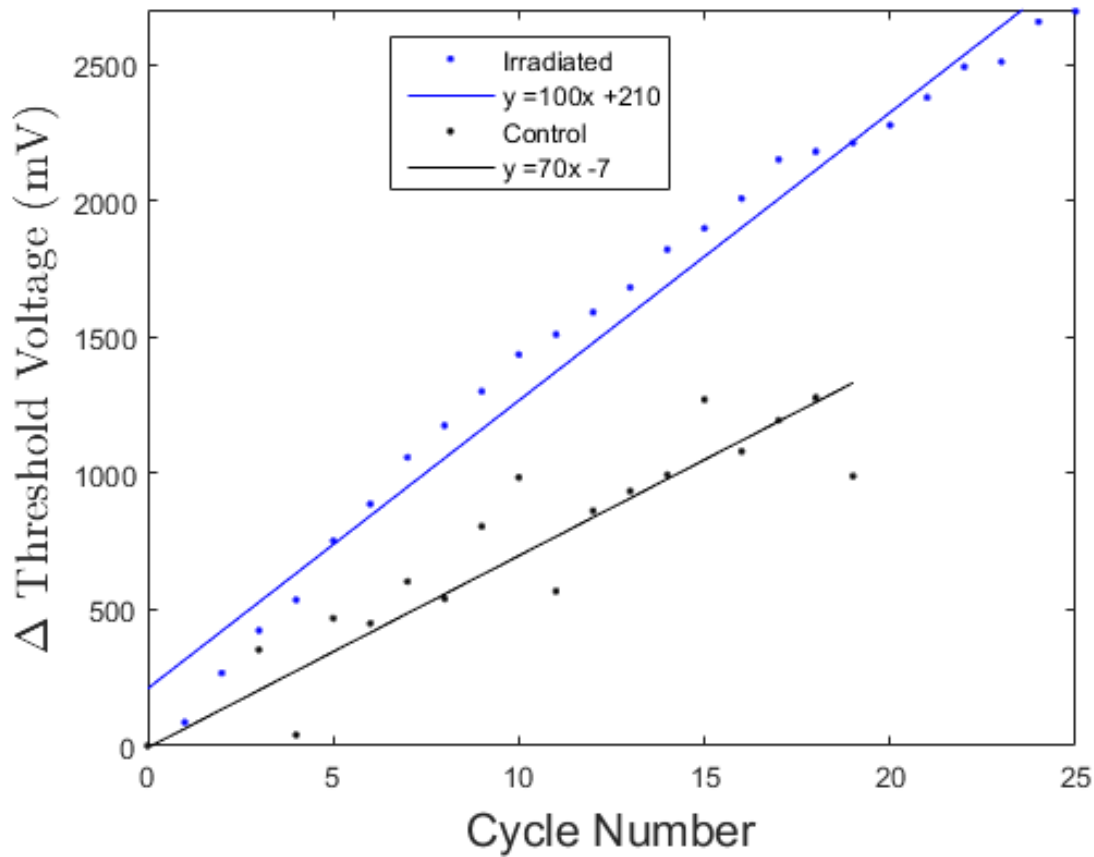


Figure 3.9: The threshold voltage shift as a function of the number of times the device was measured is shown for an irradiated OTFT and a control that was not irradiated. The slope of the irradiated OTFT was 100 mV/measurement and for the control was 70 mV/measurement. The magnitude of the change in threshold voltage of the control device was concerning and led to changing the dielectric from parylene-C used in this experiment to PMMA.

3.6 Changing to a PMMA dielectric

PMMA and CYTOP were investigated as alternative dielectrics to determine if OTFTs would have a more stable threshold voltage. No functioning transistors were made with

CYTOP in the first few batches. In the interest of time no further experiments used CYTOP. PMMA was used for the rest of the devices in this study. Figure 3.10 shows 50 transfer curves of an OTFT with a PMMA dielectric. The off current increases with repeated measurements, but the rest of the curve is more stable than the parylene-C devices. Furthermore, in figure 3.11 the threshold voltage is plotted for the 50 measurements and the shift is less than 200 mV over 50 measurements. The shift in threshold voltage for this device is more stable and so a PMMA dielectric was used for the rest of the measurements in this study.

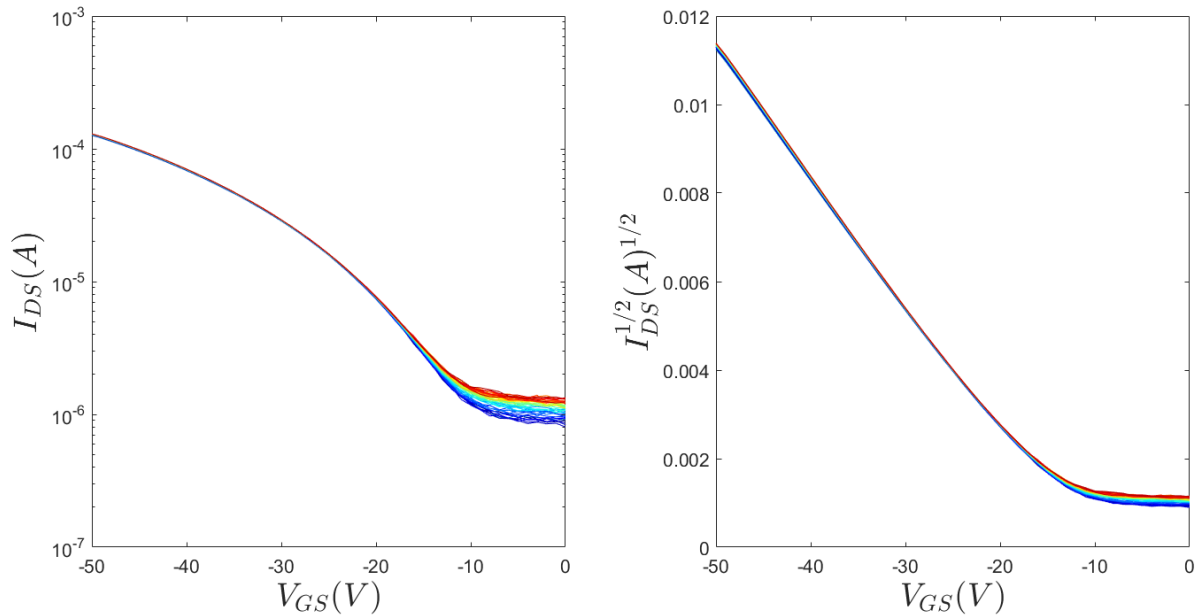


Figure 3.10: A family of 50 transfer curves of the first OTFT made with a PMMA dielectric layer. The off current increases with measurement, but the rest of the curve is more constant than the parylene-C OTFT.

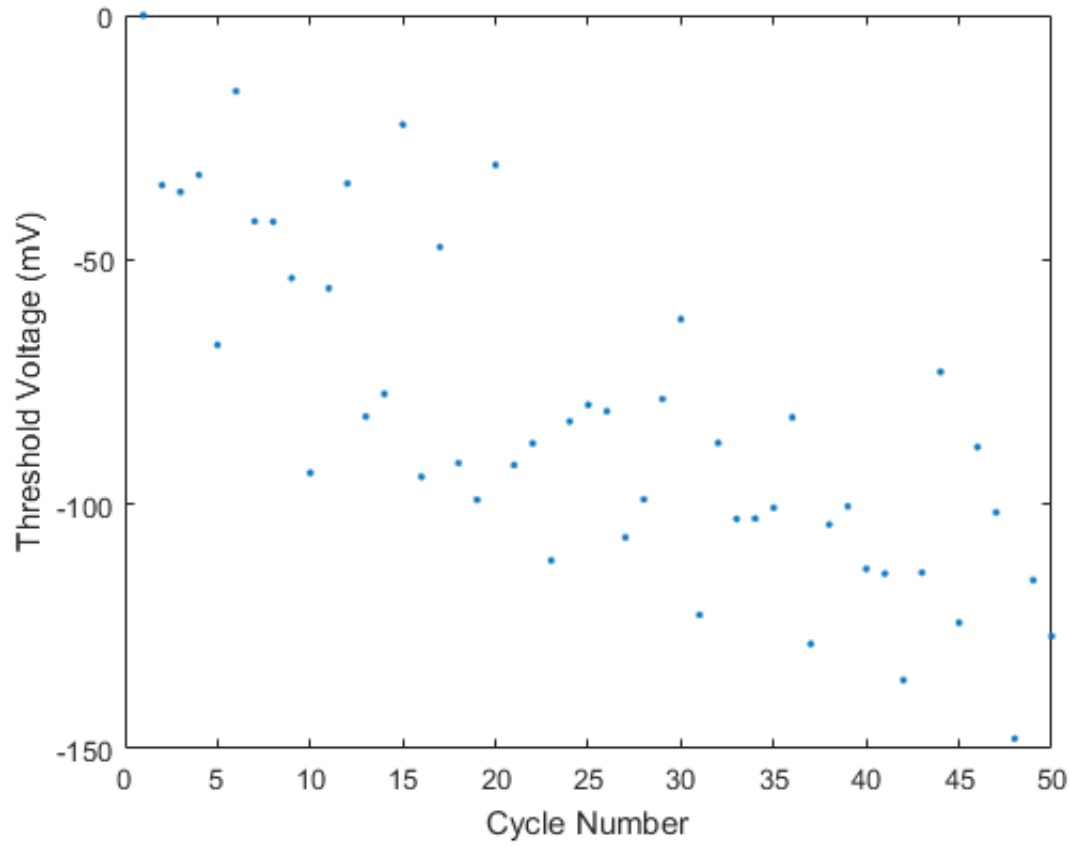


Figure 3.11: The threshold voltage for 50 measurements of the PMMA OTFT which shows more stability than the parylene-C OTFT. The threshold voltage shifts by less than 150 mV over the course of 50 measurements.

3.7 Irradiated PMMA OTFT

An OTFT was irradiated to 200 Gy with a 180 kVp photon beam, +10 V bias during irradiation, and the transfer curve measured after every 10 Gy (figure 3.12). The on current decreased with dose, whereas the off current followed no discernable trend with dose. The corresponding threshold voltage shift as a function of accumulated dose is shown in figure 3.13. The shift in threshold voltage is noisy which is possibly due to the high off-current. The noisy and high off current was concerning and so steps were taken to improve device performance before more irradiation experiments took place.

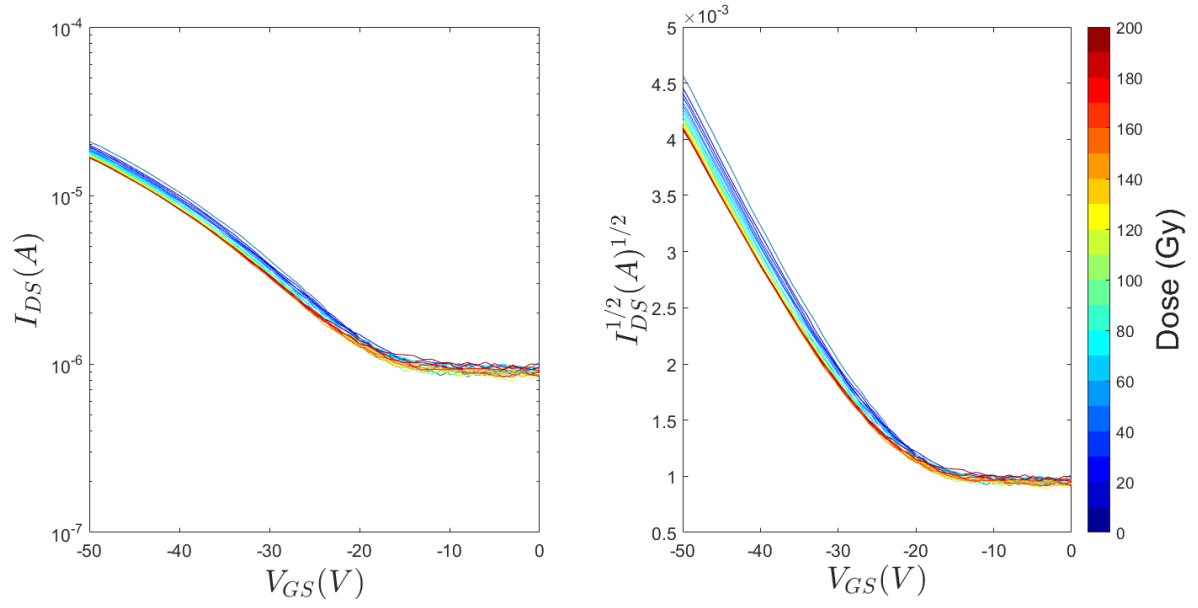


Figure 3.12: Transfer curves of the first OTFT with a PMMA dielectric irradiated. The OTFT was irradiated in 10 Gy increments to a total dose of 200 Gy.

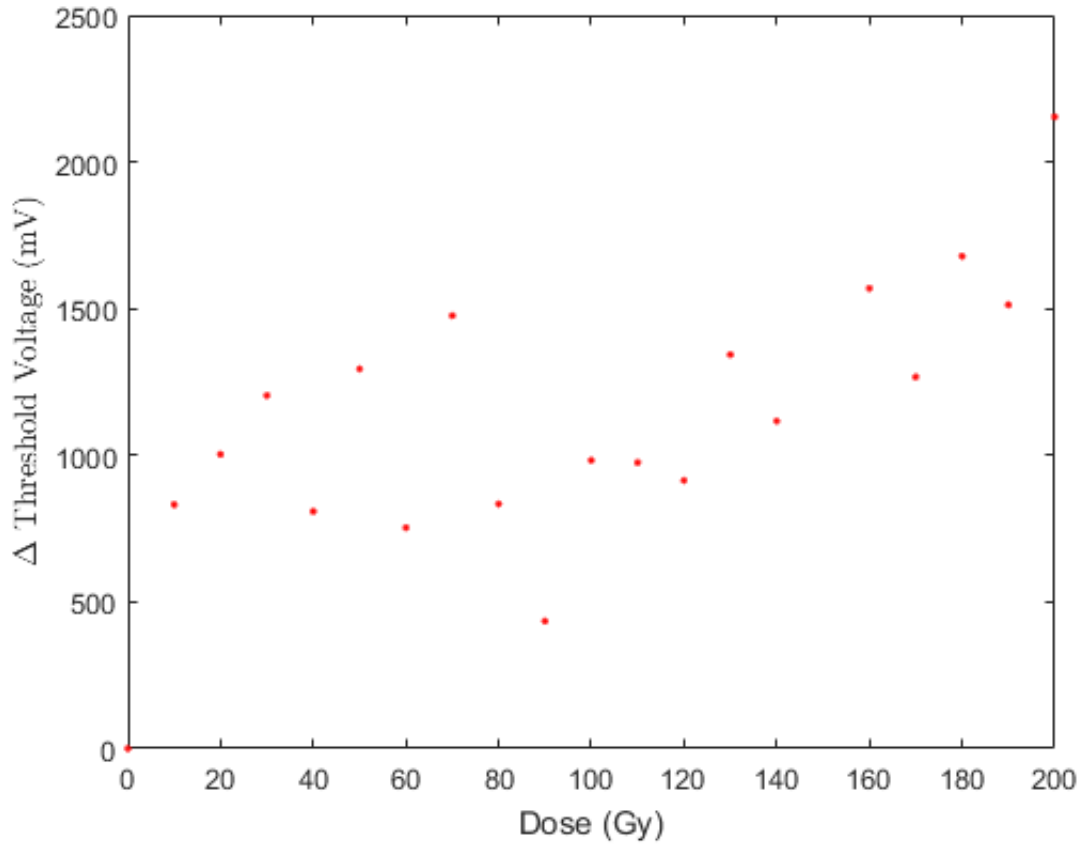


Figure 3.13: The threshold voltage shift of the first OTFT irradiated with a PMMA dielectric. The OTFT was irradiated with a 180 kVp photon beam in 10 Gy increments.

3.8 Improving OTFT Performance with a PMMA dielectric

OTFTs measured in the lab setting (all figures up to 3.4) had a much lower off-currents than OTFTs measured in the clinical irradiation setup, indicating that there could be technical challenges in the latter measurements that could be addressed to improve the quality of our measured data. In the lab the OTFTs are measured using a probe station. The probe station allows very precise contact to each electrode by lowering a tungsten needle with a micropositioner. Contact in the clinical setting was made by attaching copper tape to the electrodes and then attaching alligator clips to the tape. In the clinical setting, we switched from using single-conductor test leads with alligator clips on them to triaxial cables with alligator clips to reduce the noise. Next, the transfer curve acquisition parameters selected in the software were changed resulting in much

better measurements at low currents. The first parameter changed was the window of currents that the Keithley expected to measure. As the current got to the lower part of the window ($\sim 10^{-6}$ A) the current would be very noisy and currents below this value were not able to be measured. The window was switched to an automatic mode where the window adjusts based on the current that it is currently reading. The automatic window was not used initially because it caused a noisy signal across the entire data acquisition. However, this time the number of power line cycles (NPLC) was increased. Increasing NPLC increases the noise integration time, which increases the accuracy. The down side of increasing NPLC is slower data acquisition, but the combination of the new measurement parameters allowed for measurements at lower currents with less noise. Shown in figure 3.14 are 50 transfer curves of an OTFT with the new parameters. Particularly if you compare the transfer curves previously (figure 3.12) the off current is about 3×10^{-7} A in comparison to 1×10^{-6} A and there is much less noise. However, this off current is still higher than the $(4.0 \pm 3.3) \times 10^{-9}$ A measured for 300 nm parylene-C dielectric devices measured previously in the lab. To further lower the off current the spin coating speed was lowered from 2000 rpm to 1000 rpm when forming the PMMA dielectric layer. Lowering the spin speed would create a thicker dielectric which could isolate the gate better and reduce leakage current. Furthermore, instead of attaching the copper tape leads before spin coating the PMMA they were not attached until directly before the encapsulation step. This was done by rubbing off the PMMA covering the contact with a Q-tip soaked in toluene. Care needed to be taken when removing the PMMA because if too much was rubbed off the gate contact would touch the semiconductor directly and the OTFT would not work. If not enough PMMA was removed then contact would not be made.

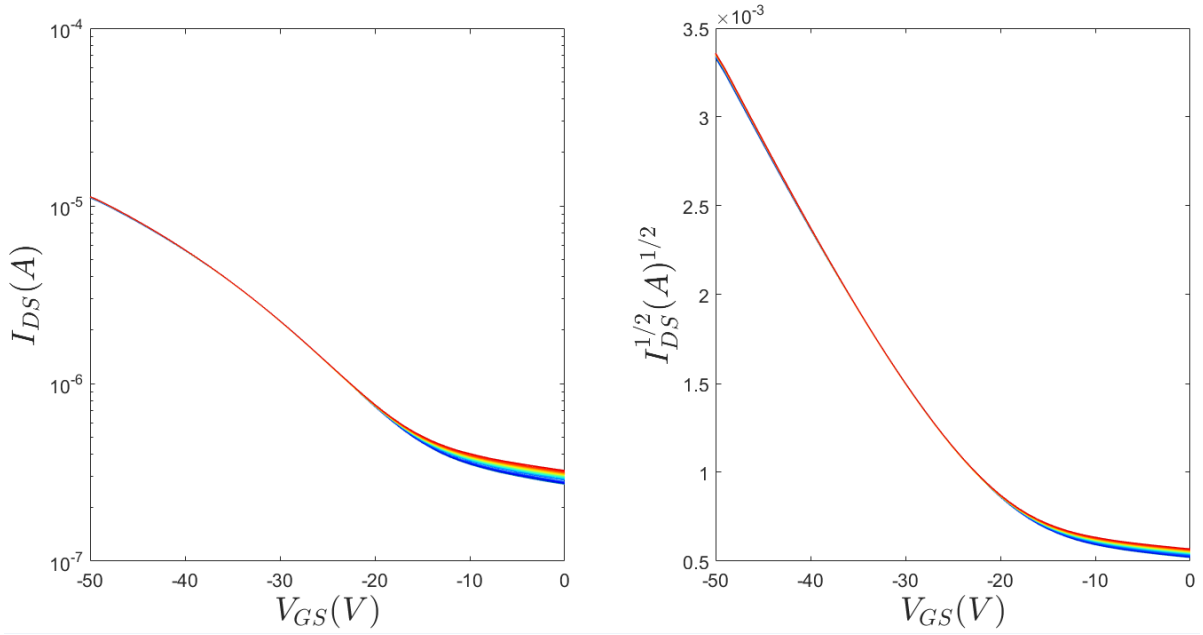


Figure 3.14: An OTFT made with a PMMA dielectric measured in the irradiation setup, but was not irradiated. The acquisition parameters were improved reducing the noise in the off current and so the transfer curves are smooth. This plot highlights the true off current of the OTFTs, which is much higher than it was for the parylene-C OTFTs.

3.9 Effects of Encapsulation and Copper Tape Contacts

With improved OTFTs an experiment was performed to investigate if the copper tape contacts or encapsulation layer affected the device performance. Figure 3.15 shows the transfer curves of OTFTs when measured first with a probe station (no copper tape contacts needed), then after adding the copper tape contacts, and then again after encapsulating the device (same devices at different stages of fabrication). No clear pattern emerged. Shown in figure 3.16 are two examples where one device (left) has the lowest off current before adding the copper tape and encapsulating the device and the second (right) has the lowest off current afterward. Since some devices after the application of copper tape and encapsulation layers had low off current, this method was deemed acceptable. However, OTFTs would not be used for irradiation if the off current was higher than 1×10^{-7} A.

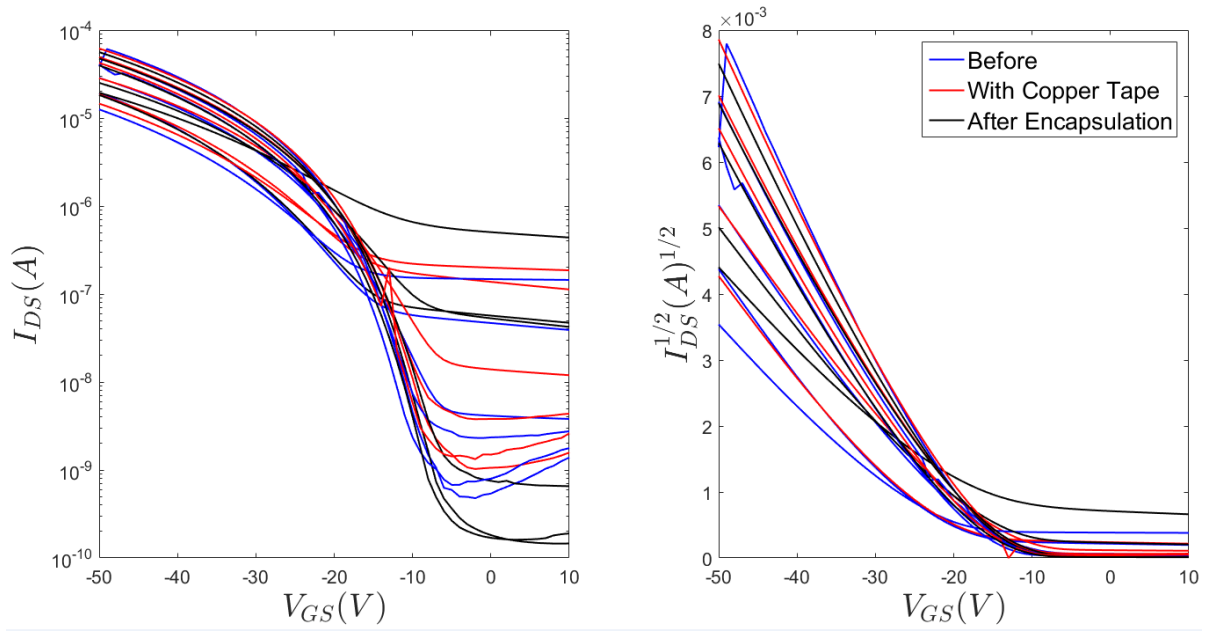


Figure 3.15: Transfer curves taken before (no copper tape or encapsulation layer), after copper tape connected to the electrical contacts, and then after the entire device was encapsulated with approximately $1 \mu\text{m}$ of parylene-C. Device performance changed with the addition of copper tape and encapsulation, but no systematic affect was observed. Some of the devices performed better and some performed worse with each step.

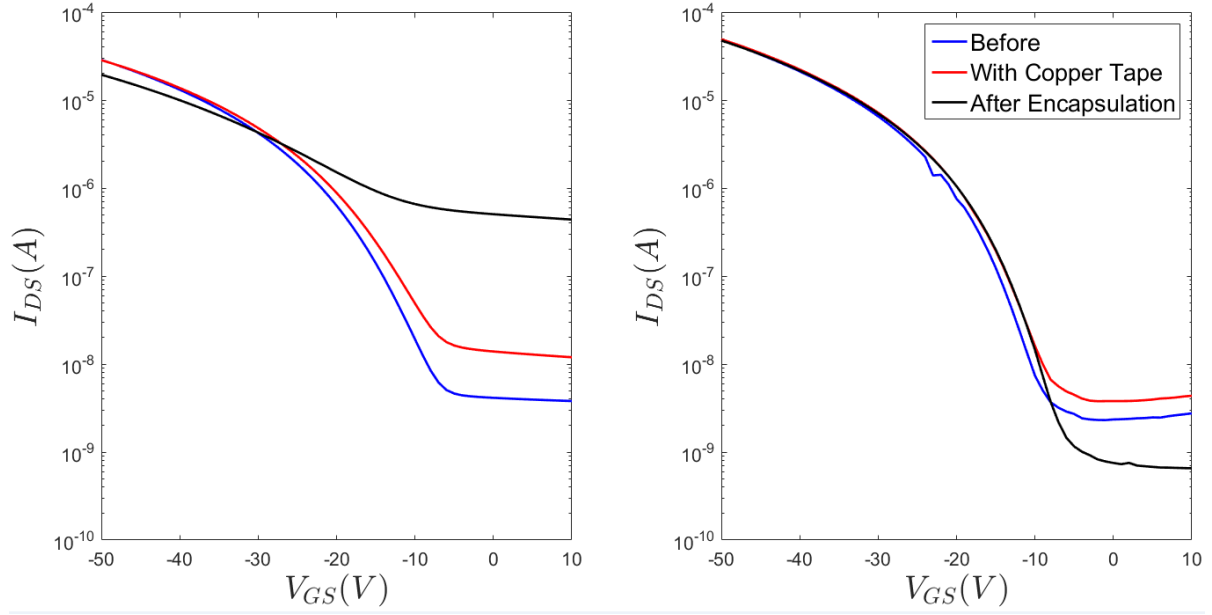


Figure 3.16: The plot on the left shows an OTFT that had worse performance when encapsulated. On the right is an example of an OTFT that had improved off current with encapsulation. Going forward OTFTs were contacted using the copper tape and the devices encapsulated with parylene-C.

3.10 Irradiation Response of OTFTs with PMMA Dielectric

The response of an OTFT was measured in photon beams of 100 kV, 180 kV, 6 MV, and 18 MV (different device for each energy). Each OTFT was irradiated to an accumulated dose of 400 Gy and the transfer curves were measured after 10 and 20 Gy for the kilovoltage and megavoltage irradiated OTFTs, respectively. Figure 3.17 shows the threshold voltage shift as a function of accumulated dose for each energy. In each case the threshold voltage shift is positive. Furthermore, the amount of threshold voltage shift appears to decrease with accumulated dose. This can be seen in figure 3.18 where the sensitivity of the devices are plotted as a function of accumulated dose. The sensitivity was determined by calculating the slope of the threshold voltage as a function of accumulated dose at each point. Over the first 100 Gy the sensitivity of the devices differ greatly with the initial sensitivity of the megavoltage beams being below 2 mV/Gy and the initial sensitivity of the kilovoltage devices being greater than 5 mV/Gy. After about 100 Gy the sensitivities of the devices begin to converge toward a value of 0.5 mV/Gy. In figure 3.19 the normalized mobility is shown as a function of accumulated

dose for each OTFT. The mobilities are normalized to the mobility measured directly before irradiating the OTFTs. In each case the mobility decreases with accumulated dose with larger degradations occurring for kilovoltage irradiated OTFTs in comparison to megavoltage irradiated OTFTs. Each OTFT remained functional after 400 Gy with the largest degradation of mobility being about 15% for the OTFT irradiated with 100 kV.

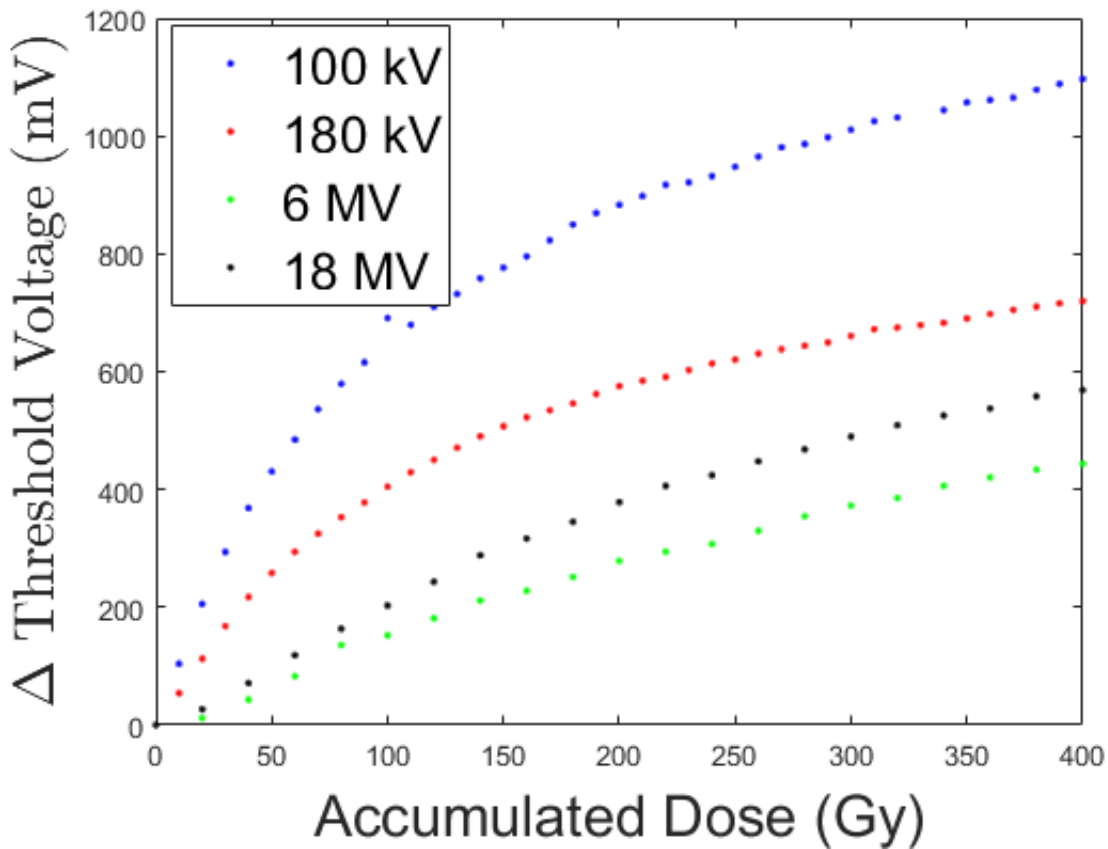


Figure 3.17: The change in threshold voltage as a function of accumulated dose for each energy used. A different OTFT was used for each experiment and so the different responses could partially be due to differences in the devices. In each case there is a positive shift with accumulated dose.

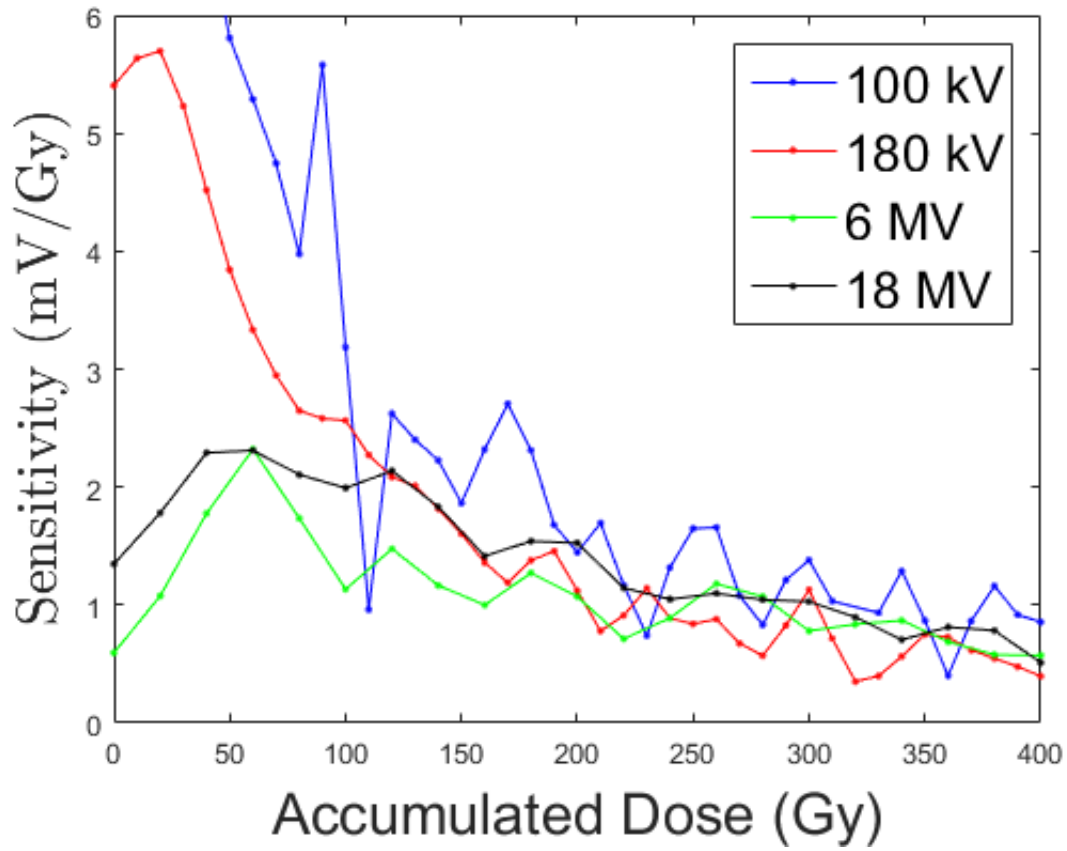


Figure 3.18: The sensitivity (change in threshold voltage with dose) is plotted as a function of accumulated dose for each of the four photon beams used in this study. Initially there are large deviations between devices in sensitivity, but after about 100 Gy of accumulated dose the sensitivities begin to converge.

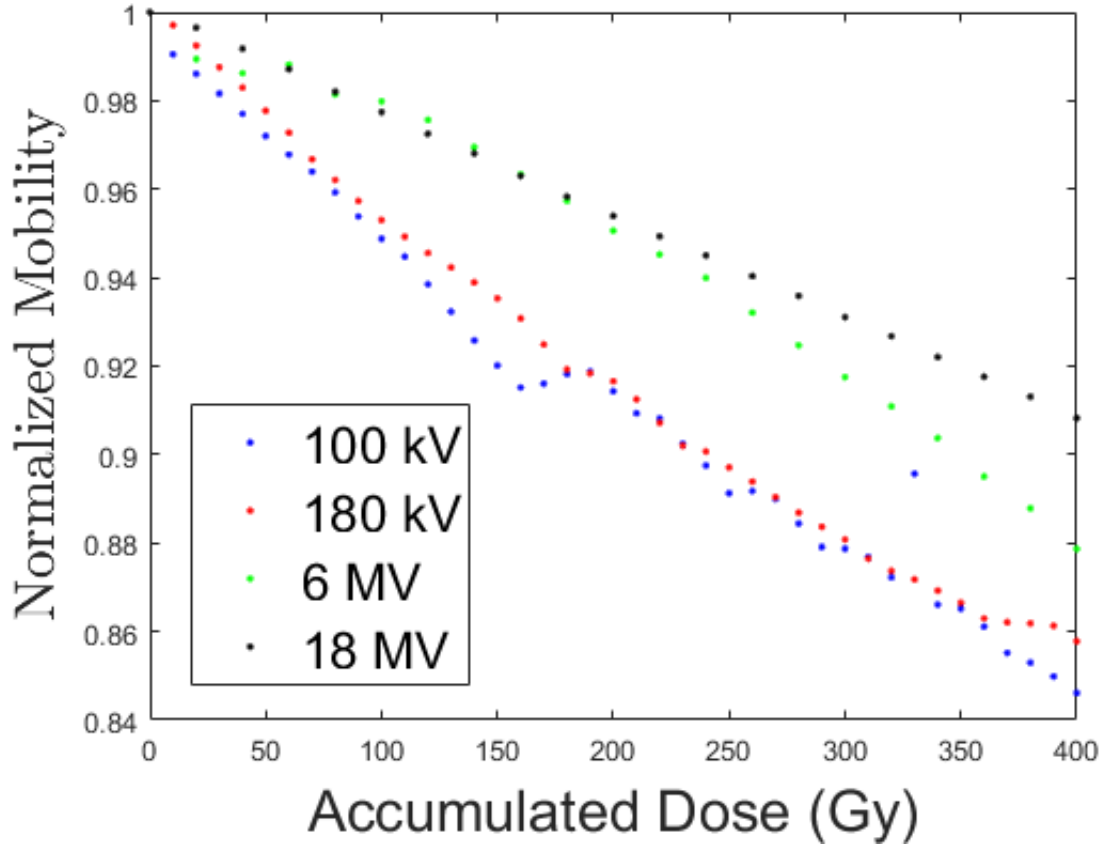


Figure 3.19: The normalized mobility of an OTFT with accumulated dose for each of the photon beams used in this study. The mobility was normalized to the mobility before irradiating for each OTFT. Each device shows degradation in the mobility with accumulated dose with a maximum reduction of about 15% for the OTFT irradiated with 100 kV photon beam.

3.10.1 OTFT Lifetime

An OTFT was irradiated up to 1000 Gy using a 6 MV photon beam and the transfer curve measured after every 20 Gy. The resulting threshold voltage shift as a function of time is shown in figure 3.20. After 1000 Gy the OTFT is still functional and the threshold voltage continues to change with accumulated dose. The threshold voltage after 300 Gy has a sensitivity of 0.8 ± 0.1 mV/Gy. Before and after the device was irradiated the device was measured 5 times with a +10 V bias held for the length of an increment of irradiation as a control. The threshold voltage shift with no irradiation is in the opposite direction in comparison to the shift during irradiations indicating that

we are measuring a radiation-induced response.

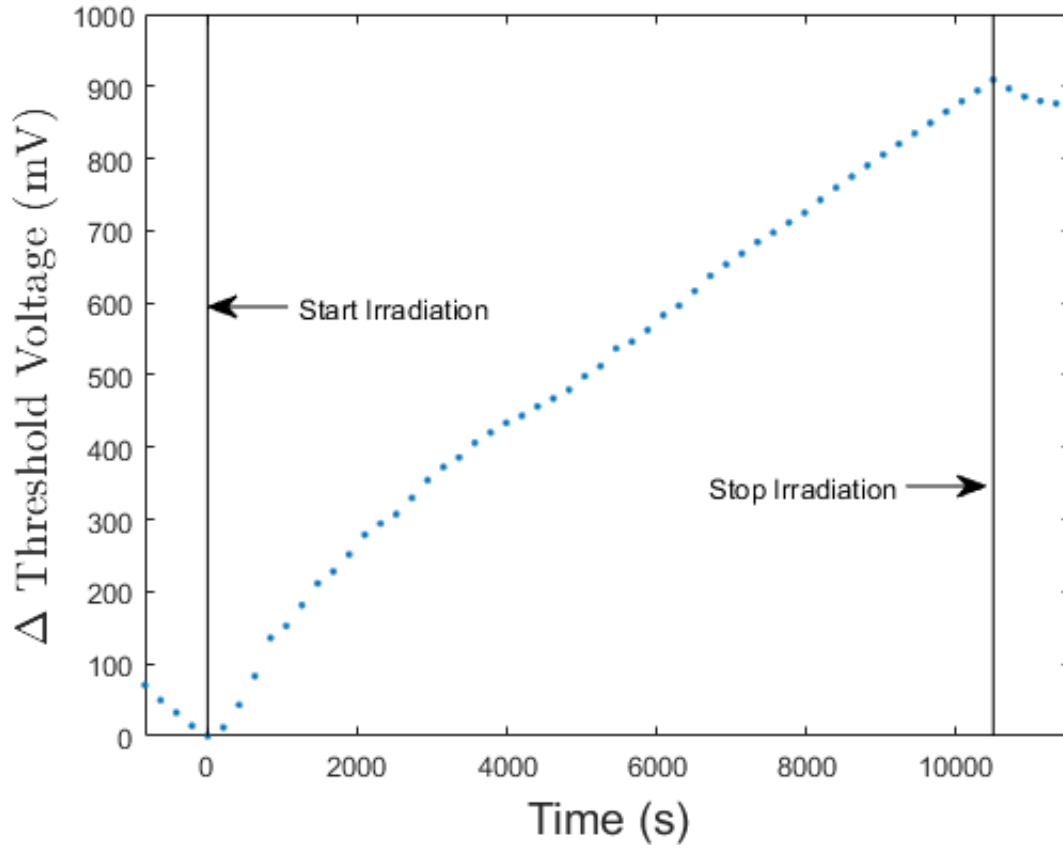


Figure 3.20: The change in threshold voltage as a function of time for an OTFT irradiated up to 1000 Gy with a 6 MV photon beam. Before and after irradiating the device a shift in threshold voltage was observed in the opposite direction to that of during irradiation.

3.10.2 Directional Dependence

To measure directional dependence an OTFT was placed at isocenter and irradiated with an 18 MV photon beam at incidence angles of 0° , 90° , and 180° . At each angle, the OTFT was irradiated up to 100 Gy in five increments with the transfer curve measured after each increment. The sensitivity as a function of accumulated dose is shown in figure 3.21. Similarly to before (figure 3.18) the sensitivity starts high (~ 4 mV/Gy) and decreases with accumulated dose. Qualitatively the sensitivity looks similar to previous OTFTs, but more experiments are needed to determine the true directional dependence.

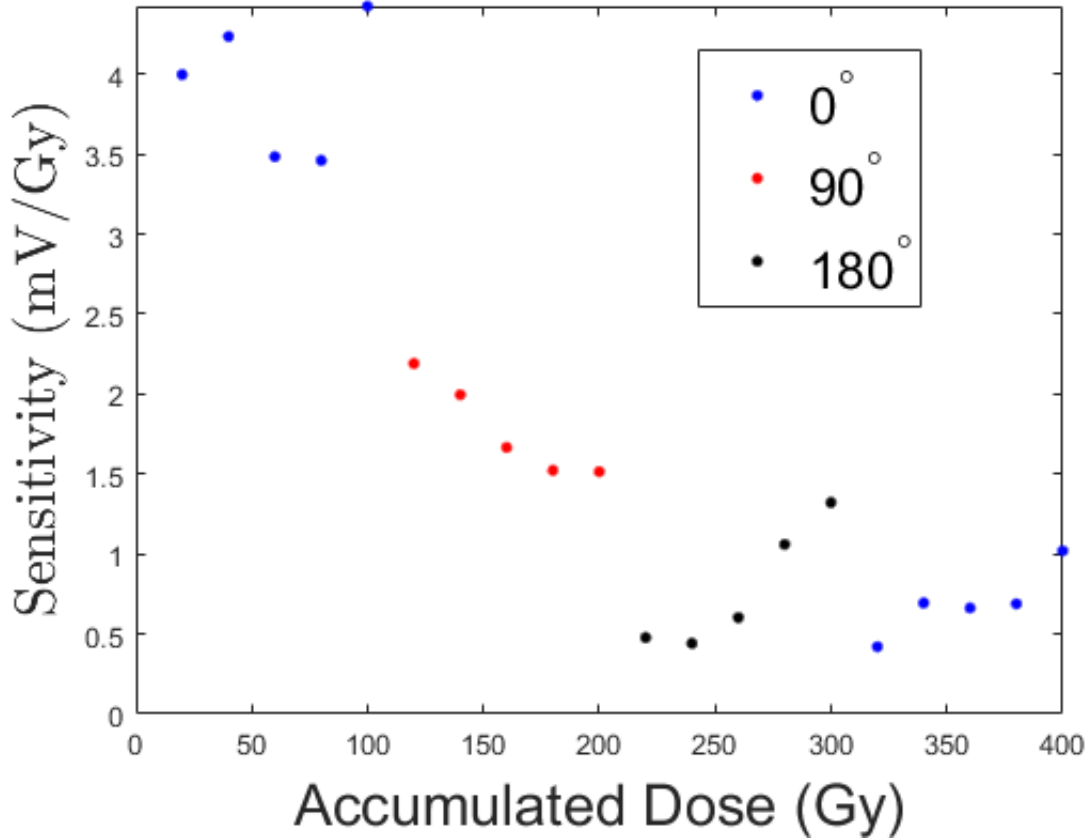


Figure 3.21: An OTFT was placed at the isocenter of an 18 MV photon beam and irradiated at incidence angles of 0° , 90° , and 180° . The sensitivity (change in threshold voltage with dose) follows the trend of devices irradiated previously where all irradiations were done at 0° . From these plots we cannot determine the directional dependence at this time because the sensitivity degradation with dose is too variable even with devices at a constant angle.

3.10.3 Dose Rate Dependence

To measure the dose rate dependence an OTFT was irradiated with an 18 MV photon beam at various SSDs. The starting SSD was 95 cm and increased in 5 cm increments after every 4 irradiations of 15 Gy each (60 Gy at each SSD). The sensitivity as a function of dose is shown in figure 3.22. As with previous devices the sensitivity start high (~ 5 mV/Gy) and decreases with accumulated dose. As with the directional dependence measurements, qualitatively the plot looks similar to previously irradiated OTFTs, but more experiments are needed to truly quantify the dose rate.

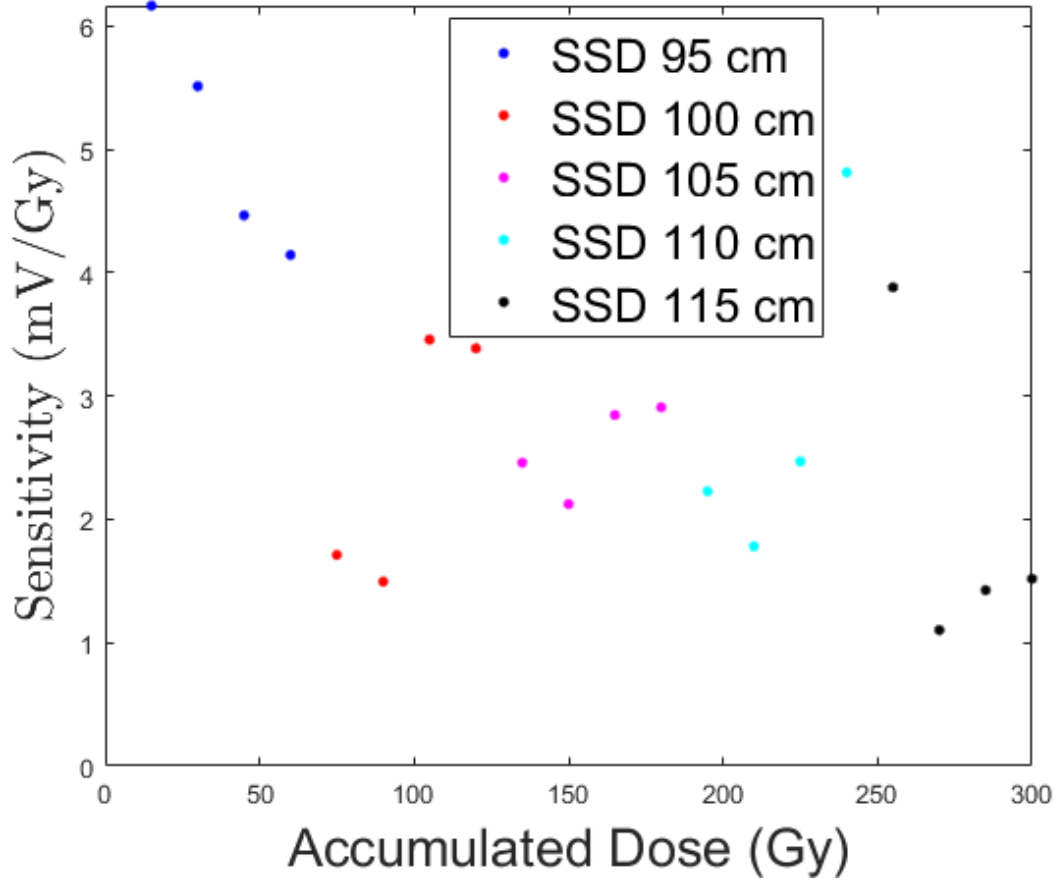


Figure 3.22: An OTFT irradiated with an 18 MV photon beam in 15 Gy increments. The sensitivity (change in threshold voltage with dose) is plotted as a function of accumulated dose. The SSD is increased with accumulated dose, while the MU's are increased, such that the dose delivered to the OTFT is the same at each SSD, but the dose rate decreases. From these plots we cannot determine the dose rate dependence at this time because the sensitivity degradation with dose is too variable even with devices at a constant dose rate.

3.11 Monte Carlo Simulations

3.11.1 Simplistic Design

In Monte Carlo a layered design OTFT as depicted in figure 3.23 was simulated and irradiated with photon beam energies ranging from 20 keV to 100 keV. The perturbation factor at each energy was calculated and normalized to the perturbation factor at 100 keV. The thickness and position of the parylene-C layers were varied to see how

the composition and geometry affected the perturbation factor. Figure 3.24 shows the perturbation factor when the thickness of parylene-C is varied for the inside layers (top coat 2 and substrate 2) as a function of energy. The description in section 2.6 generalized the simulation to 3 top coat layers and 3 substrate layers. However, in this simulation only 2 top coats and 2 substrates were used (always symmetric). As the thickness of parylene-C is decreased the perturbation factor is closer to unity. Figure 3.25 shows the perturbation factor for various thicknesses of parylene-C as the outside layers (top coat 1 and substrate 1). If parylene-C is present the perturbation factor is farther from unity at low energies. However, increasing the thickness of parylene-C does not appear to make the perturbation factor worse. Both of these results suggest that for this particular configuration parylene-C should not be used to optimize the OTFT for energy dependence. Furthermore, in comparing the two plots it is evident that the proximity of the parylene-C to the dielectric affects the perturbation factor. Perturbation factors are further from unity when the parylene-C layer is closer to the dielectric.

Top Coat 1 (100 μm Parylene-F)	Top Coat 1 (Variable Parylene-C)
Top Coat 2 (Variable Parylene-C)	Top Coat 2 (100 μm Parylene-F)
Semiconductor (50 nm Pentacene)	Semiconductor (50 nm Pentacene)
Dielectric (1 μm Parylene-F)	Dielectric (1 μm Parylene-F)
Gate (50 nm Aluminum)	Gate (50 nm Aluminum)
Substrate 2 (Variable Parylene-C)	Substrate 2 (100 μm Parylene-F)
Substrate 1 (100 μm Parylene-F)	Substrate 1 (Variable Parylene-C)

Figure 3.23: On the left is a schematic of a simplistic OTFT with the parylene-C on the inside and on the right parylene-C is on the outside. The dose is scored to the parylene-F dielectric layer in the middle.

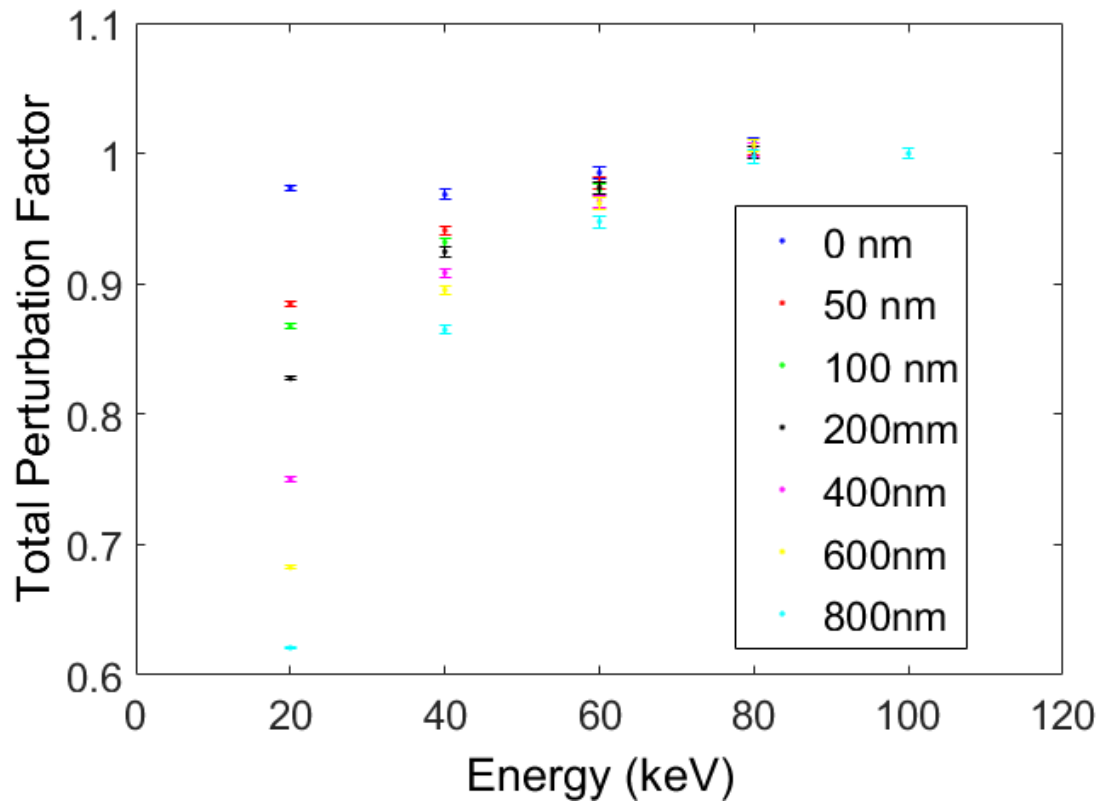


Figure 3.24: Perturbation factor as a function of energy for the varying thickness of parylene-C as the inside layers (figure 3.24) of the OTFT. As the energy decreases the perturbation factors goes farther from unity. As the thickness of parylene-C increases the perturbation factor goes farther from unity.

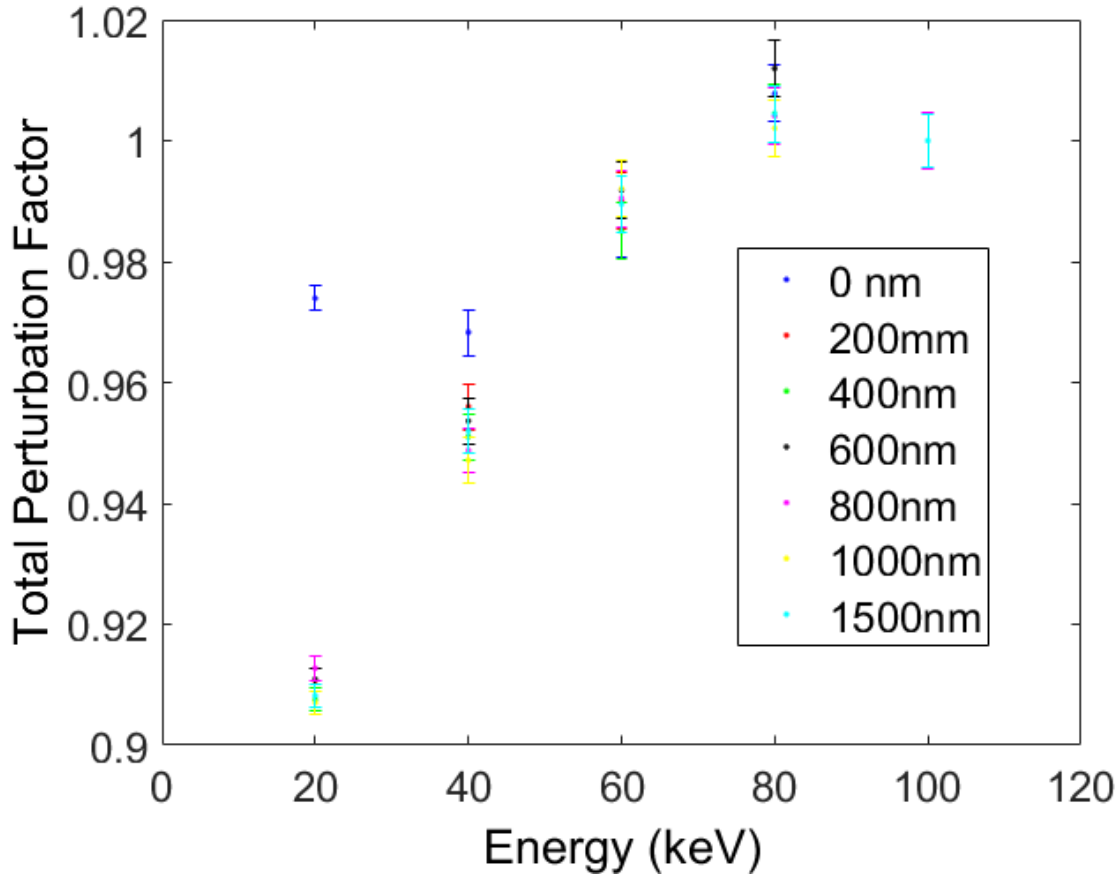


Figure 3.25: Perturbation factor as a function of energy for the varying thickness of parylene-C as the outside layers (figure 3.24) of the OTFT. If parylene-C is present the perturbation factor is farther from unity at low energies. However, the thickness of the parylene-C does not have a large effect.

The previous figures (3.24 and 3.25) suggest that parylene-F is a good material to use in fabricating OTFTs with low energy dependence. From that we simulated a device shown in figure 3.26 with parylene-F on a PET substrate. Immediately we noticed an energy dependence at low energies and decided to add PMMA layers to try to obtain a perturbation factor closer to unity. The perturbation as a function of energy for various thicknesses of PMMA are shown in figures 3.27 and 3.28. At low energies the perturbation factors get closer to unity with increasing thickness until a thickness of ~ 1500 nm where the perturbation factor is greater than unity and continues to increase with thickness.

Top Coat 1 (100 μm PET)
Top Coat 2 (100 μm Parylene-F)
Top Coat 3 (variable PMMA)
Semiconductor (50 nm Pentacene)
Dielectric (1 μm Parylene-F)
Gate (50 nm Aluminum)
Substrate 1 (variable PMMA)
Substrate 2 (100 μm Parylene-F)
Substrate 3 (100 μm PET)

Figure 3.26: Schematic of simulated OTFT where the thickness of the PMMA layers were variable, but both layers had the same thickness. The dose was scored in the dielectric layer.

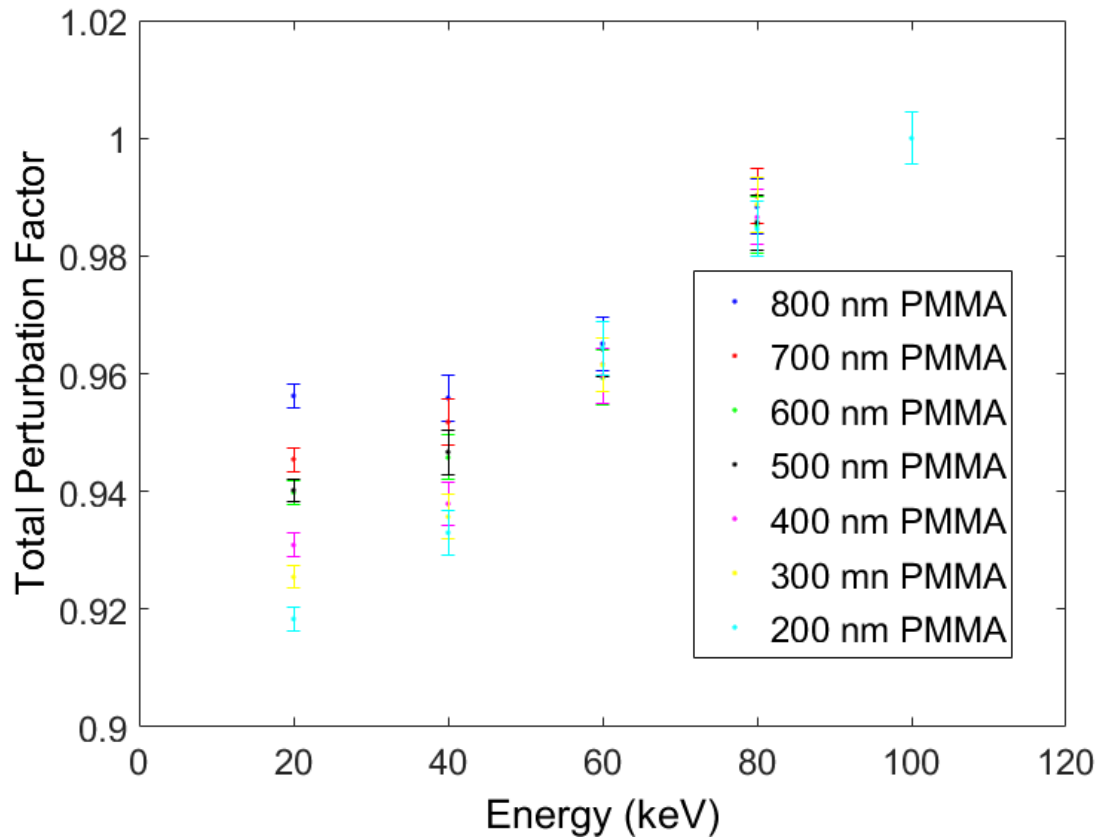


Figure 3.27: Perturbation factor for the OTFT in figure 3.26 normalized to 100 keV. This plot shows the perturbation factor can be made small with PET substrate allowing for greater mechanical stability. As the thickness of PMMA increased the perturbation factor became closer to unity. By changing the thickness of the surrounding materials the dose to the dielectric can be optimized to reduce the energy dependence.

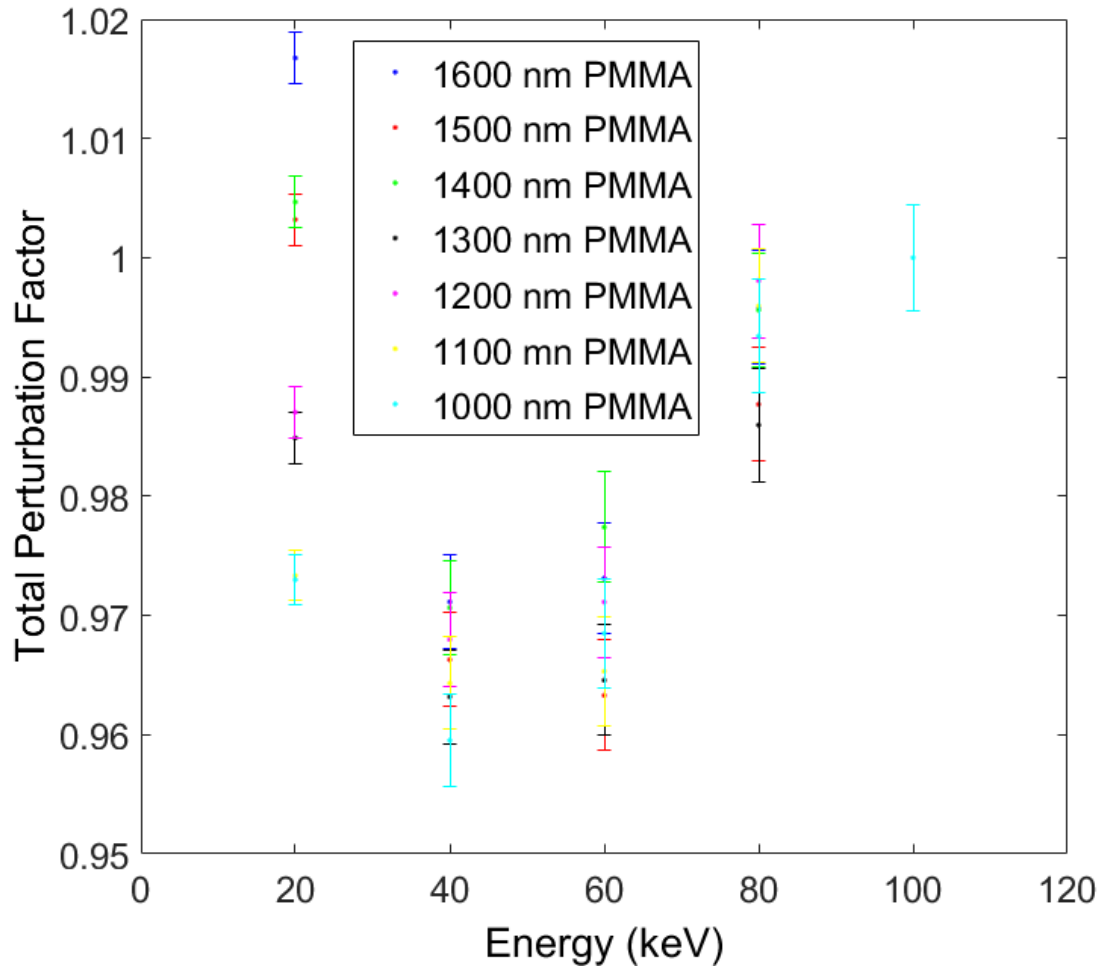


Figure 3.28: Perturbation factor for the OTFT in figure 3.27 normalized to 100 keV. At low energies the perturbation factor increases with PMMA thickness, with an optimal thickness at 20 keV being ~ 1500 nm. By optimizing the thickness of the PMMA the perturbation factor was within 3% of unity across the energy range.

3.11.2 Directional Dependence

The OTFT used experimentally and shown in figure 2.4 was simulated and irradiated at photon energies of Co-60, 6 MV, 10 MV, and 15 MV and incident angles of 0° , 90° , and 180° . Over this energy range the perturbation factors were less than 6% from unity at each angle (figure 3.29). From the simulations, the directional dependence is small. The perturbation factors farthest from unity are at 180° where the photon beam passes through 1.1 mm of glass before the active volume. If the glass is removed perhaps the directional dependence would be less. The error in the measurements are large making

it difficult to differentiate one measurement from another. More particles should be simulated to lower the error.

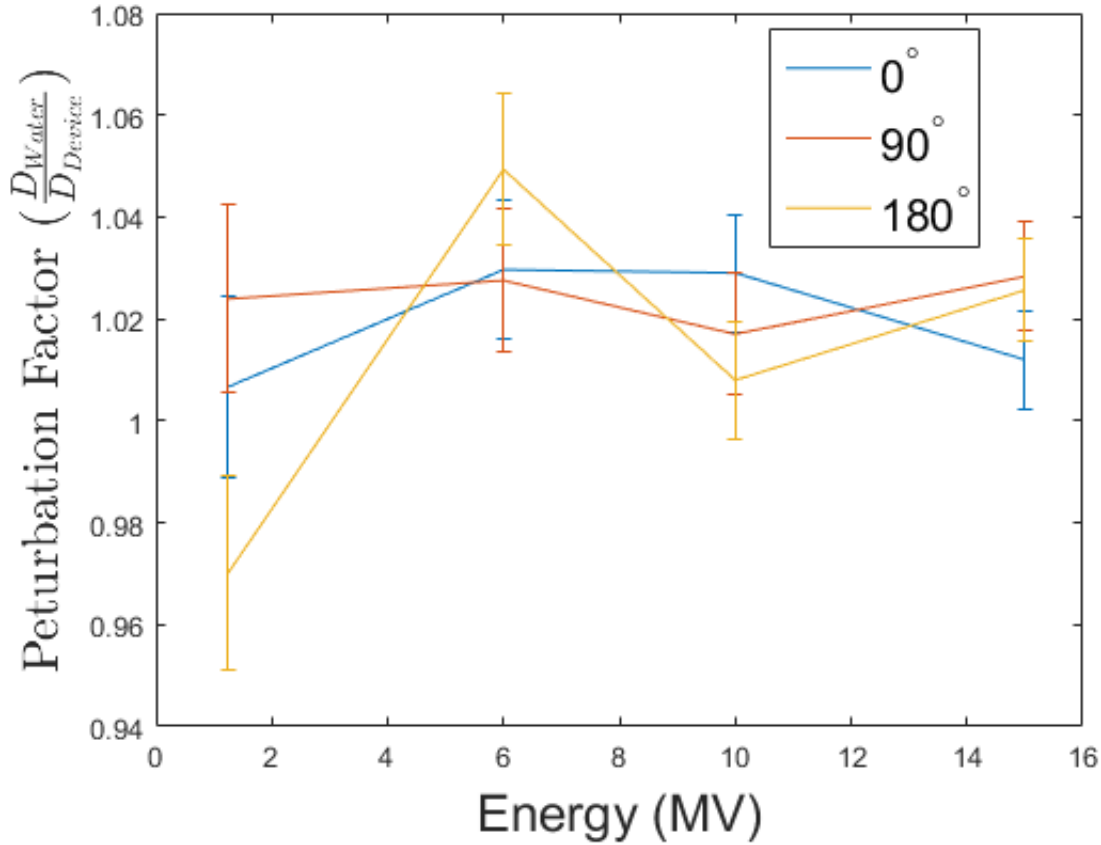


Figure 3.29: The perturbation factors simulated for the realistic OTFT shown in figure 2.4 for beam energies of Co-60, 6 MV, 10 MV, and 18 MV and beam incident angles of 0°, 90°, and 180°.

Presented first in this section were the changes in fabrication that led to improvements of OTFTs performance. Next, the response of OTFTs to photon fields of various qualities were given in terms of the threshold voltage shift and degradation of mobility. Lastly, Monte Carlo results showed the potential to make devices with low energy dependence. In the following section a more complete discussion of how the changes in fabrication lead to better OTFTs, the significance of the response of the OTFTs in comparison to MOSFETs, and the significance of the different response to various energy photon beams will be discussed.

Chapter 4

Discussion

Over the course of the project a new OTFT design was fabricated on a flexible substrate. Many challenges arose, but through better cleaning methods, better acquisition setup, and different electrode connections the OTFTs were greatly improved. We have demonstrated that an OTFT on a flexible substrate shows a measureable response to photon radiation of various qualities. Furthermore, we have demonstrated that an OTFT can remain functional after 1000 Gy and important characteristics (mobility and threshold voltage) continue to change with dose. Some remaining challenges include making more reproducible OTFTs, increasing the sensitivity, and accurately measuring the dose rate, energy, and directional dependences.

4.1 Improving OTFT function

Slowing the spin speed of the dielectric PMMA improved the off current of the OTFTs. A slower spin speed creates a thicker dielectric which could isolate the gate better. The thickness of the film is proportional to the angular velocity using:

$$t \propto \frac{1}{\sqrt{\omega}} \quad (4.1)$$

where t is the thickness and ω is the angular velocity. If the high off current was due to leakage from the gate, then perhaps using a different dielectric will improve device performance.

Another modification of the device design was to attach copper leads after spin coating the PMMA. This was done by rubbing the PMMA off of the contacts with a Q-tip soaked in toluene after the PMMA was spin coated. Although the effects of this change were not investigated, it is thought that spin coating with the copper leads already attached could potentially lead to problems. The PMMA was dissolved in toluene which could have damaged the copper tape or could have spread the conductive adhesive from the tape across the device and caused shorts through the device.

As the project went on and experience was gained, the OTFTs were exposed to air less during fabrication. Exposure to air increases the chance that dust can get on the OTFT. Since many of the layers are less than a micrometer thick, dust can be thicker than a layer of the device. If dust gets on the OTFT it can cause a short through a layer and ruin the device. Furthermore, pentacene is sensitive to air, so reducing its exposure should help device performance [68]. We spent time investigating the effect of depositing a parylene-C encapsulation layer to protect the device from degradation when exposed to air because it is necessary to be exposed to air in the irradiation environment. OTFTs showed good performance after the deposition of parylene-C, which lead to encapsulating all of the devices afterwards.

4.2 Mobility Degradation with Dose

Each OTFT had a degradation of mobility with accumulated dose which is consistent with other studies using organic semiconductors [57, 58]. Kim *et al* made an OTFT with a rubrene semiconductor on a silicon-dioxide dielectric and measured a decrease in mobility of more than 50 % after 1000 Gy[58]. For our device irradiated with a 6 MV photon beam to 1000 Gy we measured a mobility reduction of about 32%. Mobility is a measure of how efficiently charge carriers can move through the conductive path [64]. The charge defects (trapped holes) at the interface exert Coulomb forces on the charge carriers as they flow through the channel scattering them from their intended path. This means that the charge carriers do not flow from the source to drain as quickly as before and the mobility is reduced [69].

4.3 Threshold Voltage Shift with Dose

For each of the devices irradiated in this study the threshold voltage shifted positively with increasing accumulated dose. This is the opposite of what is observed for p-type MOSFETs used as dosimeters [70]. Ionizing radiation produces electron-hole pairs throughout the OTFT. Electrons in the pentacene layer can become trapped at the pentacene SiO_2 interface in the hydroxyl groups at the boundary [71, 72]. This means that in devices with an organic semiconductor that the change in signal may not be dominated by the trapped charge in the dielectric layer, but by trapped charge or other

defects in the organic semiconductor itself. Kim *et al* irradiated an OTFT with a pentacene semiconductor and SiO_2 dielectric with 10 MeV protons [73]. With a proton fluence of 10^{12} cm^{-2} they measured a small positive shift in threshold voltage. However, when irradiating with a 10^{14} cm^{-2} fluence of protons they measured a negative shift in the threshold voltage. They attributed the shift at low proton fluence to the trapped electrons in the pentacene layer. The electric field produced from the trapped electrons in the pentacene was greater than the electric field from the trapped holes in the SiO_2 . Effectively this electric field acts like a negative gate voltage, which results in a positive threshold voltage shift. As the proton fluence increases more holes are trapped in SiO_2 and migrate closer to the SiO_2 /pentacene interface. The electric field from the trapped holes in the SiO_2 dominate the electric field created by the trapped electrons in the pentacene causing a negative shift in threshold voltage. To support this interpretation of their results they made an OTFT with a self-assembled monolayer (SAM) of octadecyltrichlorosilane (OTS) coating the SiO_2 dielectric layer. The OTS is used to suppresses the interface trap states at the interface and then pentacene is deposited on top [74]. When irradiating the OTFT with 10^{12} cm^{-2} fluence of protons they measured a slight negative shift in threshold voltage in contrast to the previous OTFTs. With fewer electrons being trapped at the interface the slight shift in threshold voltage was due to the trapped holes in the SiO_2 layer. In our study we have measured a positive shift in threshold voltage as a function of dose. Like Kim *et al*, we used a pentacene semiconductor, but unlike their study we used a PMMA dielectric instead of SiO_2 . At the current time there is insufficient evidence to make any conclusions, but we can speculate. Perhaps in our OTFTs the PMMA does not trap electrons or holes preferentially and the entire signal is due to defects in the pentacene semiconductor. Another possibility is that PMMA traps electrons, but to a far less degree than SiO_2 traps holes which results in the slight positive shift in the threshold voltage. It should be noted that the sensitivities in this study ($\sim 1 \text{ mV/Gy}$) are about two orders of magnitude lower than MOSFETs used as dosimeters ($\sim 100 \text{ mV/Gy}$). Part of the reason the response is small is that the mobility degradation is competing against the shift in threshold voltage. If a device was made such that the threshold voltage shifted negatively, the degradation of mobility would amplify the signal. With sensitivities ~ 100 times less than clinically used MOSFETs these devices are not very attractive as dosimeters used in the clinic

in their current state. However, they could potentially be used for higher dose applications. High doses are used for sterilization of medical products, food irradiations to reduce pathogens, and some plastic film and packaging is irradiated for better performance. Another potential application is to make the devices even more radio-resistant for use in electronics. Although this would not make a good dosimeter, if the electronic characteristics were good enough they could have potential applications in radiation environments as transistors. Since the current OTFTs are not sensitive enough for use as a clinical dosimeter, future work will explore methods to improve sensitivity such as, changing the device configuration, using different materials, and potentially the device type (e.g. diodes).

4.4 Lifetime of OTFTs

In this study an OTFT was irradiated up to 1000 Gy and the mobility and threshold voltage continued to change with dose. As dosimeters MOSFETs have a limited lifetime that depends on the design of the device. Many MOSFETs used clinically have lifetimes below 100 Gy and lose sensitivity over their lifetimes [16, 34]. After 300 Gy the OTFT had a sensitivity of 0.8 ± 0.1 mV/Gy. The response of the OTFTs converge with accumulated dose across the four energies used (100 kV, 180 kV, 6MV, and 18 MV). Perhaps a pre-irradiation could be used to reduce the energy dependence between the devices. If the devices were pre-irradiated to 300 Gy, that would leave a lifetime of at least 700 Gy, which is longer than clinically used MOSFETs.

4.5 Comparisons of Different Quality Photon Beams

We observed greater changes in the threshold voltage and mobility of the OTFTs irradiated with kV photon beams in comparison to MV photon beams at low accumulated doses (<200 Gy). One contributing factor may be that the average dose rate is about twice as high for the megavoltage beams as the kilovoltage beams, but the pulsed nature of the linac beam creates a substantially higher instantaneous dose rate. A higher dose rate increases the density of ionization and increases the likelihood of recombination. Furthermore, the devices are on a PET substrate on top of glass which could be causing a perturbation to the true energy dependence of the device, particularly at low photon

Table II: The starting (before irradiation) OTFT parameters: threshold voltage (V_{TH}), on current (I_{ON}), and off current (I_{OFF}) are given for each photon beam energy.

	V_{TH}	$I_{ON}(A)$	$I_{OFF}(A)$
100 kV	-19.7	5.9×10^{-6}	2.1×10^{-8}
180 kV	-21.3	6.5×10^{-6}	2.6×10^{-9}
6 MV	-14.1	1.3×10^{-5}	4.7×10^{-9}
18 MV	-14.2	3.9×10^{-5}	4.5×10^{-8}

energies. The glass was used to aid with the fabrication process, but can be removed for future studies. The PET substrate can be peeled off of the glass to produce flexible OTFTs from our current design. When irradiating flexible OTFTs, it will be important to investigate the dependence of the device response on the radius of curvature of the device.

Differences attributed to energy dependence in OTFT response may in fact be in part due to differences in the devices themselves. Table II shows some of the important starting parameters of the OTFTs. The two OTFTs irradiated with megavoltage photon beams have a lower threshold voltage and higher on currents than the OTFTs irradiated with kilovoltage photon beams. To measure the response of the OTFTs to various energy photon beams work should be done to optimize the OTFTs to ensure greater reproducibility of device characteristics. Furthermore, more OTFTs could be irradiated at each energy and look at the average response. We attempted to irradiate one OTFT with multiple energies, but had difficulty transferring the OTFT from one machine to another. The electrical contacts would often break off if the OTFTs were not handled carefully. To repeat this experiment the OTFT should be setup and secured on the solid water. Then, after irradiating the OTFT in one environment the entire setup should be moved simultaneously to avoid moving any of the connecting electrodes and causing damage to the device.

4.6 Monte Carlo Energy Dependence

In the energy range of Co-60-18 MV used in the Monte Carlo simulations of the device, there was an energy dependence of less than 5% when normalized to 6 MV. The initial response of the irradiated OTFTs showed an energy dependence. Up to 200 Gy the

sensitivity measured with photon beams of 6 MV and 18 MV were 1.3 ± 0.5 and 1.8 ± 0.3 , respectively. Between 200-400 Gy the sensitivities were 0.8 ± 0.2 and 0.9 ± 0.2 for 6 MV and 18 MV, respectively. This could indicate that there are more factors involved than the intrinsic energy dependence (at least initially), which will be investigated in the future.

Simulations of a simplistic OTFT were performed using monoenergetic beams with energies 20-100 keV. With the introduction of 800 nm of parylene-C close to the dielectric layer the perturbation factor changed from ~ 0.97 to ~ 0.62 at 20 keV when normalized to the response at 100 keV. When 800 nm parylene-C was introduced on the outside of 100 μm of parylene-F the perturbation factor changed from ~ 0.97 to ~ 0.92 at 20 keV when normalized to the response at 100 keV. These results show the importance of the location of the introduced material relative to the dielectric and the effect it will have. These results lead us away from using parylene-C in the simulations, but parylene-F showed good water equivalence. Placing the OTFT on a PET substrate immediately made the perturbation factor worse. To compensate, PMMA layers were introduced and the thickness varied. By using ~ 1400 nm of PMMA the perturbation factor differs from unity by less than 3% across the energy range from 20 keV to 100 keV when normalized to 100 keV.

4.7 Objectives of Work

The first objective of the work was to gain familiarity with the fabrication processes which was successful. Throughout the course of this work the characteristics of OTFTs were improved by modifying various fabrication steps.

The second objective of this work was to acquire preliminary data measuring the response of devices to fields of ionizing radiation which was successful as well. The OTFTs response using parameters such as threshold voltage and mobility were measured as a function of dose in photon fields of 100 kV, 180 kV, 6 MV, and 18 MV.

The last objective was to characterize the dependence of the devices on energy, direction and dose rate. We did experiments to measure each of these. Unfortunately, more experiments are needed to truly quantify the dependences of these devices. In the future devices could be irradiated to a high level (~ 200 Gy) before doing the experiments because the sensitivities measured across devices converged. These measurements may

benefit from improving the reproducibility and sensitivity of the OTFTs.

Chapter 5

Conclusion

MOSFETs are used as dosimeters in radiotherapy because they have a high sensitivity, immediate readout, and small size. However, MOSFETs cannot be reliably used at low energies (diagnostic energies) because they exhibit an energy dependence. OTFTs, which are similar to MOSFETs in their operation, use organic materials instead of silicon, which means they could have many of the same advantages of MOSFETs while having a lower energy dependence.

OTFT performance was improved with changes in fabrication process (i.e. cleaning PET substrate with camera brush) and material selection (i.e. from Parylene-C to PMMA). Irradiating OTFTs with photon beams of energies 100 kV, 180 kV, 6 MV, and 18 MV resulted in a positive shift in threshold voltage and a degradation in mobility for each device. Furthermore, Monte Carlo results suggest that the intrinsic energy dependence of the devices can be made small through appropriate material selection and device configuration. The Monte Carlo results contradict the initial response of the OTFTs, which showed energy dependence. This could indicate that there are more factors involved than the intrinsic energy dependence, which will be investigated in the future. Additional work is needed to improve the sensitivity and reproducibility of these devices. Furthermore, the energy, dose rate, directional and other dependencies of the OTFTs need to be investigated in greater detail. Two of the three objectives were met in this research. First, familiarity of the fabrication process was gained. Second, preliminary data of the response of the OTFTs to ionizing irradiation was measured. The final objective of characterizing various dependences of the devices (energy, dose rate, direction) was started, but more work is needed to be able to draw significant conclusions.

This work provides preliminary evidence that OTFTs can be used as radiation detectors/dosimeters and suggests that further study of these devices and others (e.g. diodes) is warranted.

Chapter 6

Future Work

6.1 More Reproducible OTFTs

Differences in initial device parameters make it difficult to compare the response of OTFTs across experiments. Improvements need to be made to improve the reproducibility of the devices. Various stages of the fabrication process could be optimized. For instance, the temperature of the substrate during pentacene deposition should be monitored more carefully. The temperature at which the pentacene is deposited will change the morphology of the pentacene and change the mobility [75]. Furthermore, a temperature change could affect the dielectric layer on which it is being deposited. PMMA has a glass transition temperature above 100 °C and pentacene is deposited at about 50 °C [76]. However, when depositing pentacene the temperature of the substrate is not known well. Perhaps monitoring the OTFT temperature more accurately and optimizing the temperature to produce better OTFTs would help make them more reproducible.

Other dielectric materials will be explored as part of a process to increase reproducibility of the OTFTs. It may be worth revisiting the parylene-C or perhaps other parylene dielectrics. When the instability of the parylene-C OTFT was measured, the measurements in the clinical setup had not yet been improved. The high and noisy off-current associated with low quality data acquisition may have overestimated the instability of the device. We referenced Ismail and Hill as evidence of threshold voltage instability in devices with a parylene dielectric, but it is possible that other factors contributed to our observed instabilities in threshold voltage [67]. Perhaps another parylene could work even better. The advantage of using parylene is how uniformly it coats the surface. A smooth dielectric is essential to allow a smooth interface between the dielectric and semiconductor which facilitates high mobility [77].

6.2 Removal of OTFTs from Glass

Currently we have four OTFTs on each glass substrate. The original plan was to remove the PET substrate from the glass and cut the PET so that each of the four OTFTs could be measured and irradiated separately. However, the consequences of bending the OTFTs are unknown. In the interest of time and the desire to irradiate the OTFTs and measure the response, the devices remained attached to the glass substrate, but the removal and bending of the OTFTs will be investigated in the future. This means that for every four OTFTs made, only one was used for experiment. Using all four could help improve reproducibility as well since each of the four devices would undergo nominally the same conditions during fabrication. Furthermore, this allows applications using a flexible design and will likely reduce the intrinsic energy dependence that glass may cause at low energies. Experiments with flexible substrates pose numerous additional questions that will need to be answered, particularly the effect of substrate bending on device response.

6.3 Energy and Directional Dependence

With more reproducible OTFTs the energy and directional dependence should be measured again. While the initial results were encouraging, it will be important to quantify these and other dependencies with greater confidence. Furthermore, it would be advantageous to irradiate one OTFT with multiple energies. In this work separate OTFTs were irradiated at each energy, meaning that differences may not only be due to energy dependence, but also to differences in OTFTs. By irradiating a single device across multiple energies, the differences in response due to variation in devices could be eliminated. The difficulty of irradiating one device is that the initial response of the device is quite variable. To overcome this the device should be switched between energies multiple times and should be irradiated to a high dose. Since the sensitivity of our measurements decrease with accumulated dose the results should be compared to devices irradiated at one energy to see if changes in sensitivity follow the normal trajectory or if they are due to an energy dependence of the device.

6.4 Other Organic Electronics

We would also like to investigate the use of organic semiconductors in diodes and monitor their response to irradiation. Several groups have made diodes that show a linear response with dose rate [55, 56]. Mills *et al* used a flexible kapton substrate and Intaniwet *et al* used a glass substrate to measure sensitivities up to 20 and 457 nC mGy⁻¹ cm⁻³ respectively. Optimizing these devices for sensitivity and water equivalence could make them viable dosimeters.

6.5 Other OTFT Investigations

One of the principal areas for improvement in OTFT dosimeters is the sensitivity. Current values are sufficiently low that it would be difficult to find practical applications for them in a clinical environment. Future work will focus on trying to improve sensitivity by varying the device design with respect to the active area, materials, and thicknesses of the various layers the OTFTs. Following the optimization of single device designs, we will build prototype, few OTFT arrays for planar dose distribution measurements. Extrapolation from there to a high resolution planar array would be an engineering challenge, but certainly not insurmountable. Finally, we will investigate at a more basic level to understand the mechanisms of signal generation of OTFTs. For example materials used in the OTFT will be looked at using solid state nuclear magnetic resonance (NMR) spectroscopy and Fourier transform infrared (FTIR) spectroscopy before and after irradiation to help understand how radiation changes the chemical composition and the resulting changes contribute to a change in signal in the OTFT. FTIR is used to obtain the infrared spectrum of absorption or emission of a sample. NMR spectroscopy can be used to determine the chemical properties of molecules and look for radiation-induced changes following exposure to ionizing radiation.

6.6 Monte Carlo Simulations

Polyenergetic beams should be used in the simulations of kilovoltage energies to understand the energy dependence better. Spekcalc can be used to generate kilovoltage spectra of the Xstrahl 300 orthovoltage x-ray unit that was used experimentally in this study. In some of the simulations in this work monoenergetic beams of 20-100 keV were

used. Using monoenergetic sources can give the impression that the energy dependence is larger than it would be for a more realistic source used in the clinical environment. A realistic source will have a distribution of energies which could wash out some of the energy dependences measured in our simulations. Moving forward more detailed simulations can be used to evaluate which materials (i.e. dielectrics, substrates etc.), geometries (i.e. thicknesses, orientations etc.) and different device designs such as diodes. The simulations will be used to motivate the direction of our experiments.

Bibliography

- [1] G. A. J. Hall, Eric J., Radiobiology for the radiologist, iD: 781261683 (2012).
- [2] K. D. Miller, R. L. Siegel, C. C. Lin, A. B. Mariotto, J. L. Kramer, J. H. Rowland, K. D. Stein, R. Alteri, A. Jemal, Cancer treatment and survivorship statistics, 2016. CA: A Cancer Journal for Clinicians **66** (2016) 271–289. doi:10.3322/caac.21349.
- [3] F. H. Attix, Introduction to radiological physics and radiation dosimetry, John Wiley and Sons, 2008.
- [4] L. A. DeWerd, S. D. Davis, L. J. Bartol, F. Grenzow, Ionization chamber instrumentation. Clinical Dosimetry Measurements in Radiotherapy, edited by DWO Rogers and JE Cygler (Medical Physics Publishing, Madison, Wisconsin, 2009) (2009).
- [5] L. A. DeWerd, J. Micka, R. Laird, D. Pearson, M. O’Brien, P. Lamperti, The effect of spectra on calibration and measurement with mammographic ionization chambers. Medical physics **29** (2002) 2649–2654.
- [6] L. DeWerd, L. Bartol, S. Davis, Thermoluminescence dosimetry. Clinical Dosimetry Measurements in Radiotherapy. Madison WI: Medical Physics Publishing (2009).
- [7] A. Nunn, S. Davis, J. Micka, L. DeWerd, LiF: Mg, Ti TLD response as a function of photon energy for moderately filtered x-ray spectra in the range of 20–250 kVp relative to C₆₀. Medical physics **35** (2008) 1859–1869.
- [8] C. G. Soares, S. Trichter, S. Devic, Radiochromic film. Textbook of AAPM Summer School (2009).
- [9] H. Bouchard, F. Lacroix, G. Beaudoin, J. Carrier, I. Kawrakow, On the characterization and uncertainty analysis of radiochromic film dosimetry. Medical physics **36** (2009) 1931–1946.
- [10] I. Das, D. Rogers, J. Cygler, Diamond detector. Clinical Dosimetry Measurements in Radiotherapy. Medical Physics Publishing, Madison, WI (2009) 891–912.
- [11] T. C. Zhu, A. Saini, J. Cygler, Diode dosimetry for megavoltage electron and photon beams. Clinical Dosimetry Measurements in Radiotherapy (2009) 913–939.
- [12] A. S. Saini, T. C. Zhu, Energy dependence of commercially available diode detectors for in-vivo dosimetry. Medical physics **34** (2007) 1704–1711.
- [13] D. Wilkins, X. A. Li, J. Cygler, L. Gerig, The effect of dose rate dependence of p-type silicon detectors on linac relative dosimetry. Medical physics **24** (1997) 879–881.

- [14] K. T. Welsh, L. Reinstein, The thermal characteristics of different diodes on in vivo patient dosimetry. *Medical physics* **28** (2001) 844–849.
- [15] J. V. Dam, G. Leunens, A. Dutreix, Correlation between temperature and dose rate dependence of semiconductor response; influence of accumulated dose. *Radiotherapy and Oncology* **19** (1990) 345–351.
- [16] J. Cygler, P. Scalchi, Mosfet dosimetry in radiotherapy. *Clinical Dosimetry Measurements in Radiotherapy* (2009) 941–977.
- [17] A. S. Sedra, K. C. Smith, *Microelectronic circuits*, New York: Oxford University Press, 1998.
- [18] H. Klauk, Organic thin-film transistors. *Chemical Society Reviews* **39** (2010) 2643–2666.
- [19] R. C. Hughes, Hole mobility and transport in thin sio2 films. *Applied Physics Letters* **26** (1975) 436–438. doi:10.1063/1.88200.
- [20] R. C. Hughes, Charge-carrier transport phenomena in amorphous si o2 : Direct measurement of the drift mobility and lifetime. *Physical Review Letters* **30** (1973) 1333–1336. doi:10.1103/PhysRevLett.30.1333.
- [21] J. R. Schwank, M. R. Shaneyfelt, D. M. Fleetwood, J. A. Felix, P. E. Dodd, P. Paillet, V. Ferlet-Cavrois, Radiation effects in mos oxides. *IEEE Transactions on Nuclear Science* **55** (2008) 1833–1853.
- [22] P. J. McWhorter, S. L. Miller, W. M. Miller, Modeling the anneal of radiation-induced trapped holes in a varying thermal environment. *IEEE Transactions on Nuclear Science* **37** (1990) 1682–1689. ID: 1. doi:10.1109/23.101177.
- [23] F. B. McLean, T. R. Oldham. *Basic mechanisms of radiation effects in electronic materials and devices* (1987).
- [24] W. L. Warren, M. R. Shaneyfelt, D. M. Fleetwood, J. R. Schwank, P. S. Winokur, R. A. B. Devine, Microscopic nature of border traps in mos oxides. *IEEE Transactions on Nuclear Science* **41** (1994) 1817–1827. ID: 1. doi:10.1109/23.340513.
- [25] M. R. Shaneyfelt, J. R. Schwank, D. M. Fleetwood, P. S. Winokur, K. L. Hughes, F. W. Sexton, Field dependence of interface-trap buildup in polysilicon and metal gate mos devices. *IEEE Transactions on Nuclear Science* **37** (1990) 1632–1640. ID: 1. doi:10.1109/23.101171.
- [26] D. M. Fleetwood, P. S. Winokur, J. R. Schwank, Using laboratory x-ray and cobalt-60 irradiations to predict cmos device response in strategic and space environments. *IEEE Transactions on Nuclear Science* **35** (1988) 1497–1505. ID: 1. doi:10.1109/23.25487.

- [27] J. R. Schwank, P. S. Winokur, P. J. McWhorter, F. W. Sexton, P. V. Dressendorfer, D. C. Turpin, Physical mechanisms contributing to device "re-bound". IEEE Transactions on Nuclear Science **31** (1984) 1434–1438. ID: 1. doi:10.1109/TNS.1984.4333525.
- [28] M. R. Shaneyfelt, J. R. Schwank, D. M. Fleetwood, P. S. Winokur, K. L. Hughes, G. L. Hash, M. P. Connors, Interface-trap building rates in wet and dry oxides. IEEE Transactions on Nuclear Science **39** (1992) 2244–2251. ID: 1. doi:10.1109/23.211427.
- [29] D. M. Fleetwood, P. V. Dressendorfer, D. C. Turpin, A reevaluation of worst-case postirradiation response for hardened mos transistors. IEEE Transactions on Nuclear Science **34** (1987) 1178–1183. ID: 1. doi:10.1109/TNS.1987.4337449.
- [30] A. J. Leis, T. R. Oldham, W. M. DeLancey, Response of interface traps during high-temperature anneals [mosfets]. IEEE Transactions on Nuclear Science **38** (1991) 1590–1597. ID: 1. doi:10.1109/23.124150.
- [31] G. Ensell, A. Holmes-Siedle, L. Adams, Thick oxide pmosfet dosimeters for high energy radiation. Nuclear Instruments and Methods in Physics Research Section A: Accelerators, Spectrometers, Detectors and Associated Equipment **269** (1988) 655–658.
- [32] P. R. Almond, P. J. Biggs, B. M. Coursey, W. F. Hanson, M. S. Huq, R. Nath, D. W. O. Rogers, Aapm's tg-51 protocol for clinical reference dosimetry of high-energy photon and electron beams. Medical physics **26** (1999) 1847–1870. doi:10.1118/1.598691.
- [33] R. A. Kinhikar, P. K. Sharma, C. M. Tambe, D. D. Deshpande, Dosimetric evaluation of a new onedose mosfet for ir-192 energy. Physics in Medicine and Biology **51** (2006)p. 1261.
- [34] G. P. Beyer, G. G. Mann, J. A. Pursley, E. T. Espenhahn, C. Fraisse, D. J. Godfrey, M. Oldham, T. B. Carrea, N. Bolick, C. W. Scarantino, An implantable mosfet dosimeter for the measurement of radiation dose in tissue during cancer therapy. IEEE Sensors Journal **8** (2008) 38–51.
- [35] T. Cheung, M. J. Butson, K. Peter, Effects of temperature variation on mosfet dosimetry. Physics in Medicine and Biology **49** (2004)p. N191.
- [36] R. A. Kinhikar, P. K. Sharma, C. M. Tambe, U. M. Mahantshetty, R. Sarin, D. D. Deshpande, S. K. Shrivastava, Clinical application of a onedoseTM mosfet for skin dose measurements during internal mammary chain irradiation with high dose rate brachytherapy in carcinoma of the breast. Physics in Medicine and Biology **51** (2006)p. N263.
- [37] T. M. Briere, M. T. Gillin, A. S. Beddar, Implantable mosfet detectors: Evaluation of a new design. Medical physics **34** (2007) 4585–4590.

- [38] P. Scalchi, P. Francescon, Calibration of a mosfet detection system for 6-mv in vivo dosimetry. *International Journal of Radiation Oncology* Biology* Physics* **40** (1998) 987–993.
- [39] N. Jornet, P. Carrasco, D. Jurado, A. Ruiz, T. Eudaldo, M. Ribas, Comparison study of mosfet detectors and diodes for entrance in vivo dosimetry in 18 mv x-ray beams. *Medical physics* **31** (2004) 2534–2542.
- [40] R. Ramani, S. Russell, P. O’Brien, Clinical dosimetry using mosfets. *International Journal of Radiation Oncology* Biology* Physics* **37** (1997) 959–964.
- [41] R. Ramaseshan, K. Kohli, T. Zhang, T. Lam, B. Norlinger, A. Hallil, M. Islam, Performance characteristics of a micromosfet as an in vivo dosimeter in radiation therapy. *Physics in Medicine and Biology* **49** (2004)p. 4031.
- [42] P. H. Halvorsen, Dosimetric evaluation of a new design mosfet in vivo dosimeter. *Medical physics* **32** (2005) 110–117.
- [43] V. Panettieri, M. A. Duch, N. Jornet, M. Ginjaume, P. Carrasco, A. Badal, X. Ortega, M. Ribas, Monte carlo simulation of mosfet detectors for high-energy photon beams using the penelope code. *Physics in Medicine and Biology* **52** (2006)p. 303.
- [44] C. Edwards, S. Green, J. Palethorpe, P. Mountford, The response of a mosfet, p-type semiconductor and lif tld to quasi-monoenergetic x-rays. *Physics in Medicine and Biology* **42** (1997)p. 2383.
- [45] B. Wang, C. Kim, X. G. Xu, Monte carlo modeling of a high-sensitivity mosfet dosimeter for low-and medium-energy photon sources. *Medical physics* **31** (2004) 1003–1008.
- [46] B. Wang, X. G. Xu, C.-H. Kim, Monte carlo study of mosfet dosemeter characteristics: dose dependence on photon energy, direction and dosemeter composition. *Radiation Protection Dosimetry* **113** (2005) 40–46.
- [47] C. F. Chuang, L. J. Verhey, P. Xia, Investigation of the use of mosfet for clinical imrt dosimetric verification. *Medical physics* **29** (2002) 1109–1115.
- [48] P. Scalchi, P. Francescon, P. Rajaguru, Characterization of a new mosfet detector configuration for in vivo skin dosimetry. *Medical physics* **32** (2005) 1571–1578.
- [49] Z. Qi, X. Deng, S. Huang, L. Zhang, Z. He, X. A. Li, I. Kwan, M. Lerch, D. Cutajar, P. Metcalfe, In vivo verification of superficial dose for head and neck treatments using intensity-modulated techniques. *Medical physics* **36** (2009) 59–70.
- [50] C. G. Rowbottom, D. A. Jaffray, Characteristics and performance of a micro-mosfet: An “imageable” dosimeter for image-guided radiotherapy. *Medical physics* **31** (2004) 609–615.

- [51] J. E. Cygler, A. Saoudi, G. Perry, C. Morash, E. Choan, Feasibility study of using mosfet detectors for in vivo dosimetry during permanent low-dose-rate prostate implants. *Radiotherapy and oncology* **80** (2006) 296–301.
- [52] C. W. Scarantino, D. M. Ruslander, C. J. Rini, G. G. Mann, H. T. Nagle, R. D. Black, An implantable radiation dosimeter for use in external beam radiation therapy. *Medical physics* **31** (2004) 2658–2671.
- [53] A. Beddar, M. Salehpour, T. Briere, H. Hamidian, M. Gillin, Preliminary evaluation of implantable mosfet radiation dosimeters. *Physics in Medicine and Biology* **50** (2004)p. 141.
- [54] S. Best, A. Ralston, N. Suchowerska, Clinical application of the onedoseTM patient dosimetry system for total body irradiation. *Physics in Medicine and Biology* **50** (2005)p. 5909.
- [55] C. A. Mills, Y.-F. Chan, A. Intaniwet, M. Shkunov, A. Nisbet, J. L. Keddie, P. J. Sellin, Direct detection of 6 mv x-rays from a medical linear accelerator using a semiconducting polymer diode. *Physics in Medicine and Biology* **58** (2013)p. 4471.
- [56] A. Intaniwet, J. L. Keddie, M. Shkunov, P. J. Sellin, High charge-carrier mobilities in blends of poly (triarylamine) and tips-pentacene leading to better performing x-ray sensors. *Organic Electronics* **12** (2011) 1903–1908.
- [57] H. N. Raval, S. P. Tiwari, R. R. Navan, V. R. Rao, Determining ionizing radiation using sensors based on organic semiconducting material. *Applied Physics Letters* **94** (2009)p. 92.
- [58] J. J. Kim, J. M. Ha, H. M. Lee, H. S. Raza, J. W. Park, S. O. Cho, Effect of electron-beam irradiation on organic semiconductor and its application for transistor-based dosimeters. *ACS applied materials and interfaces* **8** (2016) 19192–19196.
- [59] D. B. Hall, P. Underhill, J. M. Torkelson, Spin coating of thin and ultrathin polymer films. *Polymer Engineering and Science* **38** (1998) 2039–2045.
- [60] D. M. Mattox, Handbook of physical vapor deposition (PVD) processing, William Andrew, 2010.
- [61] R. Ghodssi, P. Lin, Mems materials and processes handbook. Springer Science and Business Media **1** (2011).
- [62] P. Kramer, A. Sharma, E. Hennecke, H. Yasuda, Polymerization of para-xylylene derivatives (parylene polymerization). i. deposition kinetics for parylene n and parylene c. *Journal of Polymer Science Part A: Polymer Chemistry* **22** (1984) 475–491.
- [63] C. D. Dimitrakopoulos, D. J. Masearo, Organic thin-film transistors: A review of recent advances. *IBM Journal of research and development* **45** (2001) 11–27.

- [64] B. Kumar, B. K. Kaushik, Y. S. Negi, Organic thin film transistors: structures, models, materials, fabrication, and applications: a review. *Polymer Reviews* **54** (2014) 33–111.
- [65] S. Basu, M. C. Lee, Y.-H. Wang, Graphene-based electrodes for enhanced organic thin film transistors based on pentacene. *Physical Chemistry Chemical Physics* **16** (2014) 16701–16710.
- [66] B. Walters, I. Kawrakow, D. Rogers, Dosxyznrc users manual. Nrc Report Pirs **794** (2005).
- [67] A. G. Ismail, I. G. Hill, Stability of n-channel organic thin-film transistors using oxide, sam-modified oxide and polymeric gate dielectrics, iD: 272178 (June 2011 2011). doi:<http://dx.doi.org/10.1016/j.orgel.2011.03.027>.
- [68] F. D. Angelis, M. Gaspari, A. Procopio, G. Cuda, E. D. Fabrizio, Direct mass spectrometry investigation on pentacene thin film oxidation upon exposure to air. *Chemical Physics Letters* **468** (2009) 193–196.
- [69] R. Velazco, P. Fouillat, R. Reis, Radiation effects on embedded systems, Springer Science and Business Media, 2007.
- [70] M. M. Pejovic, P-channel mosfet as a sensor and dosimeter of ionizing radiation. *Facta Universitatis, Series: Electronics and Energetics* **29** (2016) 509–541.
- [71] L.-L. Chua, J. Zaumseil, J.-F. Chang, E. C. Ou, General observation of n-type field-effect behaviour in organic semiconductors. *Nature* **434** (2005)p. 194.
- [72] Y.-Y. Noh, J. Ghim, S.-J. Kang, K.-J. Baeg, D.-Y. Kim, K. Yase, Effect of light irradiation on the characteristics of organic field-effect transistors. *Journal of Applied Physics* **100** (2006)p. 094501.
- [73] T.-Y. Kim, J. Jang, K. Cho, Y. Song, W. Park, J. Park, J.-K. Kim, W.-K. Hong, T. Lee, Interface effect in pentacene field-effect transistors from high energy proton beam irradiation. *Organic Electronics* **27** (2015) 240–246.
- [74] J. E. McDermott, M. McDowell, I. G. Hill, J. Hwang, A. Kahn, S. L. Bernasek, J. Schwartz, Organophosphonate self-assembled monolayers for gate dielectric surface modification of pentacene-based organic thin-film transistors: A comparative study. *The Journal of Physical Chemistry A* **111** (2007) 12333–12338.
- [75] D. Knipp, R. Street, A. Völkel, J. Ho, Pentacene thin film transistors on inorganic dielectrics: Morphology, structural properties, and electronic transport. *Journal of Applied Physics* **93** (2003) 347–355.
- [76] A. Richard, Interface and surface effects on the glass-transition temperature in thin polymer films. *Faraday discussions* **98** (1994) 219–230.

- [77] S. Steudel, S. D. Vusser, S. D. Jonge, D. Janssen, S. Verlaak, J. Genoe, P. Heremans, Influence of the dielectric roughness on the performance of pentacene transistors. *Applied Physics Letters* **85** (2004) 4400–4402.